International Journal of Smart Grid (IJSmartGrid)
https://www.ijsmartgrid.org/ Online ISSN: 2602-439X
A. Tatish and K. Vaisakh., Vol. 10, No. 1, March, 2026 Research Article

Simplified Finite-Control-Set Model Predictive Control for Grid-Connected Inverters with LCL Filters: Reduced Prediction Horizon and Weighting Factors-Free Design

Adel Tatish *‡, Kanchapogu Vaisakh *

* Department of Electrical Engineering, Andhra university, Visakhapatnam 530017, AP, India

(adeltatish.rs@andhrauniversity.edu.in, prof.kvaisakh@andhrauniversity.edu.in)

‡ Corresponding Author; Andhra university, Visakhapatnam 530017, AP, India Tel: +917567627748,

adeltatish.rs@andhrauniversity.edu.in

Received: 28.08.2025 Accepted:23.11.2025

Abstract- Finite-Control-Set Model Predictive Control (FCS-MPC) has shown great promise for controlling microgrid converters. However, conventional FCS-MPC approaches applied to high-order dynamic systems, such as grid-connected converters with LCL filters, require a long prediction horizon to achieve accurate grid current tracking, resulting in increased computational burden. This paper proposes a simplified FCS-MPC strategy for grid-connected inverters with LCL filters, addressing the computational complexity and tuning challenges of conventional methods. By tracking the filter capacitor voltage instead of directly regulating grid-side or converter-side currents, the proposed approach reduces the required prediction horizon from six steps (Np=6) to three steps (Np=3), significantly lowering computational burden. This reduction, coupled with a single-objective cost function, slashes the computational time by over 300 times, from 7.8 ms to 25.3 µs on embedded hardware (400 MHz CPU), making real-time implementation feasible. A single-objective cost function eliminates the need for weighting factors, simplifying controller design and tuning. The method ensures sinusoidal current injection even under unbalanced grid conditions by exclusively utilizing the positive sequence of the PCC voltage, extracted via a discrete-time quadrature signal generator. The effectiveness of the proposed strategy is validated through both MATLAB/Simulink simulations and experimental testing. The results demonstrate that the proposed controller achieves performance comparable to conventional FCS-MPC approaches with longer prediction horizons, maintaining a low grid-current THD of 1.7%, while offering the distinct advantages of reduced computational complexity, improved robustness against grid harmonics and voltage sags, and simpler implementation without the need for tuning weighting factors.

Keywords Grid following inverter, LCL filter, finite-control-set model predictive control (FCS-MPC), prediction horizon.

1. Introduction

Conventional power systems are structured to allow power flow from central plants to transmission and distribution systems. However, the increasing quest to benefit from renewable energy sources (RES) has prompted many developed countries to change the power system's structure to suit the new grid's requirements with high penetration of RES [1]. Furthermore, microgrids emerged and spread widely as one of the solutions for integrating distributed generation (DG) systems based on RES into conventional power systems, apart from their notable role in enhancing reliability,

Cite this article as: A. Tatish and K. Vaisakh, "Simplified Finite-Control-Set Model Predictive Control for Grid-Connected Inverters with LCL Filters: Reduced Prediction Horizon and Weighting Factors-Free Design" *International Journal of Smart Grid (ijSmartGrid)*, Vol. 10, No. 1, pp. 1–13, March, 2026.

flexibility, economical operation, and optimal use of distributed energy resources [2].

Grid-connected inverters (GCI) play a crucial role in microgrids as they serve as power interfaces that facilitate the integration of DG units into the utility grid and contribute with several advantageous characteristics, including controlling active and reactive power flow and injecting high-quality current into the grid [3], [4]. In this work, we focus on voltage-source inverters (VSIs), which are widely adopted in industrial applications due to their simple structure, compatibility with LCL filters, and ease of modulation [5], [6]. The simple two-level inverter topology is most favored among the various inverter topologies due to its simple operating principle, basic structure, and extensive industrial utilization [7] [8]. The researchers have developed several control strategies for GCIs. Among these strategies, simple control strategies like traditional PID-based controllers and PR-based controllers are widely employed for GCI applications [2], [4], and [9]. However, these approaches possess certain limitations [8], [10]. The control structure, consisting of multiple complex feedback loops and Pulse Width Modulation (PWM), leads to a delayed dynamic response. Additionally, tuning PI or PR parameters is time-consuming, making the controller more intricate. Furthermore, the inherent uncertainties in renewable energy sources lead to fluctuations in the DC-bus voltage in the case of a microgrid, thereby further deteriorating the power quality on the AC side. Consequently, conventional cascaded PI or PR controllers may not effectively address these issues. Moreover, in LCL filter-based two-level inverters with PWM regulators, the stability is significantly influenced by the time delay caused by the modulation process [11]. As a result, implementing compensators and complicated tuning techniques for PI controllers becomes imperative, thereby augmenting the intricacy of the solution [12].

To overcome the traditional controller problems mentioned above, the Model Predictive Control strategy (MPC) has emerged as one of the promising controller solutions due to its fast dynamic response, ease of implementation, and ability to control several parameters for different variables through a single cost function. In addition, MPC is characterized by possibly including constraints in the cost function [13]. Despite that, the conventional MPC suffers from inherent limitations, such as computational complexity, variable switching frequency, average steady-state error, and optimum weighting factor selection [13].

Finite Control Set Model Predictive Control (FCS-MPC) is a type of MPC strategy classified as a direct MPC that controls the converter switches directly. The most significant advantages of this strategy are its fast transient response and its suitability for direct control systems such as (direct torque control) DTC and (direct power control) DPC. However, FCS-MPC is plagued by two significant limitations: the variable switching frequency and computational complexity [14], [15]. Given that the optimization variable in FCS-MPC is represented as an integer, the formulated optimization problem can be classified as a mixed integer program. Consequently, the computational complexity of this problem grows exponentially with the number of candidate solutions. Furthermore, it can become computationally intractable because the FCS-MPC optimization function must be solved in real time, typically within a few tens of microseconds [15].

Several strategies have been developed to reduce the FCS-MPC average computational burden. One of those strategies is proposed in [16] and [17] with one-step prediction horizons (Np=1). In [18], the evaluation of candidate inverter voltage vectors within two consecutive sampling periods is proposed. This approach effectively reduces the computational cost associated with sequential optimization steps. Nevertheless, when higher-order output filters like LCL filters are incorporated, such strategies will fail to track the sinusoidal references, and thus distortions will increase [19].

A comprehensive analysis was conducted in [20] to evaluate the performance of the FCS-MPC algorithm in a grid-connected inverter incorporated with an LCL filter for various state feedback controls and concluded that the prediction horizon longer than 6 with the grid-side current as a control-feedback is the practical solution to overcome the third-order dynamics of the LCL filter. Nevertheless, as mentioned earlier, increasing the prediction horizon length led to an exponential increase in the required calculations.

Multi-objective FCS-MPC strategies have already been proposed in the literature; in such strategies, two or more state variables are controlled using a single cost function. The FCS-MPC algorithm for a grid-connected inverter with LCL filter proposed in [21] considers the capacitor voltage, grid current, and inverter current as state feedback control variables. Furthermore, [19] proposed a different approach, recommending tracking the capacitor voltage reference and its first derivative as control variables feedback for the cost function. However, the presence of weighting factors is the main drawback of this approach, as the values of these factors decisively affect the controller's performance; unfortunately, there is no specific strategy or clear methodology to determine the optimal values of these factors, which makes the controller tuning process a complex and time-consuming task [14]. Therefore, some works in the literature have developed advanced strategies based on artificial intelligence, neural networks, or fuzzy logic techniques to tune these factors [22]-[24]. However, such strategies increase the complexity of the predictive controller design.

However, most existing FCS-MPC schemes for LCL-filtered grid-connected inverters still face a trade-off between computational efficiency and control accuracy. Conventional FCS-MPC with long prediction horizons and multi-objective weighting improves current quality for third-order LCL dynamics, but at the cost of high per-cycle computation and difficult tuning. This paper presents an FCS-MPC strategy that bridges the gap by reducing the prediction horizon from ($N_p = 6$) to ($N_p = 3$), while eliminating weighting factors. By tracking the LCL filter capacitor voltage instead of grid-side current, the proposed method decouples the control loop from the grid's delayed dynamics, enabling shorter horizons without compromising performance. This reduction significantly lowers the number of candidate solutions evaluated per control cycle, making real-time implementation feasible on low-cost embedded platforms. The approach retains the benefits of conventional FCS-MPC, such as fast transient response, while simplifying tuning and enhancing

robustness against grid disturbances. The key contributions of the proposed controller are listed below:

- The proposed method reduced the prediction horizon from Np=6 to Np=3 compared to conventional methods.
- The proposed method implements FCS-MPC using a single-objective cost function without weighting factors, thereby reducing design complexity and eliminating time-consuming tuning.
- The controller effectively eliminates grid current distortion caused by the amplification of high-frequency switching harmonics, which typically arises when tracking the converter-side current.
- It extracts the positive sequence of the PCC voltage and utilizes it exclusively, ensuring sinusoidal current injection even under unbalanced grid voltage conditions.
- The proposed method is validated through real-time embedded implementation using the NI sbRIO GPIC (Single-Board RIO Grid Processor-in-the-Loop Controller) Evaluation Kit.

The remainder of this paper is organized as follows: Section II presents the system description and modeling. Section III provides a brief review of conventional FCS-MPC strategies for GCIs and discusses their associated challenges. In Section IV, the proposed FCS-MPC strategy is introduced in detail. Section V presents both simulation and experimental results that validate the effectiveness, dynamic performance, and robustness of the proposed controller under various operating conditions. Finally, Section VI concludes the paper.

2. System Overview

Fig.1 illustrates the schematic diagram of a two-level three-phase voltage source inverter connected to a grid through an LCL filter. Using Kirchhoff's voltage law (KVL) at the inverter output, the dynamic model of the system is obtained as the following equations:

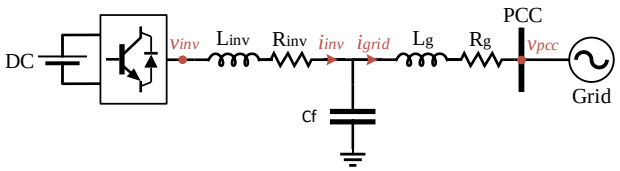

Fig. 1. Single line diagram of the grid-connected inverter with an LCL filter.

$$\frac{di_{inv}}{dt} = \frac{1}{L_{inv}}\left(v_{inv}(t) - i_{inv}(t)R_{inv} - v_c(t)\right) \quad (1)$$

$$\frac{di_{grid}}{dt} = \frac{1}{L_g}\left(v_c(t) - i_{grid}(t)R_g - v_{pcc}(t)\right) \quad (2)$$

$$\frac{dV_c}{dt} = \frac{i_{inv} - i_{grid}}{C_f} \quad (3)$$

Where i_{inv}, and i_{grid} are the inductor currents of the inverter side and the grid side filter, respectively, V_{inv} is the output voltage of the inverter, V_{PCC} is the voltage at PCC, V_c is the filter capacitor voltage, L_{inv} and L_g are the inverter side and the grid side of the LCL output filter, respectively, C_f is the filter capacitor and R_{inv} and R_g are the parasitic resistances of the inductors. This model can be described in a simple State-Space Model form as follows:

$$\dot{x} = Ax + Bu \quad (4)$$

$$x = \begin{bmatrix} i_{inv} \\ i_{grid} \\ v_c \end{bmatrix},\ u = \begin{bmatrix} v_{imv} \\ v_{pcc} \end{bmatrix} \quad (5)$$

$$A = \begin{bmatrix} -\frac{R_{inv}}{L_{inv}} & 0 & -\frac{1}{L_{inv}} \\ 0 & -\frac{R_{grid}}{L_g} & \frac{1}{L_g} \\ \frac{1}{C_f} & -\frac{1}{C_f} & 0 \end{bmatrix} \quad (6)$$

$$B = \begin{bmatrix} \frac{1}{L_{inv}} & 0 \\ 0 & -\frac{1}{L_g} \\ 0 & 0 \end{bmatrix} \quad (7)$$

The discrete-time model of the system described in Eq. (4) can be obtained for the sampling time using the Euler forward method:

$$\begin{bmatrix} i_{inv}(k+1) \\ i_{grid}(k+1) \\ v_c(k+1) \end{bmatrix} \approx A_d \begin{bmatrix} i_{inv}(k) \\ i_{grid}(k) \\ v_c(k) \end{bmatrix} + B_d \begin{bmatrix} v_{imv}(k) \\ v_{pcc}(k) \end{bmatrix} \quad (8)$$

$$A_d = \begin{bmatrix} 1 - \frac{T_s R_{inv}}{L_{inv}} & 0 & -\frac{T_s}{L_{inv}} \\ 0 & 1 - \frac{T_s R_g}{L_g} & \frac{T_s}{L_g} \\ \frac{1}{C_f} & -\frac{1}{C_f} & 0 \end{bmatrix} \quad (9)$$

$$B_d = \begin{bmatrix} \frac{1}{L_{inv}} & 0 \\ 0 & -\frac{1}{L_g} \\ 0 & 0 \end{bmatrix} \quad (10)$$

To ensure sampling-frequency adequacy during the discretization. The system is discretized with forward Euler at the sampling time (T_s) equal to the control/switching period. The T_s should be selected for ($f_s = 1/T_s \geq \kappa f_{\text{res}}$). With:

$$(\kappa \geq 20) \text{ and } f_{\text{res}} = \frac{1}{2\pi}\sqrt{\frac{L_1+L_2}{L_1 L_2 C}}, \text{ and ensure } (f_s \gg f_{\text{grid}}).$$

Hence ($\omega_{\text{res}} T_s \ll 1$), making the Euler local error $\mathcal{O}((\omega T_s)^2)$ negligible for our prediction horizon. The one-sample implementation delay is handled by applying the computed switching state in the next interval.

Moreover, the point of common coupling (PCC) voltage, denoted as v_{pcc}, at the time step (k+n) can be expressed as:

$$\tilde{v}_{pcc}(k+n) = v_{pcc}(k)e^{jn\omega T_s} \quad (11)$$

Here, ω represents the grid angular frequency, while the term ωT_s captures the phase shift of the PCC voltage over a single sampling interval T_s. When the sampling interval is sufficiently small, the PCC voltage can be assumed to remain approximately constant within that interval. Thus,

$$\tilde{v}_{pcc}(k+1) \approx v_{pcc}(k) \quad (12)$$

The relationship between the inverter output voltage v_{inv} and the DC-link voltage V_{dc} is determined by the switching states S of the individual inverter legs. In the $\alpha\beta$ reference frame, this relationship can be described by:

$$v_{inv} = \frac{2}{3} V_{dc}(S_a + aS_b + a^2 S_c) \quad (13)$$

Where, $S_a, S_b, S_c \in \{0,1\}$ are the switching states for the inverter legs (phase A, B, and C, respectively), and a is the complex operator $a = e^{j2\pi/3}$, which represents a 120° phase shift.

3. Conventional FCS-MPC

Finite Control Set Model Predictive Control (FCS-MPC) algorithms directly determine the converter switching signals by formulating the control objectives and system constraints into a cost function. This cost function quantifies the deviation between the desired reference values and the predicted behavior of the system. At each sampling instant, the cost function is evaluated for all feasible switching states of the converter, and the state that minimizes the cost is selected and applied.

For grid-connected inverters (GCIs) employing an LCL output filter, three primary approaches have been reported in the literature for designing the FCS-MPC cost function [20].

The first approach uses the converter-side current as feedback to track the reference current. This method is relatively straightforward and avoids the need for extended prediction horizons (typically $N_p \leq 2$). Moreover, the dynamic nature of the converter-side current can be effectively handled by appropriately designing the LCL filter parameters. However, this method may result in distortion of the grid-side current due to the amplification of high-frequency switching harmonics, which are pronounced near the resonant frequency of the LCL filter. Such distortions may lead to violations of grid code requirements. The associated cost function is given by:

$$g = \left(i_{inv}^{p} - i_{inv}^{*}\right)^2 + g_{lim} \quad (14)$$

Where i_{inv}^{p} and i_{inv}^{*} denote the predicted and reference converter-side currents, respectively, and g_{lim} the constraint penalty term, a function designed to enforce system limits (e.g., capacitor voltage limits, switching frequency reduction, …)

The second approach involves using the grid-side current i_{grid} as feedback. This method simplifies the control of power flow at the PCC by eliminating the need for explicit reactive power compensation. The associated cost function is also simpler:

$$g = \left(i_{grid}^{p} - i_{grid}^{*}\right)^2 + g_{lim} \quad (15)$$

Where i_{grid}^{p} and i_{grid}^{*} denote the predicted and reference grid-side currents, respectively. However, due to the third-order dynamics introduced by the LCL filter, the impact of switching actions on i_{grid} is delayed by at least three sampling intervals (i.e., noticeable at $k+3$). While the filter effectively attenuates high-frequency switching harmonics, this also reduces the responsiveness of the system to switching inputs. As a result, longer prediction horizons are required to maintain performance, leading to a significantly increased computational load.

To address the limitations associated with converter-side current distortion and the computational burden of long horizons, multi-objective FCS-MPC strategies have been proposed. These strategies incorporate multiple feedback variables, either the filter voltage combined with the converter-side current or the filter voltage combined with the grid-side current. The corresponding cost functions are formulated as:

$$g = \lambda_i\left(i_{inv}^{p} - i_{inv}^{*}\right)^2 + \lambda_v\left(v_c^{p} - v_c^{*}\right)^2 + g_{lim} \quad (16)$$

$$g = \lambda_i\left(i_{grid}^{p} - i_{grid}^{*}\right)^2 + \lambda_v\left(v_c^{p} - v_c^{*}\right)^2 + g_{lim} \quad (17)$$

Where, λ_i and λ_v are the weighting factors for the current and capacitor voltage tracking terms, respectively.

While these formulations can improve performance by balancing multiple objectives, they introduce increased complexity in controller design, particularly in the tuning of weighting factors. Moreover, the interplay between different control variables may result in unpredictable performance under varying operating conditions.

All FCS-MPC implementations are subject to time delays introduced by the computational process, which depend on the capabilities of the digital processor used. In modern systems, this delay typically remains below 50 microseconds [25], significantly shorter than that of pulse-width modulation (PWM) based controllers, which can be around 600 microseconds [26]. Nonetheless, to maintain optimal control performance, this delay must be compensated. A practical and effective compensation method is to apply the optimal switching state calculated at the current step in the next time interval [27]. As a result, even in systems where a prediction horizon of $N_p = 1$ would theoretically suffice, extending the horizon to $N_p = 2$ becomes necessary to account for processing delays.

4. Proposed Controller

This study proposes an FCS-MPC strategy that leverages the filter voltage (v_c) for direct tracking of its reference (v_c^*). The approach utilizes a single-objective cost function, thereby eliminating the need for tracking either the converter-side or grid-side current.

As discussed earlier, the switching actions applied to the converter do not produce an immediate effect on the filter voltage. Instead, their influence becomes evident after $N_p = 2$ two discrete time steps. As a result, a minimum prediction horizon of $N_p = 2$ is required to observe any impact of the control input on v_c. Similarly, the control signal applied at $k+1$ influences the filter voltage at $k+3$, effectively requiring a prediction horizon of $N_p = 3$.

To ensure accurate tracking of the reference voltage, it is therefore necessary to predict the values of $v_c(k+2)$ and $v_c(k+3)$. To reduce computational complexity, this paper derives explicit expressions for $v_c(k+2)$ and $v_c(k+3)$ as

direct functions of system variables measured at time step k. This approach eliminates the need for step-by-step recursive calculations from $k+1$through to $k+3$. Utilizing the system dynamics defined in Eqs. (8) – (10), these relationships are analytically derived and presented as follows:

$$v_c(k+2) = \alpha_1 v_{cf}(k) + \alpha_2 i_{inv}(k) + \alpha_3 i_{grid}(k) + \alpha_4 v_{inv}(k) + \alpha_5 v_{PCC}(k) \quad (18)$$

$$v_c(k+3) = \gamma_1 v_{cf}(k) + \gamma_2 i_{inv}(k) + \gamma_3 i_{grid}(k) + \gamma_4 v_{inv}(k) + \gamma_5 v_{inv}(k+1) + \gamma_6 v_{PCC}(k) \quad (19)$$

Where:

$$\alpha_1 = 1 - \frac{T_s^2}{C_f}\left(\frac{1}{L_{inv}} + \frac{1}{L_g}\right), \quad \alpha_2 = \frac{T_s}{C_f}\left(2 - \frac{T_s R_{inv}}{L_{inv}}\right)$$

$$\alpha_3 = -\frac{T_s}{C_f}\left(2 - \frac{T_s R_g}{L_g}\right), \quad \alpha_4 = \frac{T_s^2}{C_f L_{inv}}, \quad \alpha_5 = \frac{T_s^2}{C_f L_g}$$

$$\gamma_1 = 1 - \frac{T_s^2}{C_f}\left(\frac{3}{L_{inv}} + \frac{3}{L_g}\right) + \frac{T_s^3 R_{inv}}{C_f L_{inv}^2} + \frac{T_s^3 R_g}{C_f L_g^2}$$

$$\gamma_2 = \frac{T_s}{C_f}\left(3 - \frac{3T_s R_{inv}}{L_{inv}} + \frac{T_s^2 R_{inv}^2}{L_{inv}^2}\right) - \frac{T_s^3}{C_f L_{inv} L_g}$$

$$\gamma_4 = \frac{T_s^2}{C_f L_{inv}}\left(2 - \frac{T_s R_{inv}}{L_{inv}}\right), \quad \gamma_5 = \frac{T_s^2}{C_f L_{inv}}$$

$$\gamma_6 = -\frac{T_s^2}{C_f L_g}\left(3 - \frac{T_s R_g}{L_g}\right)$$

4.1 Reference Calculation

The primary objective of the proposed grid-following converter control system is to enable decoupled regulation of active and reactive power injected into the grid, thereby allowing operation at a controlled power factor. The relationship between active/reactive power and the point of common coupling (PCC) voltage in the $\alpha\beta$ frame is given by [28]:

$$\begin{bmatrix} P \\ Q \end{bmatrix} = \frac{3}{2}\begin{bmatrix} V_{pcc_\alpha} & V_{pcc_\beta} \\ V_{pcc_\beta} & -V_{pcc_\alpha} \end{bmatrix}\begin{bmatrix} I_{grid_\alpha} \\ I_{grid_\beta} \end{bmatrix} \quad (20)$$

Where V_{pcc_α}, V_{pcc_β} are the $\alpha\beta$ components of the PCC voltage, and I_{grid_α}, I_{grid_β} are the $\alpha\beta$ components of the grid-side current.

Accordingly, the grid-side current components in the $\alpha\beta$ frame can be derived from the desired active P and reactive power Q as:

$$i_{grid_\alpha} = \frac{2P \times v_{pcc_\alpha}}{3\left(v_{pcc_\alpha}^2 + v_{pcc_\beta}^2\right)} + \frac{2Q \times v_{pcc_\beta}}{3\left(v_{pcc_\alpha}^2 + v_{pcc_\beta}^2\right)} \quad (21)$$

$$i_{grid_\beta} = \frac{2P \times v_{pcc_\beta}}{3\left(v_{pcc_\alpha}^2 + v_{pcc_\beta}^2\right)} - \frac{2Q \times v_{pcc_\alpha}}{3\left(v_{pcc_\alpha}^2 + v_{pcc_\beta}^2\right)} \quad (22)$$

These expressions are used to determine the current references required to inject the desired power into the grid. To ensure sinusoidal current injection, only the positive sequence of the PCC voltage is utilized in the computation. Hence, the current references at time step k are given by:

$$i^*_{grid_\alpha}(k) = K_p(k) \times v^+_{pcc_\alpha}(k) + K_q(k) \times v^+_{pcc_\beta}(k) \quad (23)$$

$$i^*_{grid_\beta}(k) = K_p(k) \times v^+_{pcc_\beta}(k) - K_q(k) \times v^+_{pcc_\alpha}(k) \quad (24)$$

Where $v^+_{pcc_\alpha}$, $v^+_{pcc_\beta}$ are the $\alpha\beta$ components of the PCC voltage positive sequence, and K_p, K_q are given as:

$$K_p = \frac{2P^*}{3(V_m^+)^2}, \quad K_q = \frac{2Q^*}{3(V_m^+)^2} \quad (25)$$

And V_m^+ is the positive sequence amplitude of the PCC voltage. Using Eqs. (8) – (10), the grid-side current at time step $k+4$ is predicted as:

$$i_{grid}(k+4) = \frac{T_s}{L_g}\left(V_c(k+3) - R_g i_{grid}(k+3) - v_{pcc}(k+3)\right) + i_{grid}(k+3) \quad (26)$$

Accordingly, the reference filter voltage at $k+3$, required to achieve the desired current injection, is given by:

$$v_c^*(k+3) = \frac{L_g}{T_s}\left(i^*_{grid}(k+4) - i_{grid}(k+3)\right) + R_g i_{grid}(k+3) + v_{pcc}(k+3) \quad (27)$$

4.2 Cost Function Formulation

The proposed FCS-MPC approach employs a single objective cost function focused on minimizing the error between predicted and reference filter voltages. The cost function is defined as:

$$g = \left(v^*_{c_\alpha}(k+3) - v_{c_\alpha}(k+3)\right)^2 + \left(v^*_{c_\beta}(k+3) - v_{c_\beta}(k+3)\right)^2 + g_{i_{lim}} \quad (28)$$

Here, $g_{i_{lim}}$ is a penalty term that discourages excessive voltage magnitudes:

$$g_{i_{lim}} = \begin{cases} \|v_c(k+3)\|; & if \quad \|v_c(k+3)\| \geq V_{max} \\ 0 & otherwise \end{cases} \quad (29)$$

This formulation ensures that under normal conditions, the cost function remains purely focused on voltage tracking, while under constraint violations, it shifts priority to voltage regulation.

4.3 Positive Sequence Extraction

As previously mentioned, the proposed control strategy focuses solely on tracking the positive sequence component of the PCC voltage. This approach ensures sinusoidal current injection into the grid in scenarios of voltage sag or unbalanced grid voltage. The proposed method extracts the positive-sequence component of the PCC voltage using a

discrete-time quadrature signal generator (QSG) and sequence decoupling in the stationary $\alpha\beta$-frame. A harmonic oscillator model generates orthogonal signals $v_{\alpha\beta}^{q}$ from $v_{\alpha\beta}$, governed by:

$$\frac{dv_{\alpha\beta}^{q}}{dt} = -\omega_0 v_{\alpha\beta}, \quad \frac{dv_{\alpha\beta}}{dt} = \omega_0 v_{\alpha\beta}^{q} \tag{30}$$

Discretizing using the Euler-forward method with sampling time T_s:

$$v_{\alpha\beta}(k+1) \approx \omega_0 T_s v_{\alpha\beta}^{q}(k) + v_{\alpha\beta}(k) \tag{31}$$

$$v_{\alpha\beta}^{q}(k+1) \approx -\omega_0 T_s v_{\alpha\beta}(k) + v_{\alpha\beta}^{q}(k) \tag{32}$$

Solving recursively, the quadrature component at step k is:

$$v_{\alpha\beta}^{q}(k) \approx \frac{v_{\alpha\beta}(k) - (\varphi_0^2 T_s^2 + 1) v_{\alpha\beta}(k-1)}{\omega_0 T_s} \tag{33}$$

As evident from Eq. (33), the quadrature voltage component can be readily obtained using only the current and past voltage values. Fortunately, the proposed control strategy inherently provides these values, enabling the extraction of the positive voltage sequence in the frame, as shown below:

$$v_{\alpha}^{+}(k) = \frac{1}{2} v_{\alpha} + \frac{v_{\beta}(k) - (\omega_0^2 T_s^2 + 1) v_{\beta}(k-1)}{2\omega_0 T_s} \tag{34}$$

$$v_{\beta}^{+}(k) = \frac{1}{2} v_{\beta} - \frac{v_{\alpha}(k) - (\omega_0^2 T_s^2 + 1) v_{\alpha}(k-1)}{2\omega_0 T_s} \tag{35}$$

These expressions ensure accurate real-time extraction of the voltage positive sequence using only present and past measurements, making them well-suited for implementation in the proposed predictive control framework.

To mitigate harmonics from LCL resonance or grid distortion, a cascaded moving average filter (MAF) is applied to $v_{\alpha\beta}$ before sequence extraction. The MAF with window length $N_{MAF} = f_s/f_o$ (where $f_s = 1/T_s$) attenuates harmonics at integer multiples of f_o:

$$v_{\alpha\beta}^{flit}(k) = \frac{1}{N_{MAF}} \sum_{n=0}^{N_{MAF}-1} v_{\alpha\beta}(k-n) \tag{36}$$

This pre-filtering ensures robustness against 5th, 7th, and higher-order harmonics common in grid voltages.

Fig.2 illustrates the flowchart of the proposed finite control set model predictive control (FCS-MPC) algorithm, detailing the sequence of control operations executed at each sampling instant.

5. Results and Discussions

5.1 Simulation Results

To evaluate the performance of the proposed controller, a simulation of the system was conducted using MATLAB. The proposed controller's performance with three-step prediction horizons (Np=3) compared to a conventional grid-current-feedback-based FCS-MPC with Np=6, which exhibited the most favourable performance among other conventional controllers.

The steady-state performance of both the proposed and conventional controllers was evaluated under constant reference values of active power ($P = 3\,Kw$) and reactive power ($Q = 0\,var$). Fig.3 illustrates the waveforms of the grid-injected current for both controllers. It can be observed that the proposed controller, with a reduced prediction horizon, achieved a sinusoidal injected current with a THD of 1.7%. This value is remarkably close to the 1.6% THD achieved by the conventional controller with an extended prediction horizon.

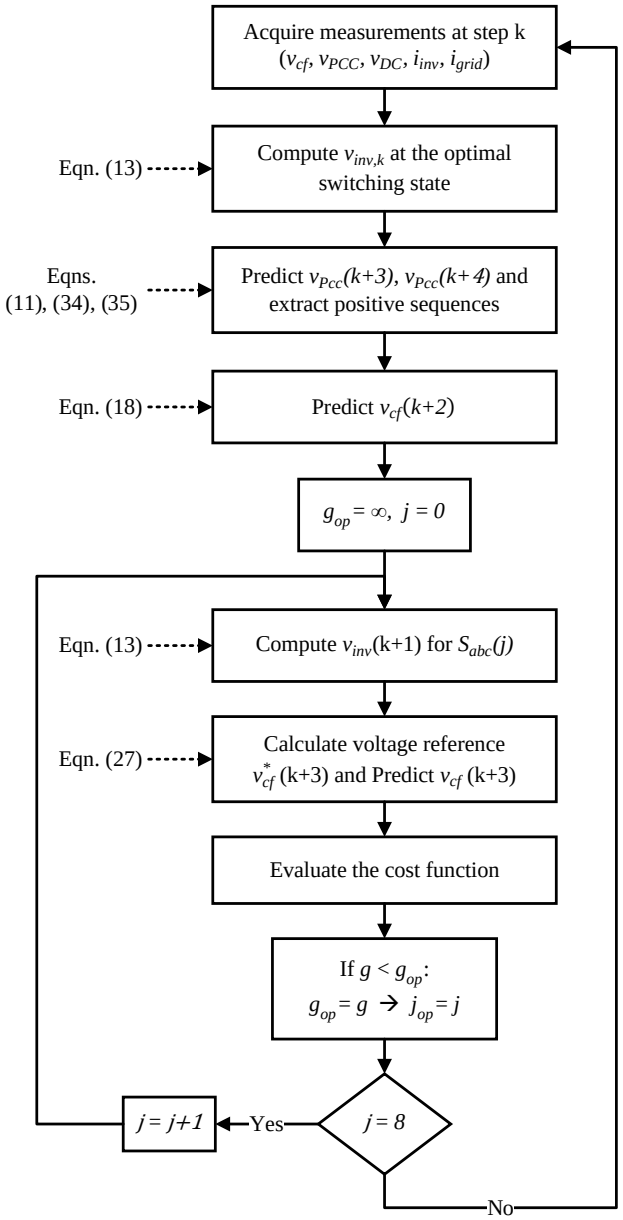

Fig. 2. Flowchart diagram of the proposed control method.

A critical component of testing the robustness of the proposed control system is evaluating its performance under model-plant parameter mismatch, where the parameters used in the predictive model deviate from the actual parameters of the physical system.

LCL filter parameters are the key system parameters that affect the predictive model. To assess the controller robustness under filter parameters mismatch, Simulations were conducted by varying the converter-side inductance, filter capacitance, and grid-side inductance while maintaining the

model parameters themselves. Fig.6 presents the resulting grid-injected current waveforms and their corresponding total harmonic distortion (THD) for the following scenarios: 50% increase and 50% decrease in converter-side inductance, 50% increase and 50% decrease in filter capacitance, and 50% increase and 50% decrease in grid-side inductance. These results illustrate that the system is robust against a wide range of mismatch model parameters.

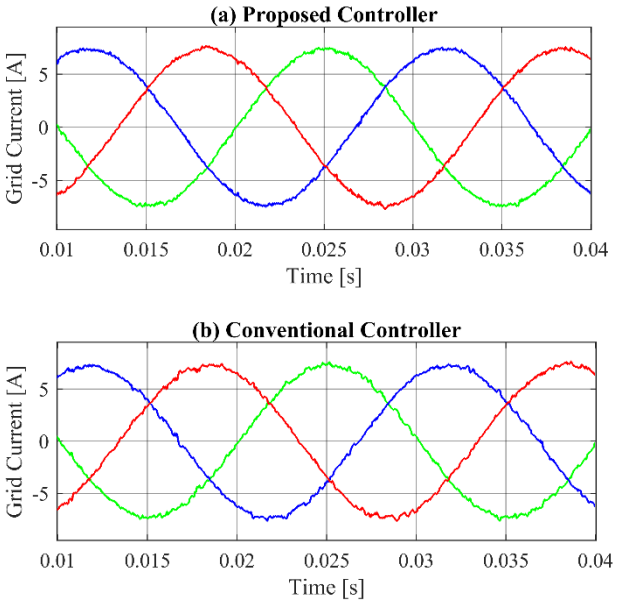

Fig. 3. Steady-state Waveforms of Grid Injected Current Under Stiff Grid Condition: (a) proposed FCS-MPC with Np=3, (b) Conventional grid current feedback-based FCS-MPC with Np=6.

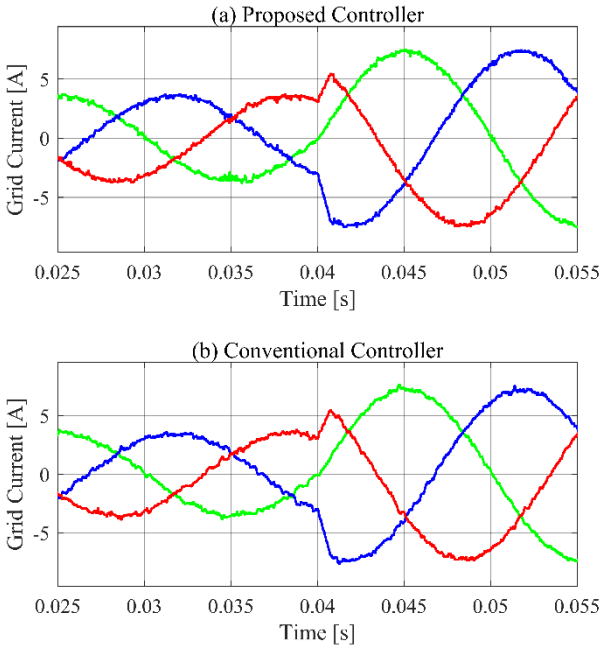

Fig. 4. Transient waveforms of grid injected current for step-up from 1.5 [KW] to 3 [KW] under stiff grid condition: (a) proposed FCS-MPC with Np=3, (b) Conventional grid current feedback-based FCS-MPC with Np=6.

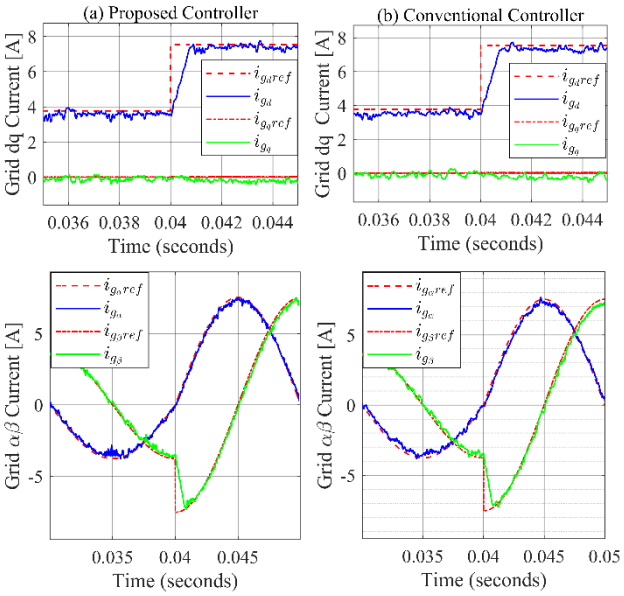

Fig. 5. Transient dq and αβ grid injected current and its references for a step-up from 1.5~kW to 3~kW: (a) Proposed FCS-MPC with N_p=3, (b) Conventional grid current feedback-based FCS-MPC with N_p=6.

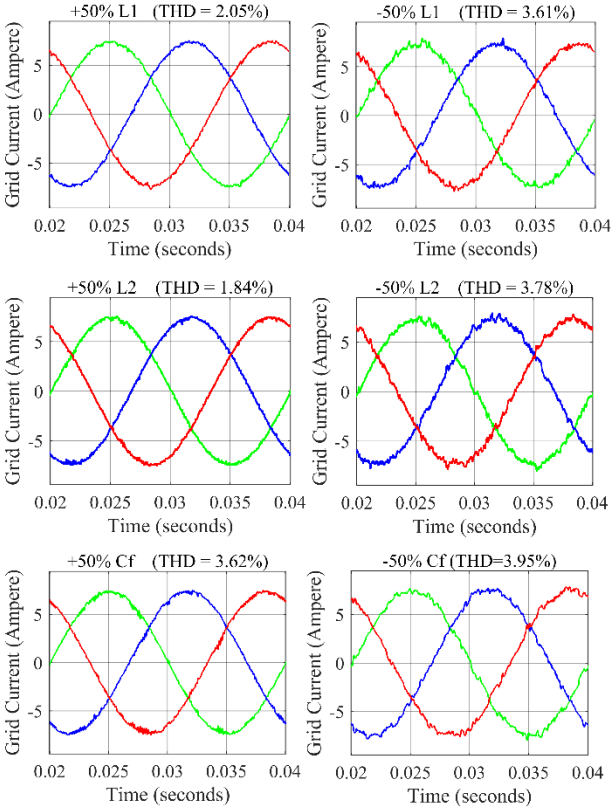

Fig. 6. Grid-injected current waveforms under mismatch parameters.

To further substantiate the robustness of the proposed controller, its performance was evaluated under weak grid conditions, a common scenario characterized by parameter mismatches. In this assessment, the grid inductance was significantly increased from 0.5 mH to 5 mH. Fig.7 presents the waveforms of the PCC voltage, filter voltage, inverter-side current, and grid-injected current. As shown, despite the grid

voltage exhibiting a high harmonic content, with a THD of 6.03%, the proposed controller successfully maintained the injection of a near-sinusoidal current into the grid, achieving a current THD of only 2.01%. This demonstrates the controller's strong resilience to substantial grid impedance variations and weak grid conditions.

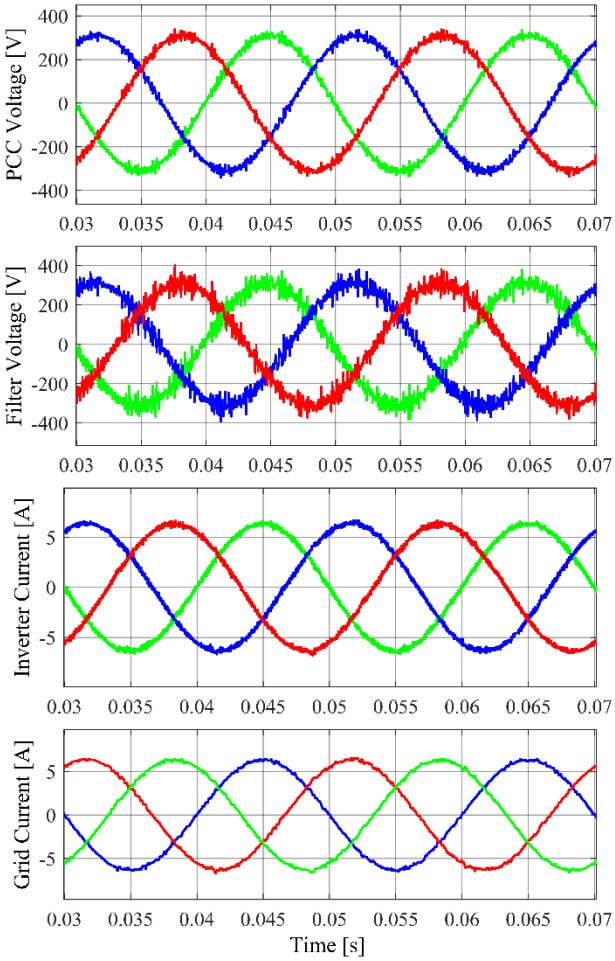

Fig. 7. PCC Voltage, filter voltage, inverter current, and grid-injected current waveforms with grid inductance increased to 5 mH.

To further challenge the system, the grid inductance was increased to $20mH$. In this more severe case, the PCC voltage THD increased to 13.07%, while the grid-injected current THD exhibited only a slight increase to 2.23% as shown in Fig.8, further confirming the effectiveness and robustness of the proposed control strategy under highly adverse grid conditions. Table I summarizes the grid-injected current THD of the proposed FCS-MPC for different operation scenarios.

Table 1. Grid-injected current THD

Op. Scenario	THD_i	Op. Scenario	THD_i
Steady state	1.7%	$+50\%\ L_{grid}$	1.84%
Step change	1.7%	$-50\%\ L_{grid}$	3.78%
$+50\%\ L_{inv}$	2.05%	$+50\%\ C_f$	3.62%
$-50\%\ L_{inv}$	3.61%	$-50\%\ C_f$	3.95%
$Z_g = 5(mH)$	2.01%	$Z_g = 20(mH)$	2.23%

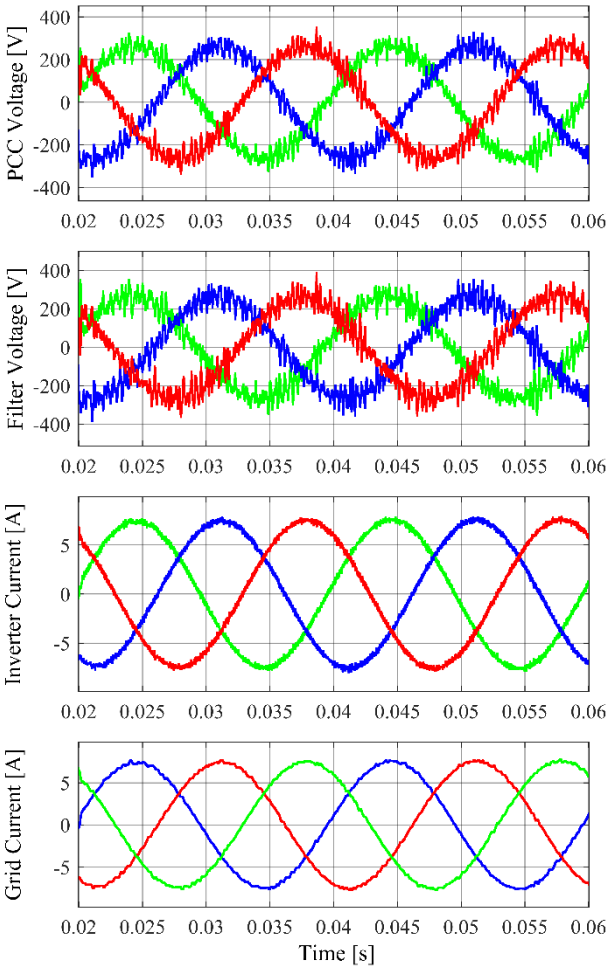

Fig. 8. PCC Voltage, filter voltage, inverter current, and grid-injected current waveforms with grid inductance increased to 20 mH.

As previously described, the proposed controller extracts the reference current based on the positive sequence of the PCC voltage. This design strategy enables the controller to track only the positive sequence component, thereby ensuring that balanced currents are injected into the grid even under unbalanced voltage conditions. To evaluate the controller's performance under such circumstances, simulations were carried out for two test cases.

In the first case, a 30% voltage sag was introduced on phases B and C, occurring between $0.1\ s$ and $0.2s$. Fig.9 illustrates the PCC voltage and the grid-injected current waveforms for this scenario. As shown, the proposed controller successfully maintains the injection of balanced currents into the grid throughout the voltage sag period.

In the second case, the grid voltage was defined with positive and negative sequence components of $(v^+ = 0.5\,pu)$ with a 180-degree phase shift, and $(v^- = 0.3\,pu)$ with a 120-degree phase shift, respectively. This setup emulates a more severe unbalanced voltage sag. The corresponding PCC voltage and grid-injected current waveforms are presented in Fig.10. As observed, the proposed controller effectively maintains balanced current injection into the grid despite the significant voltage imbalance.

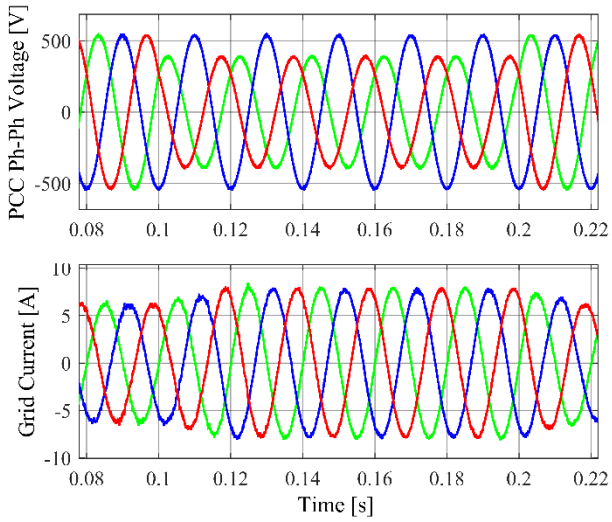

Fig. 9. PCC voltage and grid-injected current waveforms during a 30% voltage sag on phases B and C.

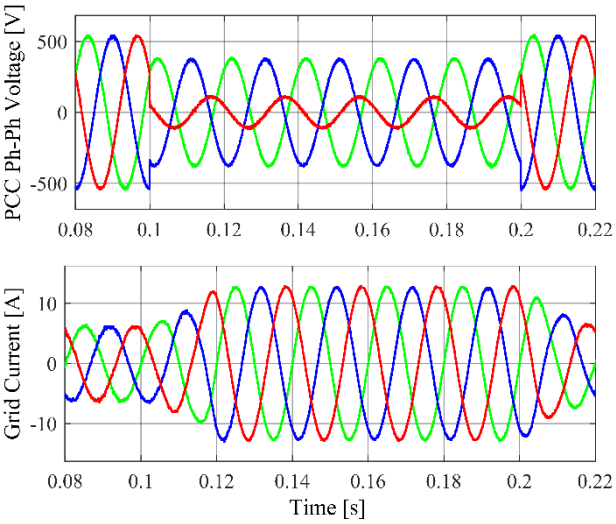

Fig. 10. PCC voltage and grid-injected current waveforms under unbalanced voltage sag with defined positive and negative sequence components.

5.2 Experimental Results

The performance of the proposed controller was experimentally validated using the ECOSENSE Wind Turbine RL Emulator as a real-time embedded system. The experimental setup for this emulator is shown in Fig.11. This system emulates wind turbine behavior by utilizing a DC motor coupled with a permanent magnet synchronous generator (PMSG), along with back-to-back converters and a battery storage system connected through a bidirectional converter to maintain the balance between generation and load. This system utilizes an NI sbRIO GPIC evaluation kit with the sbRIO-9683 RIO Mezzanine Card and the sbRIO-9606 processor and FPGA card as a real-time embedded controller.

The single-line block diagram of the system is presented in Fig.12, and its main parameters are listed in Table II. In this study, a constant wind speed was assumed with constant DC Bus voltage maintained by Turbine-side converter, and the proposed FCS-MPC controller was applied to the grid-side inverter.

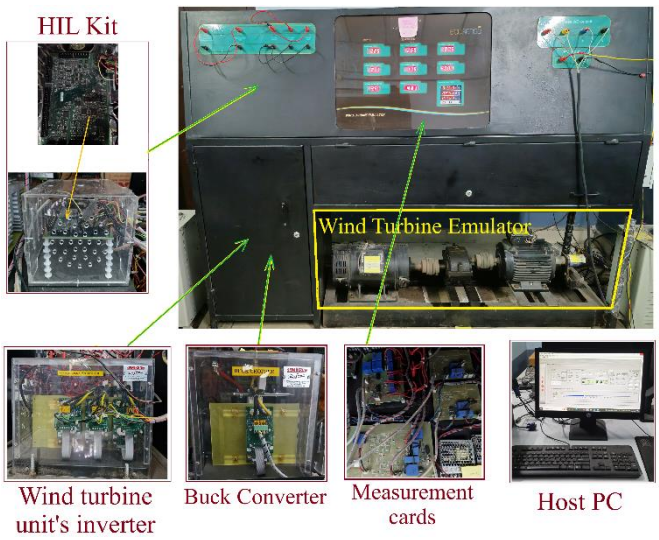

Fig. 11. Experimental setup with some internal parts.

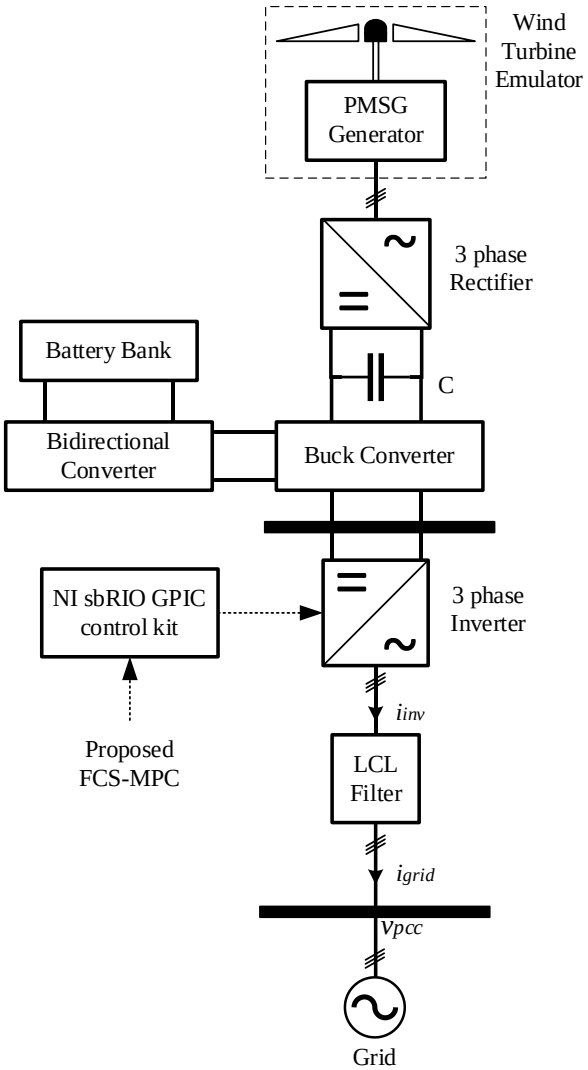

Fig. 12. Block diagram of the experimental setup.

Table 2. Experimental system parameters

Parameter	Value	Description
v_{grid}	380 v	Ph-Ph voltage of the main grid
v_{dc}	500 v	DC bus voltage.
f	50 Hz	Main grid frequency.
T_s	25 μs	Sampling time.
L_{inv}	18 mH	inverter-side inductance of the LCL filter
C_f	25 μF	LCL filter Capacitor
L_g	0.8 mH	Grid-side inductance of the LCL filter

The steady-state performance of the proposed system was experimentally assessed by setting a constant active power reference of 500 [W] while maintaining unity power factor (Q=0 [var]). The corresponding grid-injected current waveforms and instantaneous active power are shown in Fig.13 and Fig.14, respectively. It is evident from the results that the proposed controller, even with a reduced prediction horizon, successfully maintained the desired steady-state behavior and achieved balanced current injection with minimal harmonic distortion. The computational time of the proposed FCS-MPC was measured at 25.3 µs on the 400 MHz sbRIO platform. In stark contrast, the conventional FCS-MPC with Np=6 required 7.8 ms, making it over 300 times slower. This decisive result demonstrates that the proposed method is perfectly suited for real-time implementation on this processor, whereas the conventional approach is computationally prohibitive and would require significantly more powerful hardware.

To further evaluate the dynamic performance of the proposed FCS-MPC controller, the system was subjected to a step change in the active power reference from 500 [W] to 750 [W]. Fig.15 and Fig.16 illustrate the grid-injected current waveforms and the active power response during this transient event. As observed, the controller exhibited excellent reference tracking capability with negligible steady-state error and no observable overshoot, demonstrating its robustness and fast dynamic response under sudden changes in operating conditions.

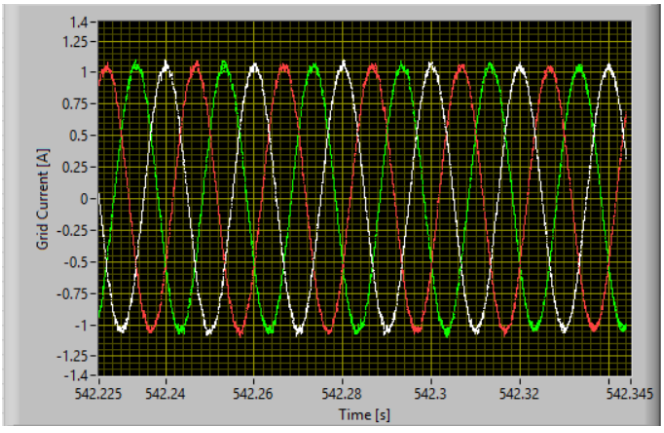

Fig. 13. Experimental result of the grid-injected current in steady state condition.

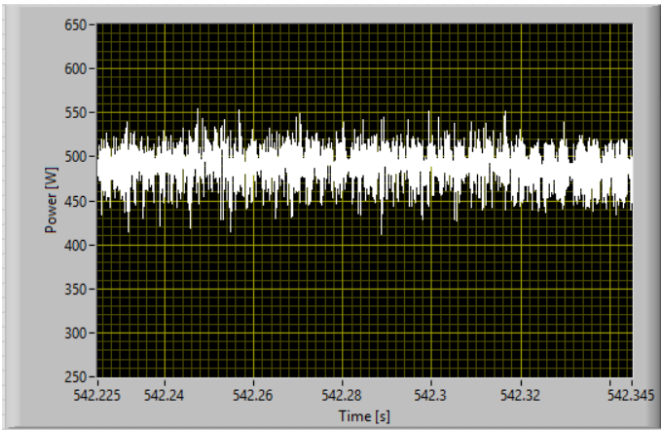

Fig. 14 Experimental result of the active power injected into the grid in steady state condition.

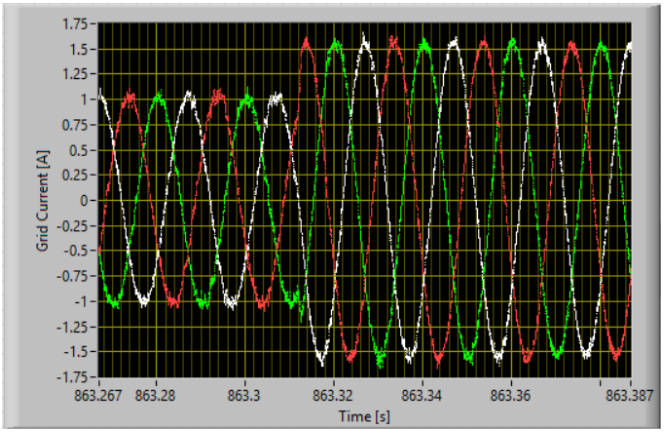

Fig. 15. Experimental result of the grid injected current during step change of the active power reference from 500 to 750 [w]

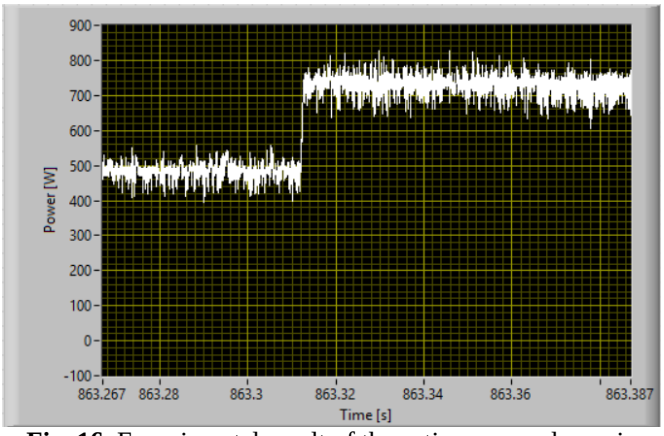

Fig. 16. Experimental result of the active power dynamic response during step change of the active power reference from 500 to 750 [w].

To validate the performance of the proposed FCS-MPC strategy under weak grid conditions, a 5 mH inductance was connected between the grid and the point of common coupling (PCC) to emulate a high grid impedance scenario. The system was operated with an active power reference of 500 [W] while maintaining unity power factor operation, corresponding to a reactive power reference of 0 [VAR]. Fig.17 presents the PCC voltage waveforms under these conditions, where it can be observed that the addition of the inductance introduces

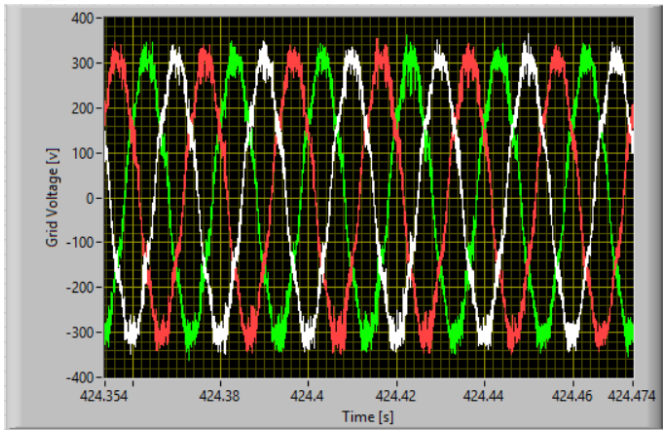

Fig. 17. Experimental result of the PCC voltage under a weak grid condition.

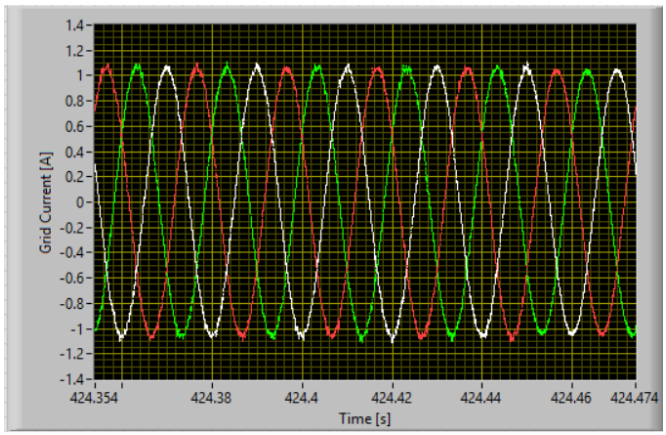

Fig. 18. Experimental result of the grid-injected current under a weak grid condition.

significant distortion into the grid voltage. Despite this adverse condition, the proposed controller effectively maintained stable operation. Fig.18 illustrates the grid-injected current waveforms, demonstrating that the controller successfully regulated the inverter output, preventing the voltage distortion from propagating into the current waveforms. Furthermore, Fig.19 shows the corresponding active power injected into the grid. It is evident that the proposed FCS-MPC controller accurately tracks the active power reference, delivering the commanded power without being affected by the voltage distortion at the PCC. These results confirm the robustness and effectiveness of the proposed control strategy under weak grid conditions.

6. Conclusion

This paper proposed a simple, weighing-factorless finite control set model predictive control (FCS-MPC) strategy for grid-connected microgrids equipped with LCL filters. By tracking the filter capacitor voltage rather than directly controlling the grid-side current, the proposed approach achieved accurate reference tracking with a significantly reduced prediction horizon (Np = 3), thereby addressing the computational complexity issues associated with conventional methods requiring longer horizons and consequently addressed the design complexity by avoiding the weighing factors in the cost function.

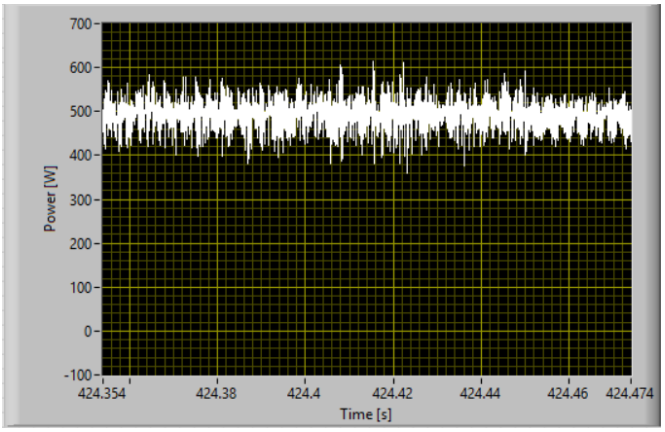

Fig. 19. Experimental result of the instantaneous active power under a weak grid condition.

Both simulation and experimental results validated the effectiveness of the proposed controller under a wide range of operating conditions, including steady-state operation, dynamic power reference changes, parameter mismatches, and weak grid scenarios characterized by high grid impedance and severe voltage distortions.

The performance of the proposed controller is comparable to the conventional method, achieving a grid-current THD of 1.7% in steady-state and 2.23% under a severely weak grid (20 mH grid impedance), while reducing the prediction horizon by 50%. Furthermore, it demonstrated superior steady state and dynamic performance, achieving low injected-current THD, accurate active power tracking, and robust operation without requiring complex weighting factor adjustment. Critically, the experimental implementation confirmed a computational time of just 25.3 µs for the proposed method, over 300 times faster than the 7.8 ms required by the conventional Np=6 approach, making it uniquely suitable for real-time execution on embedded hardware.

Overall, the proposed FCS-MPC strategy offers an efficient and reliable control solution for grid-connected microgrids, ensuring high power quality and reduced computational burden, and showing strong potential for practical deployment in real-world renewable energy integration.

Acknowledgment

The experimental work presented in this paper was supported by the Science and Engineering Research Board (SERB), Government of India, under the Core Research Grant (CRG) project CRG/2018/002041. The support from both institutions is sincerely appreciated.

Author Contributions

A. Tatish was responsible for the conceptualization, data curation, formal analysis, investigation, methodology, validation, writing original draft, review and editing. K. Vaisakh was the project administrator, supervised and guided the overall work. All authors have read and agreed to the published version of the manuscript.

Conflict of Interest

The author(s) declared no potential conflicts of interest with respect to the research, authorship, and/or publication of this article.

References

[1] A. Gulraiz, M. A. Khan, S. Ahmed, and R. Hussain, "Impact of Photovoltaic Ingress on the Performance and Stability of Low Voltage Grid-Connected Microgrids," Results in Engineering, p. 105030, 2025.

[2] M. Ganjian-Aboukheili, M. Shahabi, Q. Shafiee, and J. M. Guerrero, "Linear Quadratic Regulator Based Smooth Transition between Microgrid Operation Modes," IEEE Transactions on Smart Grid, vol. 12, no. 6, pp. 4854–4864, 2021, doi: 10.1109/TSG.2021.3094419.

[3] L. Yang, X. He, P. Zhang, and S. Liu, "Control scheme and performance analysis of dual-frequency single-phase grid-connected inverter interfaced with weak and distorted grids," IEEE Access, vol. 8, pp. 178639–178650, 2020, doi: 10.1109/ACCESS.2020.3022106.

[4] Y. Han, W. Li, H. Lin, and X. Chen, "Modeling and stability analysis of LCL-type grid-connected inverters: A comprehensive overview," IEEE Access, vol. 7, pp. 114975–115001, 2019, doi: 10.1109/ACCESS.2019.2935806.

[5] S. Jahan, S. P. Biswas, S. Haq, M. R. Islam, M. A. P. Mahmud, and A. Z. Kouzani, "An Advanced Control Scheme for Voltage Source Inverter Based Grid-Tied PV Systems," IEEE Transactions on Applied Superconductivity, vol. 31, no. 8, pp. 1–5, 2021, doi: 10.1109/TASC.2021.3094446.

[6] A. Ahmed, S. P. Biswas, M. S. Anower, M. R. Islam, S. Mondal, and S. M. Muyeen, "A Hybrid PWM Technique to Improve the Performance of Voltage Source Inverters," IEEE Access, vol. 11, pp. 4717–4729, 2023, doi: 10.1109/ACCESS.2023.3235791.

[7] S. Kouro, P. Cortés, R. Vargas, U. Ammann, and J. Rodríguez, "Model predictive control - A simple and powerful method to control power converters," IEEE Transactions on Industrial Electronics, vol. 56, no. 6, pp. 1826–1838, 2009, doi: 10.1109/TIE.2008.2008349.

[8] D. M. R. Korada and M. K. Mishra, "Fixed Switching Frequency Model Predictive Current Control for Grid-Connected Inverter With Improved Dynamic and Steady State Performance," IEEE Access, vol. 11, pp. 104094–104105, 2023, doi: 10.1109/ACCESS.2023.3317537.

[9] C. Bao, X. Ruan, X. Wang, W. Li, D. Pan, and K. Weng, "Step-by-step controller design for LCL-Type Grid-Connected inverter with capacitor-current-feedback active-damping," IEEE Transactions on Power Electronics, vol. 29, no. 3, pp. 1239–1253, 2014, doi: 10.1109/TPEL.2013.2262378.

[10] K. H. Ang, G. Chong, and Y. Li, "PID control system analysis, design, and technology," IEEE Transactions on Control Systems Technology, vol. 13, no. 4, pp. 559–576, 2005, doi: 10.1109/TCST.2005.847331.

[11] H. T. Do, X. Zhang, N. V. Nguyen, S. S. Li, and T. T. T. Chu, "Passive-Islanding Detection Method Using the Wavelet Packet Transform in Grid-Connected Photovoltaic Systems," IEEE Transactions on Power Electronics, vol. 31, no. 10, pp. 6955–6967, 2016, doi: 10.1109/TPEL.2015.2506464.

[12] K. T. Tan, P. L. So, Y. C. Chu, and M. Z. Q. Chen, "Coordinated Control and Energy Management of Distributed Generation Inverters in a Microgrid," IEEE Transactions on Power Delivery, vol. 28, no. 2, pp. 704–713, 2013, doi: 10.1109/TPWRD.2013.2242495.

[13] P. Falkowski, A. Sikorski, and M. Malinowski, "Finite control set model predictive control with floating virtual voltage vectors for grid-connected voltage source converter," IEEE Transactions on Power Electronics, vol. 36, no. 10, pp. 11875–11885, 2021, doi: 10.1109/TPEL.2021.3067602.

[14] S. Vazquez, J. Rodriguez, M. Rivera, L. G. Franquelo, and M. Norambuena, "Model Predictive Control for Power Converters and Drives: Advances and Trends," IEEE Transactions on Industrial Electronics, vol. 64, no. 2, pp. 935–947, 2017, doi: 10.1109/TIE.2016.2625238.

[15] P. Karamanakos, M. Nahalparvari, and T. Geyer, "Fixed Switching Frequency Direct Model Predictive Control With Continuous and Discontinuous Modulation for Grid-Tied Converters With LCL Filters," IEEE Transactions on Control Systems Technology, vol. 29, no. 4, pp. 1503–1518, 2020, doi: 10.1109/TCST.2020.3008030.

[16] P. Cortes, G. Ortiz, J. I. Yuz, J. Rodriguez, S. Vazquez, and L. G. Franquelo, "Model predictive control of an inverter with output LC filter for UPS applications," IEEE Transactions on Industrial Electronics, vol. 56, no. 6, pp. 1875–1883, 2009, doi: 10.1109/TIE.2009.2015750.

[17] V. Yaramasu, M. Rivera, M. Narimani, B. Wu, and J. Rodriguez, "Model predictive approach for a simple and effective load voltage control of four-leg inverter with an output LC filter," IEEE Transactions on Industrial Electronics, vol. 61, no. 10, pp. 5259–5270, 2014, doi: 10.1109/TIE.2013.2297291.

[18] P. Cortes, J. Rodriguez, S. Vazquez, and L. G. Franquelo, "Predictive control of a three-phase UPS inverter using two steps prediction horizon," Proceedings of the IEEE International Conference on Industrial Technology, pp. 1283–1288, 2010, doi: 10.1109/ICIT.2010.5472535.

[19] T. Dragicevic, "Model Predictive Control of Power Converters for Robust and Fast Operation of AC Microgrids," IEEE Transactions on Power Electronics, vol. 33, no. 7, pp. 6304–6317, 2018, doi: 10.1109/TPEL.2017.2744986.

[20] N. Panten, N. Hoffmann, and F. W. Fuchs, "Finite Control Set Model Predictive Current Control for Grid-Connected Voltage-Source Converters with LCL Filters: A Study Based on Different State Feedbacks," IEEE Transactions on Power Electronics, vol. 31, no. 7, pp. 5189–5200, 2016, doi: 10.1109/TPEL.2015.2478862.

[21] P. Falkowski and A. Sikorski, "Finite Control Set Model Predictive Control for Grid-Connected AC-DC Converters with LCL Filter," IEEE Transactions on Industrial Electronics, vol. 65, no. 4, pp. 2844–2852, 2018, doi: 10.1109/TIE.2017.2750627.

[22] A. Bakeer and I. S. Mohamed, "An Artificial Neural Network-Based Model Predictive Control for Three-Phase Flying Capacitor Multilevel Inverter," IEEE Access, vol. 10, pp. 70305–70316, 2022, doi: 10.1109/ACCESS.2022.3187996.

[23] M. Babaie, K. Al-Haddad, and L. Franquelo, "Self-Training Intelligent Predictive Control for Power Converters," IEEE Transactions on Power Electronics, vol. 38, no. 1, pp. 12482–12496, 2023, doi: 10.1109/TPEL.2023.3293820.

[24] L. Tang, W. Xu, X. Wang, D. Dong, X. Xiao, and Y. Zhang, "Weighting Factors Optimization of Model Predictive Control Based on Fuzzy Thrust Constraints for Linear Induction Machine," IEEE Transactions on Applied Superconductivity, vol. 31, no. 8, pp. 1–5, 2021, doi: 10.1109/TASC.2021.3103704.

[25] S. Vazquez, J. Rodriguez, M. Rivera, L. G. Franquelo, and M. Norambuena, "Model predictive control: A review of its applications in power electronics," IEEE Industrial Electronics Magazine, vol. 8, no. 1, pp. 16–31, 2014, doi: 10.1109/MIE.2013.2290138.

[26] B. H. Bae and S. K. Sul, "A compensation method for time delay of full-digital synchronous frame current regulator of PWM AC drives," IEEE Transactions on Industry Applications, vol. 39, no. 3, pp. 802–810, 2003, doi: 10.1109/TIA.2003.810660.

[27] P. Cortes, J. Rodriguez, C. Silva, and A. Flores, "Delay compensation in model predictive current control of a three-phase inverter," IEEE Transactions on Industrial Electronics, vol. 59, no. 2, pp. 1323–1325, 2012, doi: 10.1109/TIE.2011.2157284.

[28] E. Pouresmaeil, C. Miguel-Espinar, M. Massot-Campos, D. Montesinos-Miracle, and O. Gomis-Bellmunt, "A control technique for integration of DG units to the electrical networks," IEEE Transactions on Industrial Electronics, vol. 60, no. 7, pp. 2881–2893, 2013, doi: 10.1109/TIE.2012.2209616.

International Journal of Smart Grid (IJSmartGrid)
https://www.ijsmartgrid.org/ Online ISSN: 2602-439X
B. Tasdemir and M. Yaz, Vol. 10, No. 1, March, 2026 Research Article

Comparative Short-Term Wind Energy Forecasting Using Hybrid JAYA-ANN, GRU-ANN, and VMD-ANN Models

Bahtiyar Tasdemir*‡, Mustafa Yaz**

*Department of Electrical and Electronics Engineering, Yozgat Bozok University, Yozgat, Turkey

**Department of Electrical and Electronics Engineering, Yozgat Bozok University, Yozgat, Turkey

(bahtiyartasdemir1830@gmail.com, Mustafa.yaz@yobu.edu.tr)

‡Bahtiyar Tasdemir; Yozgat Bozok University, Yozgat, Turkey, Tel: +90 354 242 10 02,

Fax: +90 354 217 89 91, bahtiyartasdemir1830@gmail.com

Received: 21.11.2025 Accepted: 21.01.2026

Abstract- Wind power generation is directly dependent on weather conditions, so it is very difficult to predict how much energy will be generated in a given time period. The main objective of this study is to predict wind power generation more accurately by comparing an Artificial Neural Network (ANN)-based forecasting model with JAYA-ANN, Gated Recurrent Unit (GRU)-ANN, and Variational Mode Decomposition (VMD)-ANN hybrid models. Wind direction, particulate matter (PM10), temperature, and historical power data for summer and spring seasons were collected to estimate the daily wind power generation capacity. Of the collected data, 80% was divided into a training set, 10% into a validation set, and 10% into a test set, and appropriate modelling methods were applied. The performance of the models was evaluated with Mean Absolute Percentage Error (MAPE), Root Mean Squared Error (RMSE), and Mean Absolute Error (MAE) error measures. According to the prediction results of MAPE, RMSE, and MAE values of ANN, VMD-ANN, GRU-ANN, and JAYA-ANN hybrid models in summer and spring seasons, the JAYA-ANN hybrid model is better than other prediction models and provides higher forecasting accuracy. Such a forecasting model can be an important guide for energy planners and local electricity providers for generation planning and management of alternative energy sources.

Keywords Artificial neural network, wind energy, hybrid learning, forecasting.

1. Introduction

The world energy deficit and environmental pollution have become increasingly severe. Many developing countries are increasingly opting for renewable energy sources in electricity generation. This method not only allows individuals to meet their own household energy needs but also enables them to sell any surplus electricity they generate to connected energy providers [1]. Wind energy has been recognised as a cleaner and renewable energy source and has been included in the country's national long-term energy promotion strategy. According to the Global Wind Energy Council, the total installed wind power capacity of the world has reached 1 TW according to the 2024 report [2]. However, the intermittent and variable nature of wind power raises a number of problems, included those related to the stability of wind power supplies and the sensitive balance between the management and capacity in reserve [3]. Thus, forecasting of reliable wind power is essential for the security of the power grid and for pre-determining the power strategy [4], [5].

Cite this article as: B. Tasdemir and M. Yaz, "Comparative Short-Term Wind Energy Forecasting Using Hybrid JAYA-ANN, GRU-ANN, and VMD-ANN Models" *International Journal of Smart Grid (ijSmartGrid)*, Vol. 10, No. 1, pp. 14-29, March, 2026.

Existing methods for wind energy prediction mainly consist of statistical modelling and physical models [6]. Physical methods rely on advanced mathematical models to make predictions. These methods utilize numerical weather forecast data provided by meteorological services, which analyze the behavior and physical dynamics of the lower atmosphere to forecast future weather conditions. Additionally, they take into account the topography of the wind farm's location. However, a major drawback of physical models is their dependence on highly precise online and offline data [7]. They are also computationally intensive and demand substantial resources [8]. Physical methods excel in medium- and long-term forecasting, but their accuracy diminishes for short-term predictions. In contrast, statistical methods focus on identifying linear and non-linear relationships between weather variables such as wind speed, direction, temperature and the wind power generated [9]. These methods rely on historical data to train models that establish these connections. While statistical models are well-suited for short-term wind forecasting, their accuracy decreases as the forecasting horizon extends. They are relatively simple to implement and involve minimal computation time. To enhance performance, these models are periodically updated by comparing predicted and actual power values, allowing forecasts to improve over time.

Physical, statistical, and machine learning-based methods have made significant advances in wind energy forecasting and various other disciplines, demonstrating the diversity and potential of the field. Environmental studies integrating machine and deep learning techniques, in particular, have achieved high accuracy [10].

This study systematically analyzes selected works published between 2021 and 2023, focusing on estimation time, data set size, model structures, and evaluation criteria, as summarized in Table 1. The comprehensive literature review indicates that, despite notable progress, several fundamental challenges remain unresolved.

In this study, meteorological and wind farm data commonly utilized in daily wind power forecasting are employed. Initially, an ANN based forecasting model is developed and evaluated using wind direction, PM10 concentration, temperature, and historical power output data. Subsequently, three hybrid models JAYA-ANN, GRU-ANN, and VMD-ANN are constructed using the same dataset and compared against the standalone ANN model. The results indicate that the hybrid models exhibit superior forecasting performance. This study provides a meaningful contribution to the academic literature on short-term wind energy forecasting. Furthermore, the integration of the JAYA-ANN hybrid model and the inclusion of the PM10 parameter both of which have not been previously applied in wind energy forecasting constitute a significant innovation introduced by this research.

2. Methodology

In this section ANN, JAYA, GRU, and VMD algorithms used in the construction of hybrid forecasting models are presented in detail. The overall training architecture is illustrated in Figure 1. In the proposed approach, the JAYA, GRU, and VMD algorithms are employed to optimize the internal parameters of the ANN, namely the weights and biases of the multilayer perceptron. These optimization algorithms receive the ANN parameters as input vectors and iteratively adjust them to minimize forecasting error. The objective function guiding this optimization process is based on widely used error metrics, including RMSE, MAE, and MAPE.

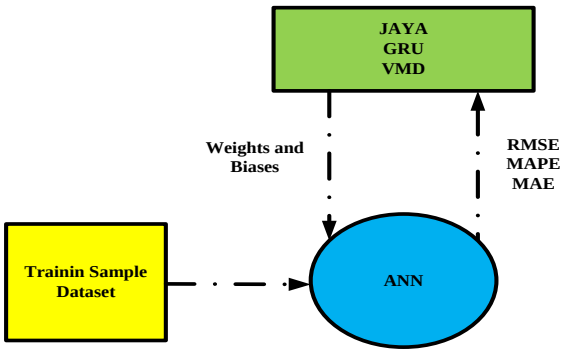

Fig. 1. Architecture of training examples.

2.1. Artificial Neural Networks

Artificial Neural Networks are non-linear mapping systems designed to emulate the workings of the human central nervous system. At their core lies the basic building block: the neuron. The first ANN model, introduced by McCulloch and Pitts in 1943, laid the foundation for concepts that remain relevant today [18]. ANNs can also be characterized as highly parallel processors made up of simple processing units capable of learning from experience and applying this knowledge to make future decisions [19]. ANNs are robust prediction tools for situations where the relationship between data is unknown and needs to be established. They learn from any observed patterns in the relationships between input datasets and target values in the training dataset. Once an ANN is trained, it can predict future outcomes based on the identified patterns and connections derived from the training dataset.

ANNs are particularly well-suited for processing data that are uncertain, noisy, or exhibit occasional irregular variations, making them highly effective for modeling complex real-world phenomena. Consequently, ANNs are ideal for forecasting both wind speed and wind power, as they can capture complex, non-linear dependencies that traditional linear models may fail to represent accurately [18].

Their highly interconnected nodes allow neural networks to learn intricate patterns from the training data and generalize these patterns to unseen data in a manner that loosely resembles the adaptive and learning processes of the human brain. This capacity for learning, adaptation, and generalization represents one of the principal advantages of ANNs, particularly in forecasting applications where input-output relationships are dynamic, stochastic, and potentially noisy. Figure 2 illustrates the fundamental architecture of an artificial neural cell, highlighting the interconnections and the flow of information through the network.

Table 1. Lists illustrative research on wind energy power forecasting from 2021 to 2023

Year	Ref.	Period	Dataset length	Forecast model	Forecast error	Comments
2023	S. M. Malakouti [11]	1 h	One and a half months	Random Forest Ada Boost K - Neighbors	MSE=21-2340.8-32286.9 kW RMSE=4.6-48.38-179.68 kW MAE=2.56-38.09-116.62 kW MAPE=0.0079-2.78-16.33 % R^2=1-0.997-0.95	Random Forest demonstrated superior predictive performance, whereas KNN exhibited lower accuracy despite faster computation.
2023	Gao et al. [12]	15 minutes	3000 sample points	SSA-VMD-LSTM	MAE=1.4139 RMSE=2.0296 MAPE=0.0849 %	The results show that the SSA-VMD-LSTM method gives better prediction accuracy and lower wind power error than other methods, proving the model is effective.
2023	Alkabbani et al. [13]	1 h	3 years	MIMO ANN MIMO LSTM	R^2=0.77-0.77 MSE=1.83-1.68 RMSE=427.78-409.88 MW MAPE=27.5-26.6 %	Multi-input multi-output (MIMO) LSTM approach are more reliable with higher accuracies.
2022	Xiong et al. [14]	1 h/ 2h 3 h	1 years	AMC-LSTM	MAE=0.0509-0.0517-0.0519 RMSE=0.0949-0.0954-0.0948 MSE=0.8951-0.9112-0.8990	The proposed wind power forecasting model has lower error, higher accuracy, and better matches the actual data compared to other models.
2022	Zhu et al. [15]	1 h	6 month	CEEMDAN-SVR-TCN	MAE=68.4695-75.7741-75.21 RMSE=87.9475-98.9572-100 MSE=3.3726-3.7948-3.835	Using real wind power data, the proposed method shows better accuracy than other models, proving its effectiveness.
2022	He et al. [16]	15 minutes	16 month	IOWA-CNN-LSTM	RMSE=12.154 MAE=8.0608	The proposed model has the lowest MAE and RMSE among the five models, showing it is reliable and effective.
2021	Chandran et al. [17]	10 minutes	50.530 data	LSTM GRU RNN	MSE=0.1358-0.13-0.143	The GRU network is particularly well-equipped to capture highly non-linear and complex patterns in real-time data.

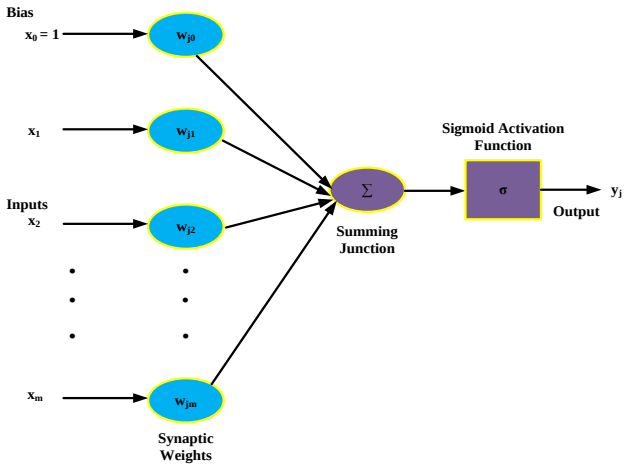

Fig. 2. Artificial neural cell architecture.

Where:

- X_1 and x_m represent the inputs of the neuron.
- X_0 represents the bias. The bias helps neurons activate meaningfully. It determines the threshold at which a neuron activates; otherwise, the neuron remains inactive.
- W_{j0} and w_{jm} represent the respective synaptic weights connecting each input to neuron j.
- Y_j is the output signal of the neuron.

The output of the summation function is shown as (s_j) in equation 1:

$$s_j = \sum_{m=0}^{m} w_{jm} x_m \quad (1)$$

The sum of the weights is then passed through an activation function (σ) to compress it into a specific small value range. In Equation 2, the output obtained from the activation function is the output of the neuron (y_j).

$$y_j = \sum_{m=0}^{m} \sigma(s_j) \quad (2)$$

In this study, an ANN model with 4 input layers, one hidden layer, and one output layer is used for daily wind energy power forecasting. In the structure of ANN, a single hidden layer with 5 neurons and a sigmoid activation function is used because it is easy to calculate the derivative by compressing the inputs between 0 and 1 [20]. The trial-and-error method was adopted to determine the number of neurons in the hidden layer. As a result of the experiments, the best network topologies for each product series are shown in Table 2.

Table 2. Performance of the developed ANN model

Model Used	Fuction	Neuron Count	MAPE (%)	RMSE (MW)	MAE (MW)
ANN	Sigmoid	5	19.59	22.63	1.28
ANN	Sigmoid	10	20.71	24.46	1.78
ANN	Sigmoid	15	23.25	26.19	2.15
ANN	Sigmoid	20	25.89	28.28	2.45

Artificial neural networks are classified into feedforward networks and feedback networks based on their structures.

2.2. Feedforward Neural Networks

In feedforward artificial neural networks, processing elements are typically organized in layers. Signals are transmitted in a unidirectional manner from the input layer to the output layer through connections. In a feedforward ANN, cells are arranged in layers, and the outputs of the cells in each layer are transferred as inputs to the next layer with weights. The input layer sends information received from the external environment directly to the cells in the hidden layer without any modifications. The information is processed in the hidden and output layers to obtain the network's result output [21]. Figure 3 shows the feed-forward network structure.values in the training dataset. X_s represent inputs, and Y_s represent outputs.

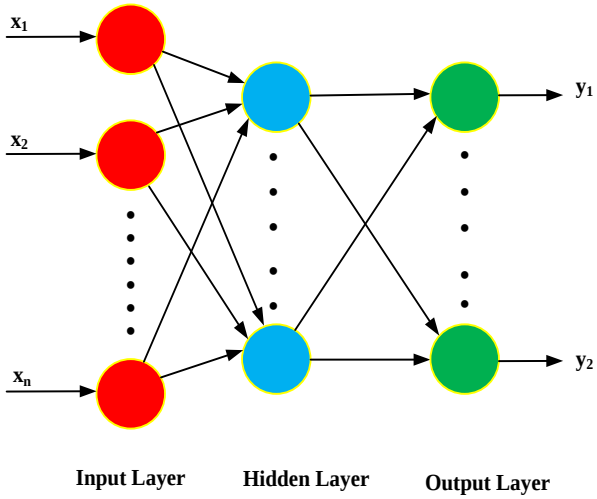

Fig. 3. Feedforward network structure.

In this study, we chose ANN as our base model because it is lightweight, widely used in the literature, and suitable for the size of our dataset. This allows us to clearly evaluate the contribution of our proposed method independently of the effects of complex deep architectures. The feedforward neural network structure is preferred to solve problems due to its prediction ability and its success in tasks such as pattern recognition, visual recognition, and time series prediction.

2.3. Feedback Neural Networks

Recurrent or feedback artificial neural networks have a variable structure, unlike feedforward networks. In these networks, neurons in the output or intermediate layers send their outputs back to the input layer or previous intermediate layers. Thus, information is transmitted both forward and backward. Feedback neural networks have dynamic memory, where the output at any given time is a reflection of both the current and previous inputs. In feedback neural networks, the output of at least one processing element is fed back either to itself or to other elements, and this feedback is typically provided through a delay element. Feedback occurs not only between processing elements but also between layers. Due to

this structure, feedback neural networks exhibit nonlinear dynamic behaviors. As a result, depending on how the feedback is implemented, these networks can appear in different structures and behaviors [22]. Figure 4 shows the feedback neural network structure.

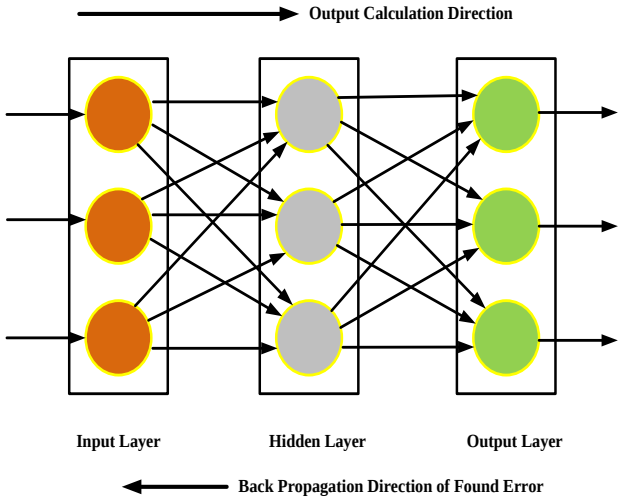

Fig. 4. Feedback network structure.

2.4. Jaya Algorithm

The basic Jaya algorithm, while having many advantages in solving various optimization problems, also has some disadvantages, such as low accuracy and slow convergence, particularly for complex and high-dimensional problems, due to the challenges in balancing the search and development processes. In recent years, many researchers have made various improvements to address these shortcomings of the Jaya algorithm and have successfully applied the algorithm to different practical problems.

In The Jaya algorithm is a population-based metaheuristic method introduced by Rao and used for solving constrained and unconstrained continuous optimization problems. Being independent of parameters is one of the most important features that distinguish the Jaya algorithm from others. Thanks to this advantage, it can be easily adapted to optimization problems. In addition, one of the strengths of the algorithm is that it increases the tendency to move towards the best solution during location updates, while at the same time avoiding the worst solution and reducing the risk of getting stuck in the local maximum or minimum [23]. Due to these advantages, JAYA algorithm is preferred in this study.

Assume that the objective function is Z(x) to be maximized or minimized and that at any iteration 'i', 'k' is the number of design variables and 'n' is the population size. Let the best and worst values of the objective function during an iteration be denoted by $Z_{k,best,i}$ and $Z_{k,worst,i}$ respectively. Also, $X_{k,best,i}$ and $X_{k,worst,i}$ are the best and worst values of variable 'k' during iteration 'i' corresponding to $Z_{k,best,i}$ and $Z_{k,worst,i}$ in the population, respectively. The updated value is then calculated according to equation 3.

$$x'_{k,n,i} = x_{k,n,i} + r_{1,k,i}(x_{k,best,i} - |x_{k,n,i}|) - r_{2,k,i}(x_{k,worst,i} - |x_{k,n,i}|) \quad (3)$$

Here $r_{1,k,i}$ and $r_{2,k,i}$ are two random numbers between [0,1]. The term '$r_{1,k,i}$ ($X_{k,best,i}$ - $|x_{k,n,i}|$)' indicates the ability of the solution to approach the best solution, while the term '$r_{2,k,i}$ ($X_{k,worst,i}$ - $|x_{k,n,i}|$)' indicates the ability of the solution to avoid the worst solution. $X_{k,n,i}$ is accepted if it gives a superior function value. Two random numbers, $r_{1,k,i}$ and $r_{2,k,i}$ are used for the Jaya algorithm to enable better exploration of the search space. The absolute value $|x_{k,n,i}|$ used in the equation helps the algorithm to further increase its exploration ability. The JAYA algorithm used in this study was run 30 times in 1000 iterations, and the number of populations was taken as 50, which is the algorithm run parameter. Figure 5 shows the flow diagram of the JAYA algorithm.

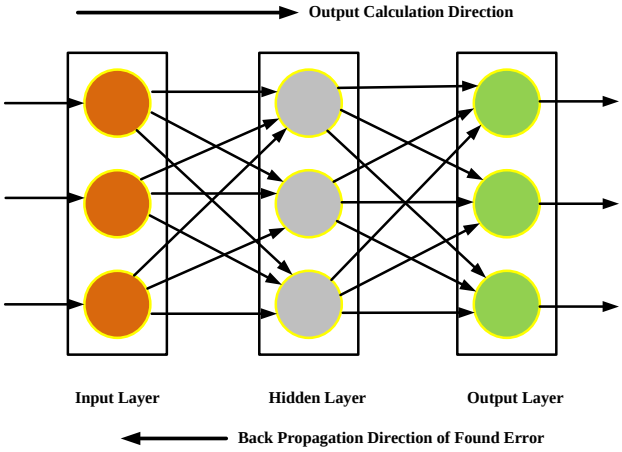

Fig. 5. Flow diagram of the JAYA algorithm.

2.5. Gated Recurrent Unit (GRU)

GRU, first proposed by Cho et al. in 2014, is a gated recurrent neural networks (RNN) derivative developed to address the inadequacies of traditional RNN in learning long-term dependencies [24]. GRU uses an update gate and a reset gate to provide a more stable learning process, especially against problems such as gradient fading and bursting, which are frequently encountered in RNNs.

Compared to the LSTM architecture, the GRU appears to have a structurally simpler design. The LSTM consists of three gates: the input gate, the forget gate, and the output gate; it also contains an additional memory unit called the cell state. GRU combines these mechanisms into two gates, integrating the cell state and the hidden state into a single structure. This simplification reduces the number of parameters and reduces the computational cost [25]. The lower computational complexity of GRU allows it to offer faster training times compared to LSTM in some applications while achieving similar accuracy levels without significant loss in performance. For this reason, GRU has become a preferred alternative, especially in systems with limited resources or online applications [26].

The GRU-based neural network architecture developed in this study is presented in detail in Figure 6. The model consists of five main components: the input layer, the GRU layer, the dropout layer, the fully connected layer, and the output layer. The GRU layer, which is at the center of this structure, acts as

the basic computational unit of the network and has the ability to learn both short-term and long-term dependencies in time series data. The GRU layer converts the data it receives from the input into temporal representation vectors, enabling their use in the subsequent layers of the network. The dropout layer, placed immediately after the GRU layer, randomly disables certain neurons during the training process, preventing the model from overfitting to certain features. This mechanism reduces overfitting by preventing reliance on specific connections. As a result, the model achieves more balanced learning and its generalization ability increases when faced with different data samples, thus making prediction performance more reliable [27]. Furthermore, the dropout layer increases the model's flexibility against different data samples, strengthening its robustness against noisy or missing data.

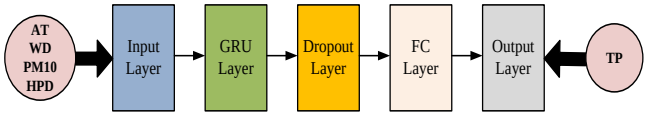

Fig. 6. Architecture of the GRU network.

As shown in Figure 7, the relevant GRU layer consists of multiple GRU blocks, and this figure also presents the schematic structure of a single GRU block. Two main control mechanisms, the reset gate and the update gate, form the basis of this architecture. The reset gate allows the network to model short-term dependencies more efficiently by determining the extent to which past memory is integrated with new input information. On the other hand, the update gate offers selective control over the extent to which the previous hidden state is maintained or updated.

As indicated in the diagram, the inputs to the GRU block are defined as the input vector X_t at the current time step and the hidden state H_{t-1} from the previous time step. As a result of the computations, a candidate latent state $\hat{H}$ is generated, and this information is updated to the final latent state H_t through the update mechanism. This process enables GRU to learn the context in temporal data more efficiently. The mathematical calculation formulas in Equations 4, 5, 6, and 7 form the quantitative basis of this process.

$$R_t = \sigma(X_t W_{xr} + H_{t-1} W_{hr} + b_r) \quad (4)$$

$$Z_t = \sigma(X_t W_{xz} + H_{t-1} W_{hz} + b_z) \quad (5)$$

$$\hat{H}_t = \tanh(X_t W_{xh} + (R_t \odot H_{t-1}) W_{hh} + b_h) \quad (6)$$

$$H_t = Z_t \odot H_{t-1} + (1 - Z_t) \odot \hat{H}_t \quad (7)$$

R_t and Z_t represent the reset gate and update gate, respectively; σ and tanh denote the sigmoid activation function and hyperbolic tangent activation function, respectively; ʘ denotes the element-wise multiplication operation. W_{xr}, W_{xz}, W_{hr}, W_{hz}, W_{xh}, and W_{hh} are the weight parameter matrices associated with the input and hidden states, while b_r, b_z, and b_h are the corresponding bias vectors. These parameters are learned during the training process and play a crucial role in regulating the flow of information within the gated recurrent unit structure, enabling the model to effectively capture temporal dependencies and nonlinear patterns in sequential data.

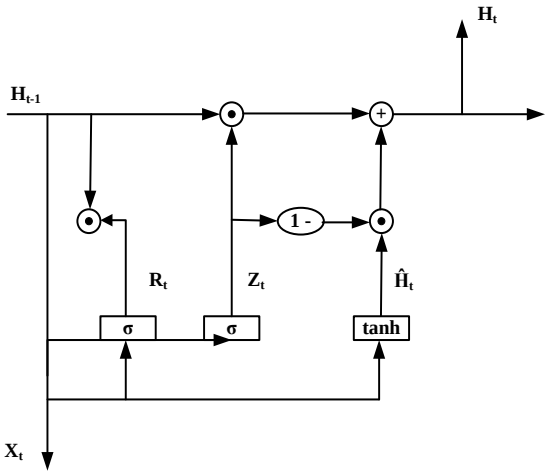

Fig. 7. Diagram of GRU block.

2.6. Variational Mode Decomposition (VMD)

Variational Mode Decomposition (VMD), developed by Dragomiretsky et al. in 2014, is a non-iterative and adaptive signal processing method formulated in a variational framework to decompose signals into predefined modes [28]. Compared to Empirical Mode Decomposition (EMD) and similar empirical approaches, VMD offers higher adaptability to signals with varying frequency content [29], superior decomposition accuracy [30], and a bandwidth-oriented control mechanism by optimizing the center frequency of each mode. Thanks to these features, VMD is often preferred in the preprocessing stage to provide reliable and meaningful feature extraction for machine learning-based models. It has been shown that VMD can decompose non-stationary signals into more discrete and information-rich components in the time-frequency plane [31]. In this context, VMD-based decomposition stands out as an effective tool to improve the performance of learning tasks such as noise suppression, pattern recognition, and classification.

$$\min\left\{\sum_{k=1}^{k} \left\| \partial_t[(\delta(t) + \frac{j}{\pi t}) u_k(t)] \exp(-j w_k t \right\|\right\}$$

$$\{u_k, w_k\} \quad (8)$$

$$s.t. \sum_{k=1}^{N} u_k = f(t)$$

In Equation 8, 'u_k' denotes the kth modal component representing each sub-signal obtained by decomposition, 'w_k' signifies the center frequency of the kth power modal component, 'j' is the imaginary unit, 'N' denotes the number of modal decompositions, 'δ(t)' is the Dirac function, i.e., the unit impulse function, '∂_t' is the derivative, and 'f(t)' is the original signal to be decomposed. The VMD based decomposition process is carried out in the following specific steps.

Step 1: Initialise $\{u_k^1\}$, $\{w_k^1\}$, λ_k^1 and n =0;

Step 2: n=n+1, enter the loop;

Step 3: The update formulas for u_k and w_k are applied iteratively until the number of parses reaches N, at which point the inner loop ends

Step 4: The value of λ is updated via an update formula at each iteration.

Step 5: Given a tolerance ϵ, the loop is terminated if the stopping condition (9) is fulfilled. In the equation, ε represents the convergence progression.

$$\sum k\|u_k^{n+1} - u_k^n\|_2^2 / \|u_k^n\|_2^2 < \epsilon \quad (9)$$

Otherwise, the loop continues with Step 2.

2.7. Persistence Reference Model (PRM)

The persistence forecasting model is a fundamental reference approach frequently employed in time series forecasting applications. Its primary advantages lie in its ease of implementation and very low computational cost. The key objective in developing more advanced forecasting models is to achieve higher forecasting accuracy than the persistence model, ideally while maintaining a similar or lower computational burden. This model operates on the assumption that the wind power output at time t+1 is highly correlated with the output at time t. Accordingly, the future wind power output is directly estimated as a continuation of the current output. This approach can demonstrate notable forecasting performance, particularly in scenarios where short-term fluctuations in wind generation are minimal.

The persistence model is commonly employed as a benchmark for evaluating the performance of various forecasting methods. However, its forecast accuracy is significantly influenced by the length of the forecast horizon; as the horizon extends, the model's accuracy tends to decline. Furthermore, variations in meteorological parameters such as temperature, solar radiation, wind speed, and humidity can considerably affect its performance. Owing to these limitations, persistence-based forecasting models typically yield higher prediction errors and are therefore widely used as baseline models for assessing the accuracy of more advanced forecasting approaches. In the study by Perez et al. [32], a comparable methodology was applied, wherein the performance of the proposed forecasting model was evaluated against the results obtained from the persistence model. The percentage improvement is defined in Equation 10. In this equation, e_{TM} is the prediction model error, e_{SRM} is the continuous reference model error, and p_{IY} is the improvement percentage. progression.

$$P_{IY} = \left(1 - \frac{e_{TM}}{e_{SRM}}\right) x100 \quad (10)$$

3. Results

The dataset was obtained from an onshore wind farm in Turkey's Central Anatolia region. This climate differs from coastal or tropical wind farms in terms of boundary layer behavior, low humidity, and stable wind regime. Therefore, direct generalization of the model is not recommended. Which comprises three different wind turbines whose specifications are summarized in Table 3. The dataset presented in Table 4 includes wind direction, PM10, and temperature measurements for the year 2022, while the corresponding output power data from 2021 is used on a daily basis. The study is based on the transfer forecasting approach in wind energy prediction. The aim is not to directly copy power values but to learn the meteorological variable production relationship and apply it to the following year's atmospheric data. This method is common in the energy sector, prevents the machine from overfitting, and generalizes the physical behavior of the local wind regime. The dataset collected during the spring and summer periods contains no missing values. During the winter season, atmospheric conditions are more irregular: factors such as condensation, freezing, low temperatures, high turbulence intensity, and sudden wind shear breaks increase the model's variance, making comparisons methodologically difficult. This study first aims to demonstrate the relative strength of hybrid models during periods of high seasonal stability. Of the entire dataset, 80% was used for training, 10% for validation, and the remaining 10% for testing.

The dataset collected during the spring and summer periods contains no missing values. Of the entire dataset, 80% was used for training, 10% for validation, and the remaining 10% for testing.

Table 3. Information on three different wind turbines in the wind farm

Wind Turbine	**E82-E2**	**E82-E3**	**E82-E5**
Nominal power (kW)	2000	3000	2350
Rotor diameter (m)	80	82	82
Navel height (m)	78	78	78
Wind length (m)	38.8	38.8	43.8

Table 4. Data set

Input	**Output**
Wind direction	Output power
PM10	
Temperature	
Historical output power	

In our study, the PM10 parameter is treated not merely as an additional meteorological input, but as a physical atmospheric variable that influences the aerodynamic behavior of wind flow. High particle concentration reduces momentum transfer on the rotor surface, decreasing the efficiency of the effective power curve and introducing systematic deviations in the wind speed–power relationship. When PM10 was included in the model, an improvement of 10–15% was observed in MAPE values. This result confirms the variable's contribution to prediction performance. A computer with an Intel Core i5-1135G7 CPU @ 2.40 GHz and

16 GB of RAM was used to implement the study with Matlab. Table 5 shows the computational costs of hybrid models.

Table 5. Computational costs of hybrid models

Model	Average education time	Explanation
ANN	3-4 min	Lower cost
VMD-ANN	6-7 min	VMD analysis
GRU-ANN	10-12 min	Time dependent account
JAYA-ANN	14-16 min	Global optimization 1000 iterations x50 populations

Although JAYA-ANN has the highest computational cost, it offers an improvement in prediction error in the range of 60–75%. Therefore, the method is technically rational.

Since wind power is a highly variable parameter, wind power forecasting is not an exact science. The error rate is calculated by comparing the predicted wind power at a certain time 't' with the actual power value in the data set. A low error indicates the accuracy of the prediction model. The evaluation criteria to be used in this study are root mean square error and mean absolute percentage error. The RMSE, MAPE, and MAE error evaluation formulas are provided in Equations 11, 12, and 13, respectively [33].

$$RMSE = \sqrt{\frac{1}{n}\sum_{i=1}^{n}\left(X_{est,i} - X_{tar,i}\right)^2} \quad (11)$$

$$MAPE = \frac{100}{n}\sum_{i=1}^{n}\left|\frac{X_{est,i} - X_{tar,i}}{X_{tar,i}}\right| \quad (12)$$

$$MAE = \frac{1}{n}\sum_{i=1}^{n}\left|X_{est,i} - X_{tar,i}\right| \quad (13)$$

Where:

- $X_{est,i}$= forecast value for time i
- $X_{tar,i}$ = actual value observed at time I
- i = number of forecast points

3.1. Forecast Results for the Summer Period

In the prediction using the ANN model, the MAPE values for the training, validation, and test subsets of the dataset were found to be 19.92%, 18.69%, and 17.81%, respectively. The corresponding RMSE values were calculated as 26.22 MW, 50.84 MW, and 66.78 MW, while the MAE values were 2.13 MW, 13.14 MW, and 15.97 MW, respectively. Figure 8 presents the prediction results for the training, validation, and test subsets of the dataset.

In the prediction using the VMD-ANN hybrid model, the MAPE values for the training, validation, and test subsets of the dataset were found to be 17.54%, 15.93%, and 14.02%, respectively. The corresponding RMSE values were calculated as 24.39 MW, 41.75 MW, and 38.06 MW, while the MAE values were 2.12 MW, 18.45 MW, and 10.98 MW, respectively. Figure 9 illustrates the prediction performance of the model across all subsets.

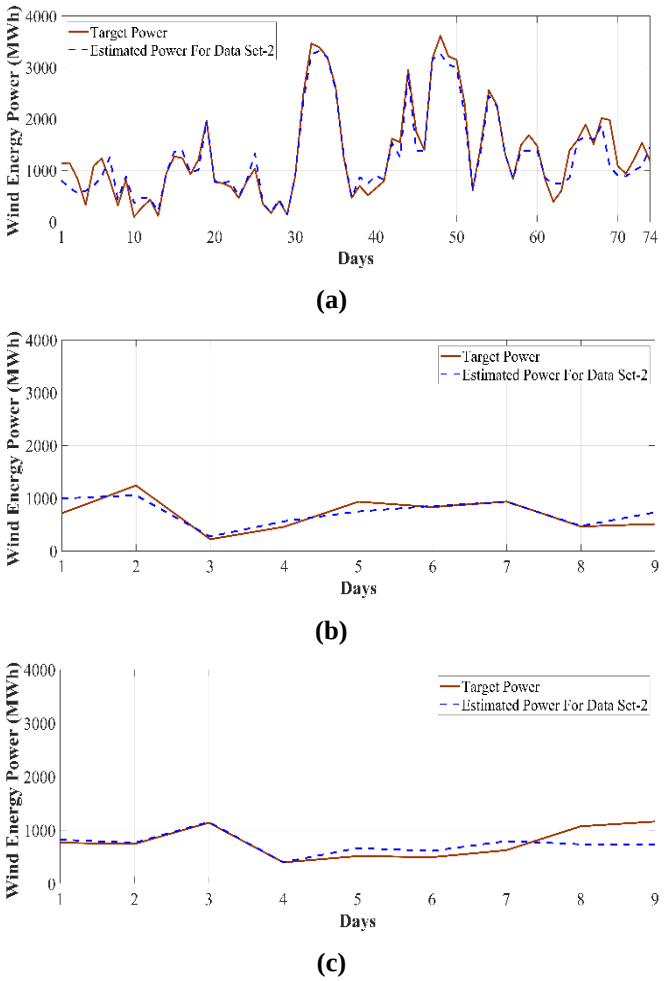

Fig. 8. Prediction results for the ANN model based on three subsets of the dataset: (a) training subset, (b) validation subset, and (c) testing subset.

The forecasting performance of the GRU-ANN hybrid model was evaluated based on the training, validation, and test subsets of the dataset. MAPE values were found to be 14.45% for the training set, 13.33% for the validation set, and 11.76% for the test set, indicating a consistent improvement in generalization capability. In parallel, RMSE values were computed as 23.10 MW, 35.73 MW, and 37.70 MW, while MAE values were 1.68 MW, 12.31 MW, and 10.21 MW, respectively. Figure 10 provides a graphical representation of the prediction performance across all subsets.

To assess the predictive capability of the JAYA-ANN hybrid model, performance metrics were examined for the training, validation, and test subsets of the dataset. MAPE was measured at 9.49% for the training data, 8.35% for the validation data, and 7.28% for the test data, reflecting the model's improved generalization on unseen data. Additionally, RMSE values were determined to be 14.56 MW, 31.75 MW, and 23.80 MW, while the corresponding MAE values were calculated as 0.99 MW, 7.55 MW, and 5.93 MW for the respective subsets. The model's prediction accuracy across all subsets is visually depicted in Figure 11. These results indicate that the proposed JAYA-ANN model demonstrates a reliable and robust performance in short-term wind power forecasting.

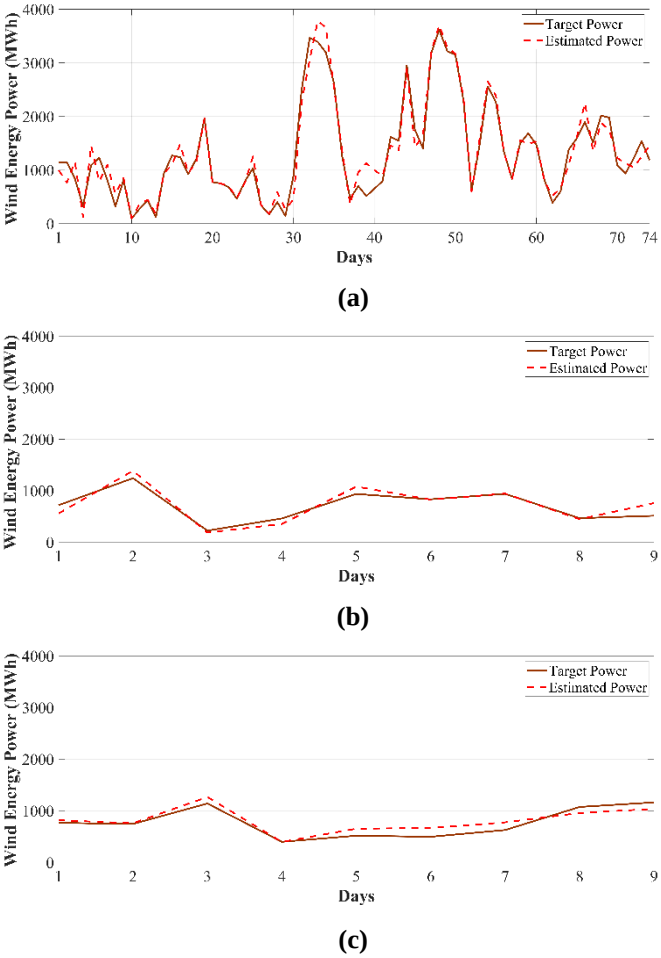

Fig. 9. Prediction results for the VMD-ANN model based on three subsets of the dataset: (a) training subset, (b) validation subset, and (c) testing subset.

The predictive performance of the ANN, VMD-ANN, GRU-ANN, and JAYA-ANN hybrid models was assessed through a comparative analysis of key evaluation metrics. Specifically, MAPE values were 19.59%, 17.04%, 14.08%, and 8.36%, respectively. In terms of RMSE, the models yielded values of 33.85 MW, 27.29 MW, 25.53 MW, and 17.14 MW. The corresponding MAE values were calculated as 4.91 MW, 4.16 MW, 3.15 MW, and 1.88 MW. These results clearly indicate that the JAYA-ANN model outperformed the others in terms of overall prediction accuracy. A visual comparison of the model performances is provided in Figure 12.

The proposed prediction models are generally not directly comparable to models in other studies, as each is based on different datasets with their own unique characteristics. The literature indicates that different datasets can affect a model's learning capacity and prediction accuracy; therefore, model performance should be evaluated relative to a standard reference model. To this end, the continuity model error is used to measure model performance more reliably. The continuity model error is based on the principle of making future predictions using values observed in the previous time step, thereby establishing a reference prediction standard. This error can be derived using Equations (6), (7), and (8). The predicted values are obtained by shifting the actual observed data by one time step and serve as a reference reflecting the model's baseline performance level.

Table 6 comprehensively and thoroughly presents the prediction performance of the four different modeling approaches considered in this study, namely the independent ANN, hybrid VMD-ANN, GRU-ANN, and JAYA-ANN models. The table enables a rigorous comparison in terms of prediction accuracy and overall effectiveness by evaluating the performance of each model on the same dataset. This clearly highlights the strengths and weaknesses of each model in the context of the dataset and provides important information to consider when selecting a model.

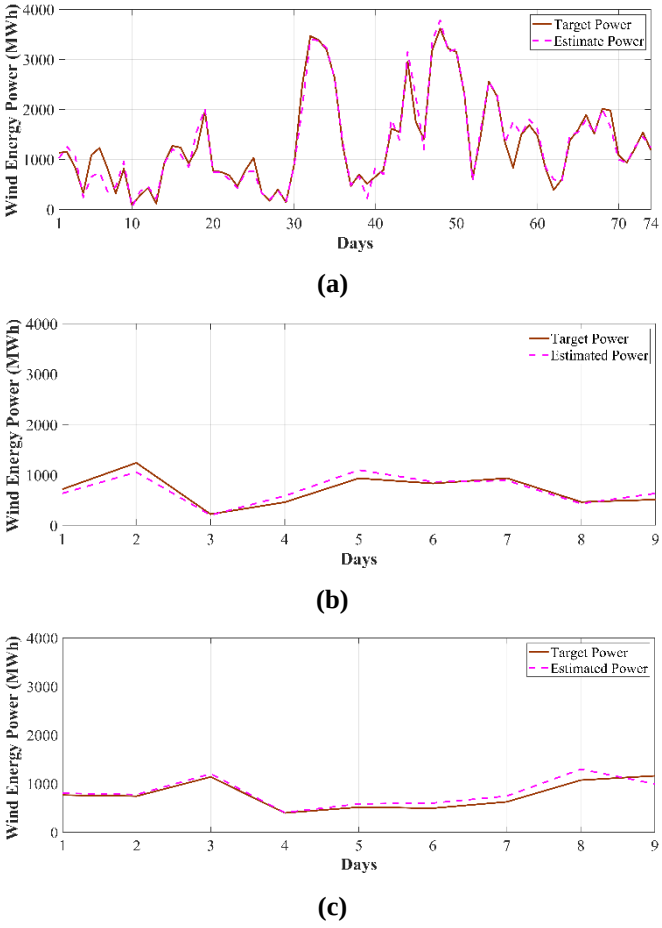

Fig. 10. Prediction results for the GRU-ANN model based on three subsets of the dataset: (a) training subset, (b) validation subset, and (c) testing subset.

3.2. Forecast Results for the Spring Semester

The ANN prediction model was evaluated using spring season data by comparing key performance metrics across different model configurations. MAPE values were recorded as 20.45%, 19.81%, and 16.53%, respectively; this demonstrates varying levels of relative prediction accuracy and highlights improvements achieved with more advanced modeling approaches. Regarding RMSE, the models produced values of 26.38 MW, 47.22 MW, and 40.2 MW. The corresponding MAE values were recorded as 1.71 MW, 11.9 MW, and 8.76 MW, further clarifying the average prediction errors and each model's effectiveness in capturing actual wind

power variations. Figure 13 graphically displays the comparative prediction performance of the models and allows for a clear visual assessment of the relative strengths and weaknesses of the models across the evaluation criteria.

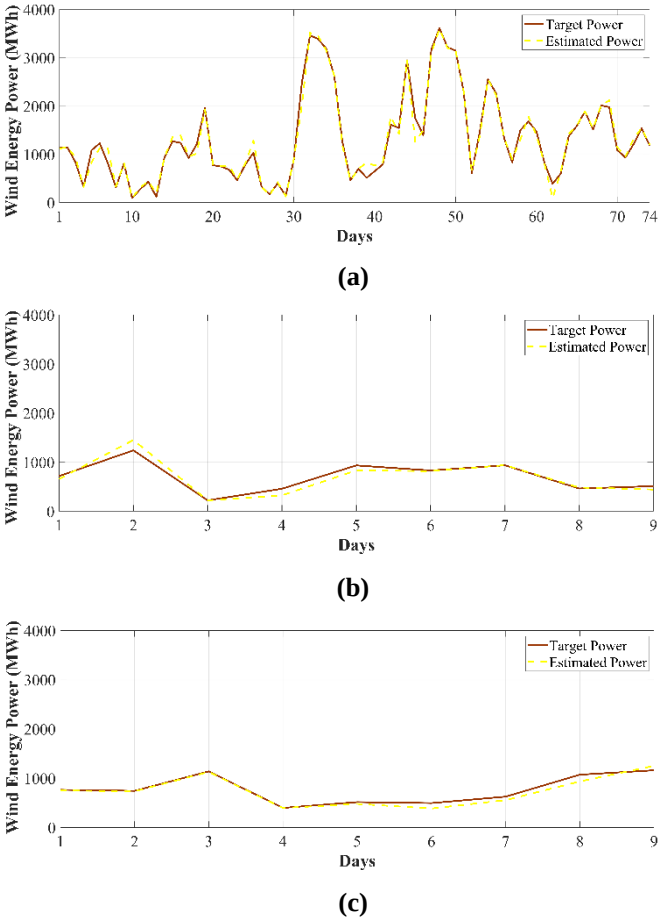

Fig. 11. Prediction results for the JAYA-ANN model based on three subsets of the dataset: (a) training subset, (b) validation subset, and (c) testing subset.

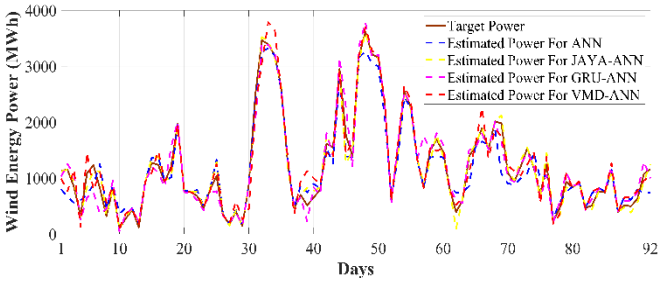

Fig. 12. Prediction results for ANN, VMD-ANN, GRU-ANN, and JAYA-ANN models.

The predictive performance of the VMD-ANN model was analyzed using data from the spring season through a comparative assessment of key evaluation metrics. MAPE values were observed to be 18.39%, 17.71%, and 17.02%, respectively. In terms of RMSE, the model yielded values of 15.54 MW, 27.74 MW, and 18.35 MW. The associated MAE values were calculated as 1.39 MW, 8.47 MW, and 4.71 MW. A visual comparison of these forecasting results is illustrated in Figure 14.

Table 6. MAPE, RMSE, and MEA values according to summer forecast results

Models	MAPE (%)	RMSE (MW)	MAE (MW)
ANN (training)	19.92	26.22	2.13
VMD-ANN (training)	17.54	24.39	2.12
GRU-ANN (training)	14.45	23.10	1.68
JAYA-ANN (training)	9.49	14.56	0.99
ANN (validation)	18.69	50.84	13.14
VMD-ANN (validation)	15.93	41.75	18.45
GRU-ANN (validation)	13.33	35.73	12.31
JAYA-ANN (validation)	8.35	31.75	7.55
ANN (test)	17.81	66.78	15.97
VMD-ANN (test)	14.02	38.06	10.98
GRU-ANN (test)	11.76	37.70	10.21
JAYA-ANN (test)	7.28	23.80	5.93
ANN (all)	19.59	33.85	4.91
VMD-ANN (all)	17.04	27.29	4.16
GRU-ANN (all)	14.08	25.53	3.15
JAYA-ANN (all)	8.36	17.14	1.88
PRM	33.25	66.99	11.96

The forecasting performance of the GRU-ANN model was thoroughly evaluated using several key performance metrics to assess its accuracy and reliability in predicting wind power outputs. The MAPE values were recorded as 15.81%, 14.26%, and 13.02%, respectively, indicating a notable improvement in relative prediction accuracy compared to baseline models and highlighting the model's ability to effectively capture the non-linear characteristics of the data. In terms of RMSE, the model yielded values of 14.27 MW, 29.4 MW, and 16.36 MW, reflecting the magnitude of absolute deviations from the observed measurements and providing insight into the overall predictive precision of the model. Meanwhile, the MAE was calculated as 1.25 MW, 8.18 MW, and 4.38 MW, further illustrating the average errors and demonstrating the model's capability to produce consistently reliable forecasts. A graphical comparison of these prediction outcomes is presented in Figure 15, offering a clear visual representation of the GRU-ANN model's performance across different evaluation criteria and enabling an intuitive assessment of its strengths relative to other forecasting approaches.

The forecasting performance of the JAYA-ANN model was comprehensively assessed using several key evaluation metrics to determine its accuracy and reliability in predicting wind power generation. The MAPE values were recorded as 12.76%, 12.45%, and 11.33%, respectively, demonstrating a consistently high relative prediction accuracy and indicating

the model's capability to effectively capture the non-linear and fluctuating nature of wind power data. The corresponding RMSE values were found to be 13.94 MW, 21.95 MW, and 19.93 MW, reflecting the magnitude of absolute deviations between the predicted and observed values and providing insight into the overall precision of the model. Furthermore, the MAE was determined to be 1.03 MW, 6.01 MW, and 4.12 MW, highlighting the average prediction errors and confirming the model's robustness in producing reliable forecasts across different time steps. Figure 16 presents a visual representation of these prediction outcomes, allowing for an intuitive comparison of the JAYA-ANN model's forecasting performance with other models and facilitating a clear understanding of its strengths and limitations in capturing the dynamics of wind power generation.

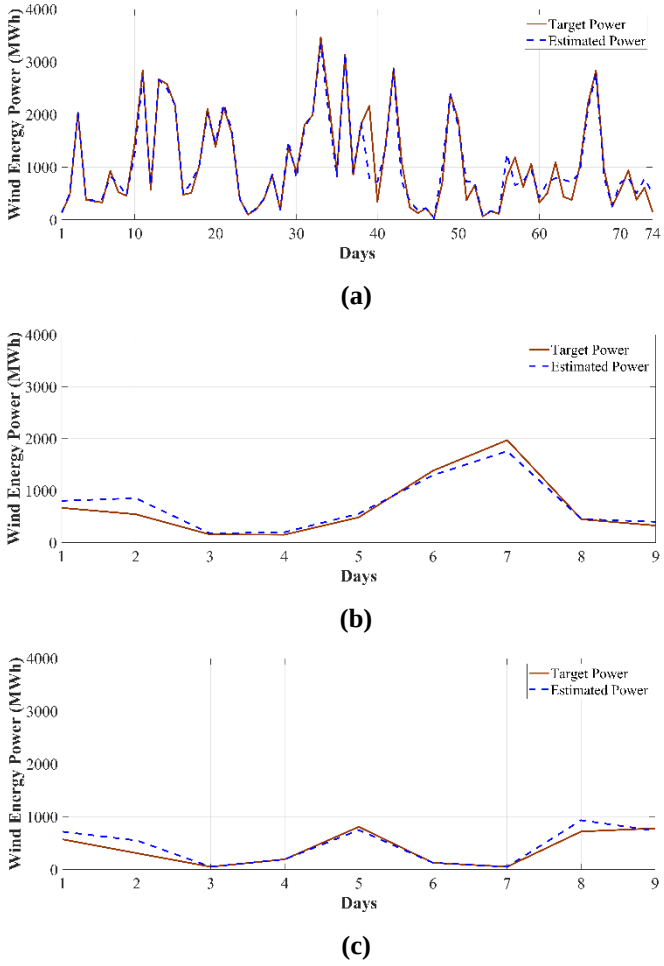

Fig. 13. Prediction results for the ANN model based on three subsets of the dataset: (a) training subset, (b) validation subset, and (c) testing subset.

A comparative analysis of fundamental performance metrics was conducted to comprehensively evaluate and compare the prediction capabilities of the ANN, VMD-ANN, GRU-ANN, and JAYA-ANN hybrid models.

The MAPE values of these models were recorded as 20%, 18.19%, 15.38%, and 12.59%, respectively. These values revealed a gradual improvement in relative prediction accuracy from the basic ANN model to the advanced JAYA-ANN model. The corresponding RMSE values were found to be 28.45 MW, 17.06 MW, 16.11 MW, and 15.10 MW; these values indicate the magnitude of absolute deviations from the observed values and provide a clear measure of each model's overall prediction accuracy. Additionally, the MAE was calculated as 3.34 MW for ANN, 2.20 MW for VMD-ANN, 2.08 MW for GRU-ANN, and 1.77 MW for JAYA-ANN, further illustrating the average prediction errors of the models and confirming the superior prediction consistency of hybrid approaches over the independent ANN model. Figure 17 provides a visual comparison of these model performances, enabling a clear and intuitive understanding of how each approach handles the variability and complexity of wind energy production and highlighting the advantages of hybridization and optimization in improving prediction accuracy. Table 7 provides a detailed evaluation of the prediction performance of four different modelling approaches, including an independent ANN model, along with Hybrid VMD-ANN, GRU-ANN, and JAYA-ANN models. The results presented are based on the dataset used in this study and enable a comprehensive comparison of each model in terms of performance metrics such as accuracy, precision, stability, and generalization ability.

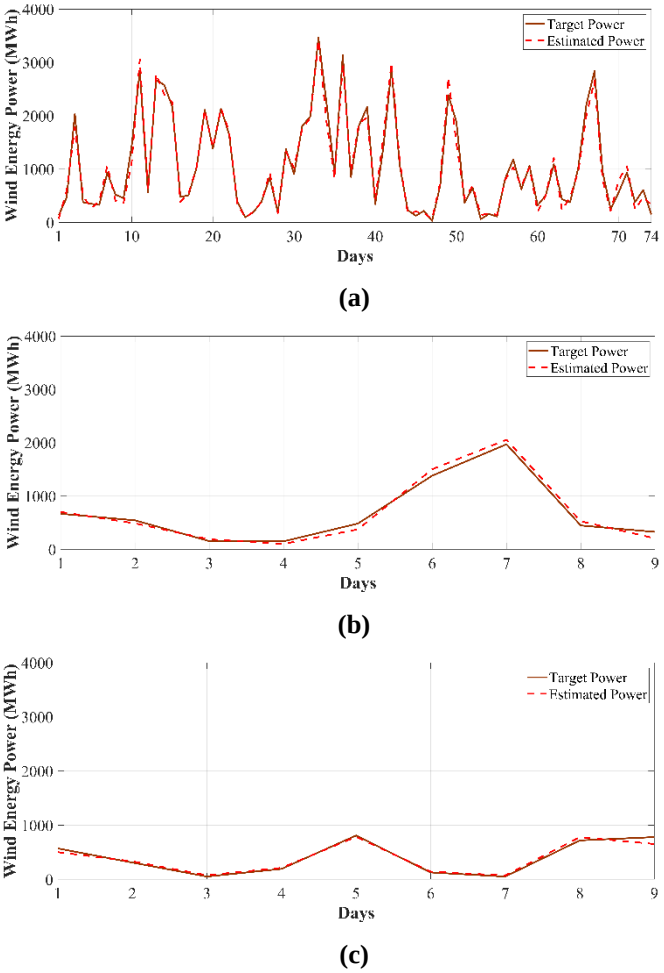

Fig. 14. Prediction results for the VMD-ANN model based on three subsets of the dataset: (a) training subset, (b) validation subset, and (c) testing subset.

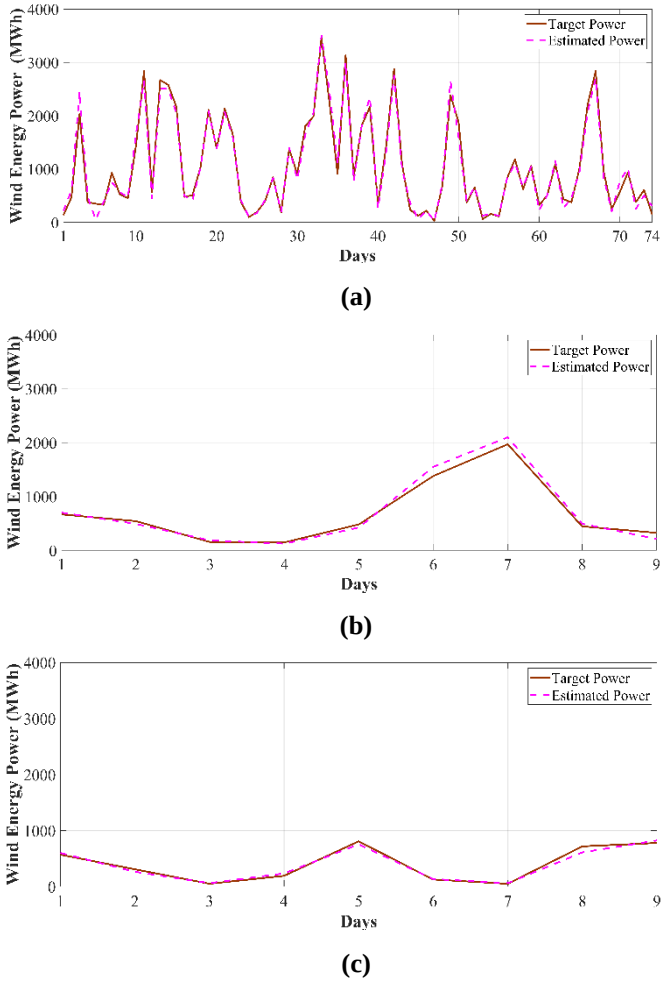

Fig. 15. Prediction results for the GRU-ANN model based on three subsets of the dataset: (a) training subset, (b) validation subset, and (c) testing subset.

The table also includes statistical indicators and error metrics that quantitatively reveal the predictive capacity of each model, allowing for a systematic evaluation of the advantages and limitations of different modelling approaches. In this context, Table 7 not only provides a detailed analysis of the prediction performance specific to the dataset, but also enhances the validity of the methods used in the study and serves as a reference for comparison and model selection in future research.

Table 8 summarizes the input variables, model structures, and performance metrics of different models used for wind energy forecasting in the current literature. The studies provide a comparative assessment using different datasets and forecasting approaches. As the proposed estimation model, the JAYA-ANN model was developed in this study using historical power data, wind direction, temperature, and PM10 parameters. The model's performance was evaluated seasonally, with MAPE found to be 8.36%, RMSE 17.14 MW, and MAE 1.88 MW for the summer season. For the spring period, MAPE was 12.59%, RMSE was 15.10 MW, and MAE was 1.77 MW. These results show that the JAYA-ANN model offers high prediction accuracy compared to other models in the literature, both in minimizing error rates and in adapting to seasonal differences.

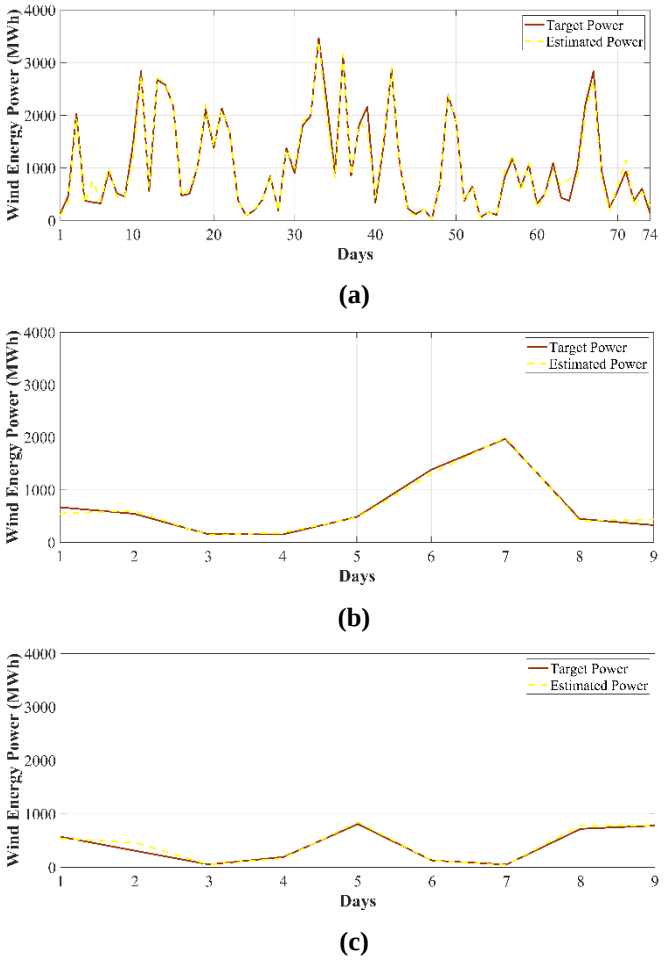

Fig. 16. Prediction results for the JAYA-ANN model based on three subsets of the dataset: (a) training subset, (b) validation subset, and (c) testing subset.

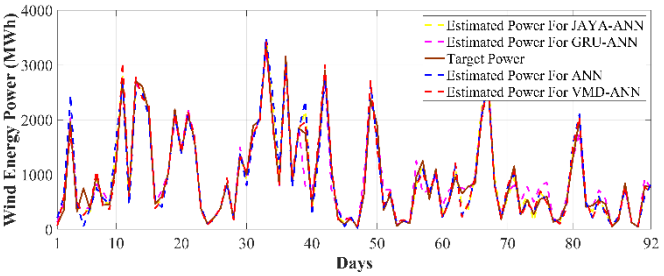

Fig. 17. Prediction results for ANN, VMD-ANN, GRU-ANN, and JAYA-ANN models.

In addition to the obtained performance results, the findings of this study highlight the effectiveness of integrating optimization algorithms with artificial neural network structures for improving wind power forecasting accuracy. The JAYA algorithm, which is based on a simple yet powerful population-based optimization mechanism, plays a significant role in optimizing the weight parameters of the ANN model and enhancing its learning capability. Unlike traditional training approaches that rely solely on gradient descent methods, the JAYA algorithm guides the optimization process by simultaneously approaching the best solution while avoiding the worst solution in the population.

Table 7. MAPE, RMSE, and MEA values according to spring season forecast results

Models	MAPE (%)	RMSE (MW)	MAE (MW)
ANN (training)	20.45	26.38	1.71
VMD-ANN (training)	18.39	15.54	1.39
GRU-ANN (training)	15.81	14.27	1.25
JAYA-ANN (training)	12.76	13.94	1.03
ANN (validation)	19.81	47.22	11.90
VMD-ANN (validation)	17.71	27.74	8.47
GRU-ANN (validation)	14.26	29.40	8.18
JAYA-ANN (validation)	12.45	21.95	6.01
ANN (test)	16.53	40.20	8.76
VMD-ANN (test)	17.02	18.35	4.71
GRU-ANN (test)	13.02	16.36	4.38
JAYA-ANN (test)	11.33	19.93	4.12
ANN (all)	20.00	28.45	3.34
VMD-ANN (all)	18.19	17.06	2.2
GRU-ANN (all)	15.38	16.11	2.08
JAYA-ANN (all)	12.59	15.10	1.77
PRM	41.96	46.65	5.96

This strategy enables the model to achieve improved convergence characteristics by effectively guiding the optimization process toward more optimal solutions while simultaneously reducing the likelihood of the training process becoming trapped in local optima, which is a common limitation encountered in traditional training procedures. As a result, the model is able to learn the underlying patterns of the data more efficiently and reach a more stable solution during the training phase. Furthermore, the incorporation of multiple meteorological parameters, including temperature, wind direction, and PM10 concentration, provides a more comprehensive and realistic representation of the environmental conditions influencing wind energy production, since wind power generation is inherently dependent on complex atmospheric dynamics and the nonlinear interactions among different meteorological variables. Since wind power generation is inherently influenced by atmospheric variability and complex nonlinear relationships among meteorological variables, the inclusion of these parameters enhances the model's ability to capture the dynamic behavior of wind power generation processes. Consequently, the outcomes of this study highlight the potential of hybrid artificial intelligence models as effective and powerful tools for renewable energy forecasting applications. Furthermore, future studies may enhance forecasting performance by incorporating additional meteorological variables, extending the dataset to cover longer time periods, and exploring advanced deep learning architectures combined with optimization algorithms to improve the robustness and generalization capability of wind power prediction models

Table 8. Comparison of predictions made in the literature with the proposed prediction model

Study	Inputs used	Model structure	Error measures
M. Ozturk et al. [34]	Historical power data, wind speed, temperature, relative humidity	ANN	MAPE= %6.46
O.Tasdemir et al [35]	Past power output, wind speed	PSO	RMSE= 44.09 MW
Y. Zhang et al. [36]	Wind Speed and direction	CNN-LSTM	MAE= 8.2 kW
A. Gijon et al. [37]	Wind speed, angle of inclination, rotor speed, torque, and power	ANN	MAPE= %10
A. J. R. Barrera [38]	Temperature, pressure, precipitation, wind	VMD-CNN-GRU	MAE=45.73, RMSE=59.37
Recommended forecast	Historical power data, wind direction, temperature, PM10	JAYA-ANN	Summer period MAPE= %8.36 MAE=1.88 MW RMSE=17.14 MW Spring period MAPE= %12.59 RMSE=15.10 MW MAE=1.77 MW

4. Conclusion

This study analyzes widely used forecasting models for wind power prediction as reported in the literature, with comparisons conducted across different time horizons. Based on an extensive literature review, forecasting methods, prediction intervals, input data types, and error metrics are examined in detail. To ensure a balanced day-ahead supply-demand relationship in wind power systems and to enhance overall system stability, commonly used error evaluation metrics, namely MAPE, RMSE, and MAE, are employed in the evaluation of daily wind power forecasting accuracy.

On the other hand, in this study, the effect of the PM10 parameter on wind power generation is particularly emphasized due to the increasing importance of the impact of air pollution on power generation systems. Analysing the impact of PM10 levels on wind power generation is critical for developing more accurate and reliable forecasting models. Improved forecasting results obtained by including the PM10 parameter enable wind energy power plants to make more accurate and reliable forecasts.

In this study, a hybrid model is developed by combining the JAYA - ANN for wind power forecasting. This hybrid model is compared with GRU and VMD based hybrid ANN models commonly used in the literature. As a result of the comparisons, it was determined that the JAYA-ANN model was superior to the other models in terms of prediction accuracy.

The following inferences were obtained from the estimation results made in the summer period using the data set:

- As a result of the prediction using the ANN, the MAPE, RMSE, and MAE values were obtained as 19.59%, 33.85 MW, and 4.91 MW, respectively. The ANN-based prediction yielded improvements of 41.08%, 49.47%, and 58.97% in MAPE, RMSE, and MAE, respectively, compared to the persistence reference model.

- The hybrid VMD-ANN model achieved MAPE, RMSE, and MAE values of 17.04%, 27.29 MW, and 4.16 MW, in order. Compared to the persistence reference model, the VMD-ANN approach resulted in performance improvements of 48.75% in MAPE, 59.26% in RMSE, and 65.21% in MAE.

- Utilizing the GRU-ANN hybrid model for wind power forecasting resulted in MAPE, RMSE, and MAE values of 14.08%, 25.53 MW, and 3.15 MW, in turn. Compared to the persistence reference model, this hybrid approach led to improvements of 57.65% in MAPE, 61.89% in RMSE, and 73.66% in MAE.

- The JAYA-ANN hybrid model achieved MAPE, RMSE, and MAE values of 8.36%, 17.14 MW, and 1.88 MW, respectively, for wind power forecasting. Compared to the persistence benchmark model, this hybrid approach demonstrated improvements of 74.85% in MAPE, 74.41% in RMSE, and 84.28% in MAE.

The following inferences were obtained from the estimation results made in the spring period using the data set:

- The ANN-based prediction yielded MAPE, RMSE, and MAE values of 20%, 28.45 MW, and 3.34 MW, respectively. Compared to the persistence model, this approach achieved improvements of 52.33%, 39.02%, and 43.96% in MAPE, RMSE, and MAE, respectively.

- The VMD-ANN hybrid model achieved values of 18.19% for MAPE, 17.06 MW for RMSE, and 2.2 MW for MAE. Compared to the persistence model, these results indicate improvements of 56.64%, 63.42%, and 63.08%, respectively.

- The GRU-ANN hybrid model yielded MAPE, RMSE, and MAE values of 15.38%, 16.11 MW, and 2.08 MW, respectively, for wind power forecasting. Relative to the persistence model, it demonstrated improvements of 63.34%, 65.46%, and 65.1% in MAPE, RMSE, and MAE, respectively.

- JAYA-ANN hybrid model yielded MAPE, RMSE, and MAE values of 12.59%, 15.1 MW, and 1.77 MW, respectively. Compared to the persistence benchmark model, this approach achieved improvements of 70% in MAPE, 67.63% in RMSE, and 70.3% in MAE.

As can be clearly seen from the conclusions summarized above, the superior performance of the JAYA-ANN hybrid model over the ANN, VMD-ANN, and GRU-ANN forecasting models in both summer and spring shows that hybrid models can be used effectively in wind power forecasting. Although building and optimizing these models is often a complex process, the results obtained prove that the effort is worthwhile.

In wind power forecasting studies, the provision of data sets constitutes a significant challenge. Therefore, anonymizing the data sets used will facilitate the comparison of similar studies and the sharing of data sets. The absence of any data deficiency in the data set used contributed to the more accurate prediction results.

Future studies may examine the effect of other air pollution parameters and the changes of particulate matter parameters in wind power forecasting. In addition, due to the limited long-term forecasting studies, the long-term performance of hybrid models can also be investigated. The performance of other hybrid models in long-term forecasting can also be analysed. The findings obtained in this study provide valuable information that can be used in the calculation of installation costs and return on investment periods of new wind power plants.

Considering the superior prediction performance of the JAYA-ANN hybrid model, it is recommended that this model be used in new projects and in the improvement of existing systems.

Acknowledgements

The authors declare that no specific funding or institutional support was received for this study.

Author Contributions

Bahtiyar Taşdemir is responsible for conceptualizing the study, validation, data editing, software development, resource provision, and project management. Bahtiyar Taşdemir and Mustafa Yaz jointly contributed to the development of the methodology, formal analysis, research process, preparation of the first draft of the article, review and editing, visualization, and consulting processes. All authors have read and approved the final version of the article.

Conflict of Interest

The author(s) declared no potential conflicts of interest with respect to the research, authorship, and/or publication of this article.

References

[1] A. Gulraiz, S. S. H. Zaidi, M. Ashraf, M. Ali, A. Lashab, J. M. Guerrero, B. Khan, ‘‘Impact of photovoltaic ingress on the performance and stability of low voltage Grid-Connected Microgrids,’’ Results in Engineering, Volume 26, 2025, 105030, ISSN 2590-1230, https://doi.org/10.1016/j.rineng.2025.105030.

[2] Global Wind Report 2024, Accessed: Jan. 14, 2025. [Online]. Available: https://gwec.net/global-wind-report-2024.

[3] S. Hu, Y. Xiang, H. Zhang, S. Xie, J. Li, C. Gu, W. Sun and J. Liu, “Hybrid forecasting method for wind power integrating spatial correlation and corrected numerical weather prediction,” Appl. Energy, vol. 293, p. 116951, Jul. 2021, doi: 10.1016/j.apenergy.2021.116951.

[4] L. Ye, B. Dai, Z. Li, M. Pei, Y. Zhao, and P. Lu, “An ensemble method for short-term wind power prediction considering error correction strategy,” Appl. Energy, vol. 322, p. 119475, Sep. 2022, doi: 10.1016/j.apenergy.2022.119475.

[5] J. Liu, Z. Zhao, J. Ji, and M. Hu, “Research and application of wireless sensor network technology in power transmission and distribution system,” Intelligent and Converged Networks, vol. 1, no. 2, pp. 199–220, Sep. 2020, doi: 10.23919/ICN.2020.0016.

[6] Z. Ma and G. Mei, “A hybrid attention-based deep learning approach for wind power prediction,” Appl. Energy, vol. 323, p. 119608, Oct. 2022, doi: 10.1016/j.apenergy.2022.119608.

[7] X. Zhao, S. Wang, and T. Li, “Review of evaluation criteria and main methods of wind power forecasting,” Energy Procedia, vol. 12, pp. 761–769, 2011, doi: 10.1016/j.egypro.2011.10.102.

[8] S. Hanifi, X. Liu, Z. Lin, and S. Lotfian, “A critical review of wind power forecasting methods—Past, present and future,” Energies (Basel), vol. 13, no. 15, p. 3764, Jul. 2020, doi: 10.3390/en13153764.

[9] Y. Wang, R. Zou, F. Liu, L. Zhang, and Q. Liu, “A review of wind speed and wind power forecasting with deep neural networks,” Appl. Energy, vol. 304, p. 117766, Dec. 2021, doi: 10.1016/j.apenergy.2021.117766.

[10] O. Karakoç and İ. Buğdaycı, “Spatial modeling of chlorophyll-a parameter by Landsat-8 satellite data and deep learning techniques: The case of Lake Mogan”, NOHU J. Eng. Sci., vol. 14, no. 2, pp. 615–629, 2025, doi: 10.28948/ngumuh.1603421.

[11] S. M. Malakouti, “Estimating the output power and wind speed with ML methods: A case study in Texas,” Case Studies in Chemical and Environmental Engineering, vol. 7, p. 100324, Jun. 2023, doi: 10.1016/j.cscee.2023.100324.

[12] X. Gao, W. Guo, C. Mei, J. Sha, Y. Guo and H. Sun, “Short-term wind power forecasting based on SSA-VMD-LSTM,” Energy Reports, vol. 9, pp. 335–344, Oct. 2023, doi: 10.1016/j.egyr.2023.05.181.

[13] B. Xiong, L. Lou, X. Meng, X. Wang, H. Ma and Z. Wang, “Short-term wind power forecasting based on Attention Mechanism and Deep Learning,” Electric Power Systems Research, vol. 206, p. 107776, May 2022, doi: 10.1016/j.epsr.2022.107776.

[14] H. Alkabbani, F. Hourfar, A. Ahmadian, Q. Zhu, A. Almansoori and A. Elkamel, “Machine learning-based time series modelling for large-scale regional wind power forecasting: A case study in Ontario, Canada,” Cleaner Energy Systems, vol. 5, p. 100068, Aug. 2023, doi: 10.1016/j.cles.2023.100068.

[15] J. Zhu, L. Su, and Y. Li, “Wind power forecasting based on new hybrid model with TCN residual modification,” Energy and AI, vol. 10, p. 100199, Nov. 2022, doi: 10.1016/j.egyai.2022.100199.

[16] B. He, L. Ye, M. Pei, P. Lu, B. Dai, Z. Li and K. Wang, “A combined model for short-term wind power forecasting based on the analysis of numerical weather prediction data,” Energy Reports, vol. 8, pp. 929–939, Nov. 2022, doi: 10.1016/j.egyr.2021.10.102.

[17] V. Chandran, C. K. Patil, A. M. Manoharan, A. Ghosh, M. G. Sumithra, A. Karthick, R. Rahim and K. Arun, “Wind power forecasting based on time series model using deep machine learning algorithms,” Mater. Today Proc., vol. 47, pp. 115–126, 2021, doi: 10.1016/j.matpr.2021.03.728.

[18] V. Singh, “Application of artificial neural networks for predicting generated wind power,” International Journal of Advanced Computer Science and Applications, vol. 7, no. 3, 2016, doi: 10.14569/IJACSA.2016.070336.

[19] A. Sharkawy, “Principle of neural network and its main types: Review,” Journal of Advances in Applied & Computational Mathematics, vol. 7, pp. 8–19, Aug.

2020, doi: 10.15377/2409-5761.2020.07.2.

[20] A. D. Rasamoelina, F. Adjailia, and P. Sincak, "A review of activation function for artificial neural network," in Proc. 2020 IEEE 18th World Symposium on Applied Machine Intelligence and Informatics (SAMI), Jan. 2020, pp. 281–286, doi: 10.1109/SAMI48414.2020.9108717.

[21] R. Rojas, Neural Networks: A Systematic Introduction. Berlin, 1996.

[22] T. Saraç, "Estimating software project duration using artificial neural networks," Türkiye, 2005.

[23] R. Venkata Rao, "Jaya: A simple and new optimization algorithm for solving constrained and unconstrained optimization problems," International Journal of Industrial Engineering Computations, pp. 19–34, 2016, doi: 10.5267/j.ijiec.2015.8.004.

[24] Z. He and F. Tong, "Residual RNN models with pruning for digital predistortion of RF power amplifiers," IEEE Trans. Veh. Technol., vol. 71, no. 9, pp. 9735, 2022.

[25] J. Chung, C. Gulcehre, K. Cho, and Y. Bengio, "Empirical evaluation of gated recurrent neural networks on sequence modeling," arXiv preprint, arXiv:1412.3555, 2014.

[26] A. Sherstinsky, "Fundamentals of recurrent neural network (RNN) and long short-term memory (LSTM) network," Physica D: Nonlinear Phenomena, vol. 404, p. 132306, 2020, doi: 10.1016/j.physd.2019.132306.

[27] X. Wang, G. Xie, W. Liu and Yang Gao, "A long-term vertical displacement prediction method of concrete bridges based on meteorological shared data and optimized GRU model," Measurement, vol. 253, Part D, p. 117811, 2025, doi: 10.1016/j.measurement.2025.117811.

[28] K. Dragomiretskiy and D. Zosso, "Variational mode decomposition," IEEE Trans. Signal Process., vol. 62, pp. 531–544, 2014.

[29] M. Fang, F. Zhang, Y. Yang, R. Tao, R. Xiao and D. Zhu, "The influence of optimization algorithm on the signal prediction accuracy of VMD-LSTM for the pumped storage hydropower unit," J. Energy Storage Mater., vol. 78, p. 110187, 2024.

[30] H. Li, S. Li, J. Sun, B. Huang, J. Zhang and M. Gao, "Ultrasound signal processing based on joint GWO-VMD wavelet threshold functions," Measurement, vol. 226, p. 114143, 2024.

[31] X. Yan and M. Jia, "Application of CSA-VMD and optimal scale morphological slice bispectrum in enhancing outer race fault detection of rolling element bearings," Mech. Syst. Signal Process., vol. 122, pp. 56–86, 2019.

[32] R. Perez, S. Kivalov, J. Schlemmer, K. Hemker, D. Renne and T. Hoff, "Validation of short and medium term operational solar radiation forecasts in the US," Solar Energy, vol. 84, pp. 2161–2172, 2010. https://doi.org/10.1016/j.solener.2010.08.014.

[33] O.Taşdemir, "Photovoltaic Power Prediction with Teaching Learning Based Optimization Algorithm," Gazi University Journal of Science Part A: Engineering and Innovation, 11(4), 780-791, 2024. https://doi.org/10.54287/gujsa.1581828.

[34] M. Öztürk, R. Kayabaşı and O. Taşdemir, "Kirşehir'in rüzgar enerjisi potansiyeli ve iç anadolu bölgesi kurulu rüzgar enerjisi santrallerinin güç analizi," Kahramanmaraş Sütçü İmam Üniversitesi Mühendislik Bilimleri Dergisi, 28(1), 189-201. https://doi.org/10.17780/ksujes.1533576.

[35] O. Taşdemir, İ. F. Tepe ve E. Irmak, "PSO algoritması ile mevsimsel rüzgar enerjisi tahminlerinin optimizasyonu, " 2024 6. Küresel Güç, Enerji ve İletişim Konferansı (GPECOM) , Budapeşte, Macaristan, 2024, ss. 543-548, doi: 10.1109/GPECOM61896.2024.10582566.

[36] Y. Zhang, H. Su, R. Wang, J. Deng, Y. Wang, W. Guo and R. Li, "Short-term forecast method of wind power output based on multi-scale CNN-LSTM in extreme weather, " International Journal of Electrical Power & Energy Systems, Volume 172, 2025, 111191, ISSN 0142-0615, https://doi.org/10.1016/j.ijepes.2025.111191.

[37] A. Gijón, A. P. Goitia, E. Perea, M. M. Solana and J. G. Romero, "Prediction of wind turbines power with physics-informed neural networks and evidential uncertainty quantification, " Engineering Applications of Artificial Intelligence, Volume 164, Part B, 2026, 113331, ISSN 0952-1976, https://doi.org/10.1016/j.engappai.2025.113331.

[38] A. J. R. Barrera, A. E. Sipols, A. P. Garcia and M. A. L. Carmona, "Short-term wind power forecasting integrating wake effect modeling with variational mode decomposition enhanced deep learning architectures, " Energy Conversion and Management, Volume 348, Part C, 2026, 120738, ISSN 0196-8904, https://doi.org/10.1016/j.enconman.2025.120738.

International Journal of Smart Grid (IJSmartGrid)
https://www.ijsmartgrid.org/ Online ISSN: 2602-439X
L.V. Dai and H.H.B. Nghia, Vol. 10, No. 1, March, 2026 Research Article

Advanced Control Technique for Optimizing Stability and Fault Recovery in Grid-Connected Solar Systems

Le Van Dai*‡, Huynh Hoang Bao Nghia*

*Electric Power System Research Group, Industrial University of Ho Chi Minh City, Ho Chi Minh City, Vietnam

(levandai@iuh.edu.vn, nghiabaohoanghuynh123@gmail.com)

‡Corresponding Author: Le Van Dai, Electric Power System Research Group, Industrial University of Ho Chi Minh City, Ho Chi Minh City, Vietnam.

Tel: +84 90167 2689, levandai@iuh.edu.vn

Received: 05.07.2025 Accepted:08.02.2026

Abstract- The primary purpose of this study is to enhance the operational stability and fault recovery capabilities of grid-connected photovoltaic (PV) systems, which frequently encounter challenges related to environmental variability and severe grid faults. To address these issues, the paper proposes an advanced maximum power point tracking (MPPT) controller utilizing an artificial neural network (ANN) trained with the Levenberg-Marquardt (LM) algorithm. The research procedure involves modelling a detailed grid-connected system comprising a DC-DC boost converter and a three-level neutral-point-clamped (NPC) inverter within the MATLAB/Simulink environment. The proposed control strategy is rigorously evaluated and compared with a conventional perturb-and-observe (P&O) method with dynamic step-size tuning under two distinct scenarios: normal operation with varying irradiance and severe three-phase-to-ground (LLLG) fault conditions. The main results demonstrate the superior performance of the proposed ANN-LM technique. Under normal conditions, the proposed method provides greater stability, with a total percentage overshoot of only 1.292%, which is significantly lower than the 1.496% observed with the conventional method. In the event of an LLLG fault, the proposed controller exhibits exceptional resilience, achieving a rapid voltage recovery time of 0.539 seconds compared to 0.713 seconds for the benchmark. Furthermore, the proposed technique improves power quality by limiting the inverter voltage total harmonic distortion (THD) to 122.37% during faults, whereas the conventional method reaches 147.31%. These findings confirm that the ANN-LM controller effectively optimizes energy extraction and ensures robust system operation in the face of grid disturbances.

Keywords: Grid-connected photovoltaic system, maximum power point tracking (MPPT), artificial neural network (ANN), Levenberg-Marquardt algorithm, fault recovery.

1. Introduction

In recent years, the field of power systems and renewable energy has made significant strides, focusing on advanced optimization and control techniques to reduce operating costs, mitigate emissions, and enhance grid reliability. A prominent research trend involves shifting towards multi-objective algorithms and intelligent control methods to address the increasing uncertainty of distributed resources. Renewable energy, particularly solar power, is

Cite this article as: L.V. Dai and H.H.B. Nghia, "Advanced Control Technique for Optimizing Stability and Fault Recovery in Grid-Connected Solar Systems" *International Journal of Smart Grid (ijSmartGrid)*, Vol. 10, No. 1, pp. 30–47, March, 2026.

increasingly pivotal in replacing fossil fuels due to its environmental benefits and abundant availability [1, 2]. In the context of the world facing increasingly serious challenges related to carbon emissions and climate change, the transition from fossil fuels to renewable energy sources, especially solar energy and photovoltaic (PV) systems, is an inevitable path. Studies show that integrating PV systems into energy and industrial systems has the potential to replace a significant portion of traditional electricity, thereby contributing to indirect CO_2 emission reductions at the system level through reduced fossil fuel demand [3]. Furthermore, energy and exergy analyses have demonstrated that harnessing PV energy in integrated structures not only improves overall energy efficiency but also significantly improves the environmental sustainability of modern energy systems [4, 5]. Furthermore, studies based on energy-exergy analysis and system structure optimization show that prioritizing clean, renewable energy sources, including solar energy, can significantly reduce the carbon emission intensity per unit of useful energy, thereby confirming the important role of PV systems in long-term carbon emission reduction strategies [6, 7].

Among renewable energy sources, PV systems are widely deployed globally, in both grid-connected and standalone configurations, serving diverse applications in energy production and the industrial sector [8, 9]. However, the energy conversion efficiency of PV systems is heavily influenced by environmental conditions such as shading, dust accumulation, temperature, and radiation intensity, which directly affect the determination of the maximum power point (MPP) [10]. Consequently, tracking and maintaining the MPP, also known as maximum power point tracking (MPPT), is a critical factor for optimal energy extraction. Although traditional algorithms, such as perturb and observe (P&O) and incremental conductance, are simple and easy to implement, they often struggle under rapidly changing weather conditions, leading to large oscillations and relatively low tracking accuracy [11].

Grid-connected PV systems typically comprise PV panels, DC-DC converters, DC-AC inverters, MPPT controllers, and grid synchronization controllers [12]. Beyond efficiency, stability is a paramount concern. When grid faults occur, such as voltage sags or severe three-phase-to-ground (LLLG) short circuits, the grid voltage can drop sharply within a short period, causing instability in the PV system and potentially forcing the inverter to disconnect [13, 14]. While the design of renewable energy systems has advanced, ensuring stability, robust control, and high fault ride-through performance remains a major challenge due to the complex nonlinear characteristics of these systems [11].

Enhancing the stability and reliability of power systems through intelligent optimization and control is a rapidly expanding research area. PV systems are generally categorized into two main types: grid-connected systems and standalone systems [15, 16]. To maximize performance, various optimization techniques have been investigated across different aspects of the smart grid [17]. For instance, in microgrid operation, the NSGA-II algorithm has proven effective in reducing costs and pollution by accounting for forecast errors in renewable sources [18]. Similarly, metaheuristic algorithms, such as genetic algorithms (GA) and particle swarm optimization (PSO), play a crucial role in optimizing energy storage systems for load flattening [19]. In the domain of protection and reliability, fuzzy logic methods have been applied to rapidly detect transformer failures. Improved bee algorithms have optimized the design of solar-wind hybrid systems to satisfy reliability constraints [20].

Furthermore, the artificial bee colony algorithm has demonstrated significant results in reducing losses in distribution grids, and Monte Carlo simulation, combined with multi-objective algorithms, has been utilized to address unit commitment problems under uncertainty. Regarding dynamic stability, optimal coordination between flexible AC transmission system devices and power system stabilizers has demonstrated superior oscillation-damping capabilities [21]. Additionally, studies on the aging process of insulation materials under contamination provide critical insights into component durability in outdoor environments [22]. These studies collectively aim to develop optimal control strategies that adapt to strong fluctuations in load and renewable sources while ensuring cost-effectiveness, stability, and reliability. This forms the basis for discussing the main objective of this paper.

Specific improvements to MPPT algorithms have also been extensively explored. In study [23], an enhancement to the traditional P&O algorithm was proposed by incorporating current change information to address the “drift” phenomenon caused by sudden irradiance changes. Similarly, a study [24] modified the incremental conductance algorithm to mitigate incorrect responses under rapidly changing conditions, increasing tracking speed by approximately 20-30%. To address partial shading, study [24] proposed a hybrid of the simulated annealing algorithm and P&O, effectively preventing the system from being trapped in local maxima. Furthermore, the slime mold golden sine algorithm was presented in [25] to offer superior convergence speed compared to PSO and other heuristic methods. Another strategy involving variable-step-size P&O using GA was discussed in [21], which adjusts the step size based on proximity to the MPP to balance speed and oscillation.

Despite these advancements, traditional and heuristic methods can still struggle with the nonlinear complexities of PV systems under severe disturbances. Consequently, machine learning techniques, particularly artificial neural networks (ANNs) [26], have emerged as powerful tools for MPPT. ANNs can model the nonlinear relationship between inputs, such as voltage, current, temperature, and output power, without requiring prior mathematical assumptions. In this study, an ANN-based MPPT controller is designed using a dataset of historical voltage and current values to estimate the optimal duty cycle for the DC-DC converter. Unlike standard training algorithms, this study employs the Levenberg-Marquardt (LM) algorithm, an efficient quasi-Newton optimization technique, to train the network, enabling rapid convergence with minimal error.

The ANN trained with the LM algorithm not only improves power prediction accuracy but also ensures high stability and adaptability under rapidly changing weather

conditions. The primary objective of this research is to design an intelligent MPPT controller that quickly locates the GMPP while minimizing power fluctuations. The proposed method is validated through simulations involving irradiance changes and, crucially, under an LLLG fault scenario, utilizing fault analysis methodologies consistent with previous research [27]. The results demonstrate that the proposed controller significantly reduces harmonic distortion, enhances the quality of the DC bus voltage, and ensures rapid system recovery.

This study contributes to control theory by demonstrating an advanced control framework that enhances the stability and fault tolerance of photovoltaic systems under grid failures. The research provides system-level insights into the dynamic interaction between photovoltaic systems and the grid during faults, supporting the reliable integration of large-scale photovoltaic systems in compliance with grid regulations. In summary, the main contributions of this research are presented as follows:

- This paper introduces a novel approach for the MPPT controller utilizing an ANN trained with the LM algorithm. This method enables precise system identification and dynamic control of parameters, optimizing energy extraction from PV panels under varying irradiation and temperature conditions.

- The system is simulated under an LLLG fault scenario, demonstrating that the proposed controller exhibits high resilience. The system recovers quickly and resumes stable operation after the fault, showcasing the robustness and adaptability of the controller under real-world conditions.

- The proposed method significantly reduces harmonic distortion and enhances the quality of the DC bus voltage. This improvement minimizes performance losses caused by harmonic interference and optimizes the DC-AC energy conversion process.

The primary objective of this study is to develop and validate an intelligent MPPT strategy for grid-connected PV systems, ensuring rapid global MPPT, high operational stability, and robust fault tolerance under severe grid disturbances. Specifically, this study aims to design an MPPT controller based on an ANN trained with the LM algorithm to accurately estimate the optimal duty cycle of a DC-DC converter under rapidly changing radiation and temperature conditions. In addition to improving steady-state power extraction capabilities, the proposed controller is evaluated under severe LLLG conditions to assess its robustness, dynamic recovery performance, and impact on DC bus voltage quality and harmonic distortion. Through comprehensive simulation analysis, this study seeks to demonstrate that the proposed ANN-LM-based MPPT method offers superior performance compared to conventional MPPT techniques in terms of tracking accuracy, system stability, and grid fault tolerance.

One of the main advantages of this study lies in the integration of an ANN-based MPPT controller with the LM training algorithm, enabling rapid convergence and high prediction accuracy without the need for a specific mathematical model of the PV system. This data-driven approach effectively captures the nonlinear behavior of PV characteristics under varying environmental conditions. Another key strength is the comprehensive evaluation of system performance under both normal operating conditions and severe grid disturbances. By considering the LLLG fault scenario, this study goes beyond conventional MPPT performance evaluation and demonstrates the robustness and fault tolerance of the proposed controller. Furthermore, the reduction of harmonic distortion and improvement of DC bus voltage quality highlight the practical benefits of the proposed method in enhancing overall energy conversion efficiency and grid compatibility. Despite these advantages, the proposed method still has some limitations. The performance of ANN-based MPPT controllers is highly dependent on the quality and representativeness of the training dataset. Insufficient or skewed training data can reduce tracking accuracy under unknown operating conditions. Furthermore, the computational complexity of training ANNs using LM algorithms can make real-time deployment on inexpensive embedded platforms challenging, especially in large-scale optoelectronic systems. Moreover, this research is primarily validated through simulation. While the results show promising performance, experimental validation on a hardware test system is necessary to fully assess real-world implementation issues such as sensor noise, parameter uncertainty, and communication latency. These aspects will be addressed in subsequent studies.

Following this introduction, the paper is organized into several sections. Section 2 details the grid-connected solar energy conversion system. Section 3 discusses the proposed control solutions. Section 4 presents the simulation results under both normal and fault conditions. Finally, the conclusion summarizes the research's key findings.

2. Grid-Connected PV Solar Energy Conversion System

Fig. 1 shows the configuration of the grid-connected PV control system. The PV array is rated at 219.961 W under standard test conditions, 1000 W/m^2 irradiance, and 25°C cell temperature. It is interfaced with a dedicated DC-DC boost converter. The converter is controlled by an ANN-based MPPT algorithm to regulate the PV terminal voltage and ensure maximum power extraction. The boost converter output is connected to a common DC-link with a nominal voltage of 1000 V.

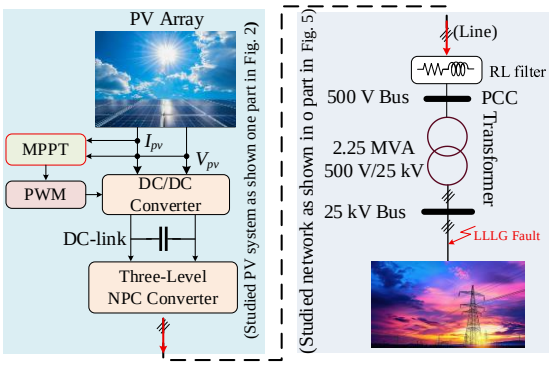

Fig. 1. Grid-connected solar power system.

The energy is then converted to three-phase AC via a three-level neutral point clamped (NPC) inverter, producing an AC voltage of approximately 500 V. A DC voltage link controller controls the inverter to maintain a DC voltage of 1000 V despite variations in input power from the PV arrays. Additionally, the system is equipped with a reactive power controller, allowing the inverter to either generate or absorb reactive power up to ±1 MVAr. To connect to the grid, the system uses a three-phase transformer with a power rating of 2.25 MVA and a voltage rating of 500 V/25 kV. The grid-side model includes a 25 kV distribution line and a 120 kV transmission grid.

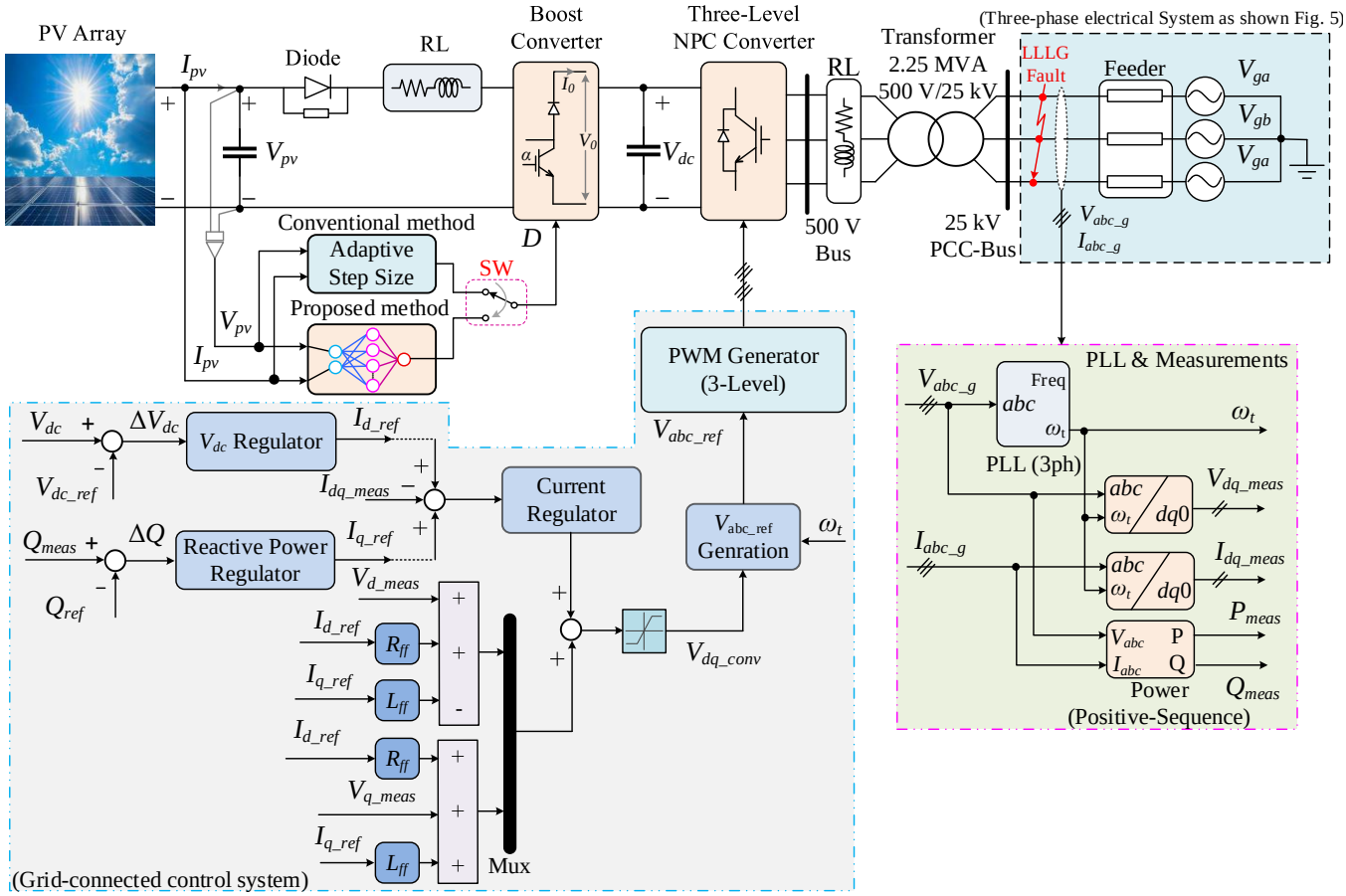

Fig. 2. The control method of the studied grid-connected solar energy.

Fig. 2 illustrates the connection between the PV array and the grid, which involves key components such as the solar panel, boost converter, DC link [31], three-phase inverter, RL filter, step-up transformer, and the electrical grid. In this system, the grid-connected PV uses a three-level NPC inverter and a sophisticated control structure that integrates artificial intelligence. The input energy from the PV array is processed through a diode and an RL filter before entering the boost converter, which steps up the V_{pv} to the DC link voltage V_{dc}. The MPPT control is executed in parallel by two algorithms: the traditional P&O algorithm, which uses an adaptable step size, and the proposed LM-based algorithm. This enables the system to switch flexibly between these two algorithms depending on the actual operating conditions.

The MPPT signal is then used to control the boost converter's duty cycle (D). The DC voltage from the boost converter is fed to the three-level NPC inverter, where it is converted to a three-phase AC voltage and filtered by the RL circuit. The signal then passes through the transformer and is connected to the grid via the distribution line. In terms of control, the system employs a double closed-loop control strategy, comprising current control and reactive power control. The measured outputs from the grid, V_{abc_g} and I_{abc_g}, are fed into a phase-locked loop (PLL) block to extract synchronized components such as frequency, real power P_{mean}, and reactive power Q_{mean}, as well as voltage and current components in the dq frame.

The reactive power regulator block handles the error between the actual and reference reactive power Q_{ref}, adjusting the reference current I_{q_ref}. Similarly, the V_{dc} regulator block controls the reference current I_{d_ref} to maintain a stable DC voltage. All control signals, I_{d_ref} and I_{q_ref}, are compared with the actual currents I_{d_mean} and I_{q_mean}, and the error is sent to the current regulator block to compute the control voltage V_{dq_conv}, which generates the three-phase reference voltage V_{abc_ref} for the three-level PWM controller.

2.1. Photovoltaic Array Model

The goal of equivalent circuit models [29] is to represent the overall I-V characteristic of a PV cell, module, or array as a continuous mathematical relationship involving key electrical variables. A PV array is formed by connecting multiple PV modules in series to achieve the desired voltage and in parallel to provide the required current. This

configuration allows the system to efficiently meet specific power requirements. The equivalent circuit model representing a PV module arranged in n_p parallel and n_s series connections is illustrated in Fig. 3 [28].

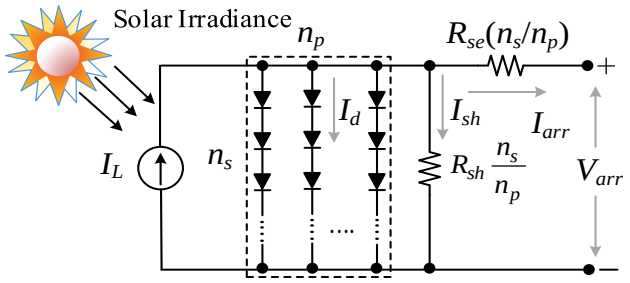

Fig. 3. Electrical equivalent model of a photovoltaic array.

To mathematically describe the equivalent circuit of a PV cell, Kirchhoff's current law is applied, leading to the following expression for the output current [29].

$$I_{arr} = I_L - I_d - I_{sh} \tag{1}$$

where I_L is the photocurrent generated by sunlight, I_d is the loss diode current, and I_{sh} is the photocurrent generated by sunlight. The diode current I_d in a single-diode PV model follows the Shockley equation for an ideal diode [30].

$$I_d = I_s\left(\exp\left(\frac{(V_{arr} + R_{se}I_{arr})q}{n(kT_c/q)}\right) - 1\right) \tag{2}$$

where I_s is the reverse saturation current of the diode, q is the electron charge 1.6×10^{-19} C, n is the diode ideality factor typically between 1 and 2, R_{se} is the internal series resistance, V_{arr} is the terminal voltage of the PV cell, k is the Boltzmann's constant 1.38×10^{-23} J/K, and T_c is the is the cell's junction temperature in Kelvin. Meanwhile, the shunt current I_{sh}, caused by leakage through the shunt resistance R_{sh}, is given as follows.

$$I_{sh} = \frac{(V_{arr} + R_{se}I_{arr})q}{R_{sh}} \tag{3}$$

Combining these relationships, the final expression for the output current of the single-diode PV model as follows.

$$I_{arr} = I_L - I_s A - \frac{(V_{arr} + R_{se}I_{arr})q}{R_{sh}} \tag{4}$$

in with $A = \exp\left(\frac{(V_{arr} + R_{se}I_{arr})q}{n(kT_c/q)}\right) - 1$.

This comprehensive formulation captures both the diode's nonlinear characteristics and the effects of resistive losses within the PV cell. As illustrated in Fig. 3, the equivalent circuit of a PV array consists of multiple PV cells arranged with n_s cells in series and n_p strings in parallel. The overall output current of the array can be expressed using the following relation.

$$I_{arr} = n_p I_L - n_p I_s B - \left(\frac{(V_{arr} + R_{se}(n_s/n_p)I_{arr})q}{R_{sh}(n_s/n_p)}\right) \tag{5}$$

where $B = \exp\left(\frac{(V_{arr} + R_{se}(n_s/n_p)I_{arr})q}{n_s n(kT_c/q)}\right) - 1$, in which V_{arr} is the total voltage of the array, and I_{arr} is the total output current. Therefore, the reverse saturation I_s is the diode current, n is the diode coefficient.

The simulation and demonstration are based on a Solarex PV module, Canadian Solar Inc. CS5P-220M [31], consisting of 66 polycrystalline cells connected in series Table 1. The I-V and P-V characteristics of the P-V array are illustrated in Figs. 4a and 4b.

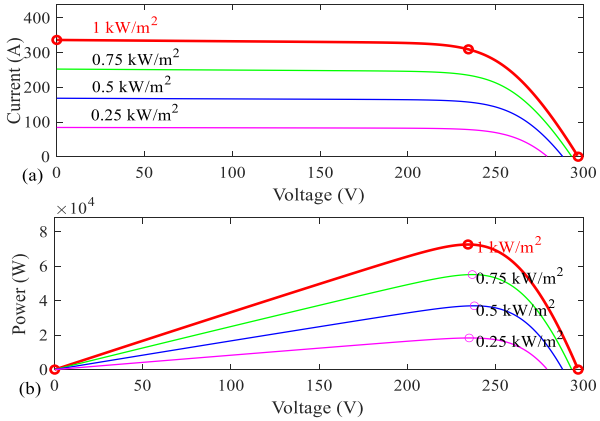

Fig. 4. Specifications of a PV array; (a) the I-V characteristic and (b) the P-V characteristic.

Table 1. The unique electrical properties of a single module

PV panel parameters	Symbols	Values
Maximum power	P_{max}	219.961W
Cells per module	n_{arr}	96
Open circuit voltage	V_{oc}	59.40 V
Short-circuit current	I_{sc}	5.10 A
Voltage at MPP	V_{mp}	46.90 V
Current at MPP	I_{mp}	4.690 A
Temperature coefficient of V_{oc}	%/deg.C	-0.374
Temperature coefficient of I_{sc}	%/deg.C	0.089
Cell-temperature	t_c	25 ºC

2.2. DC/DC Converter Model

One of the essential components of this system is the DC/DC boost converter, which increases the voltage from the PV array to the level required for conversion to AC via the inverter and grid integration. This converter plays a vital role in boosting the DC voltage from the PV array to the optimum level for efficient use in conversion to AC and grid integration, as shown in Fig. 2. The DC/DC boost converter is controlled by the duty cycle, with the output voltage V_0 and current I_0 related to the input voltage and current as follows:

$$\begin{cases} V_0 = \dfrac{V_{pv}}{1-\alpha} \\ I_0 = I_{pv}(1-\alpha) \end{cases} \quad (6)$$

where α is obtained as the output of the MPPT control system.

2.3. RL Filter

The RL filter is incorporated into the inverter to enhance the load current and minimize switching losses in the power components. The inductance value is determined by the current ripple, which typically ranges from 15% to 25% of the rated current. To calculate the appropriate inductance, the maximum current ripple can be calculated as follows.

$$\Delta i = \frac{1}{8}\frac{V_{dc}}{L_f f_{sw}} \quad (7)$$

where V_{dc} is the DC voltage, L_f is the filter inductance, and f_{sw} is the inverter switching frequency. The inductance value L_f in this system is typically set so that the current ripple does not exceed 20% of the rated current. The RL filter plays a crucial role in minimizing inverter-induced harmonic distortion, improving current quality, and mitigating negative impacts on the system's electronic devices.

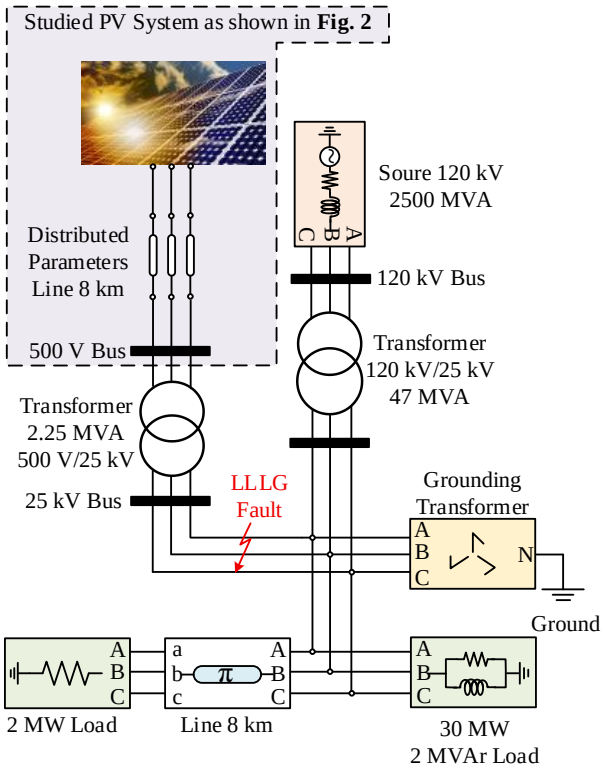

Fig. 5. The model of a three-phase electrical system.

2.4. Model of Different Grid Elements

This model simulates a three-phase electrical system, including key components such as a three-phase transformer, three-phase power source, transmission lines, and RLC loads in Fig. 5. The transformer has an input voltage of 120 kV and an output voltage of 25 kV, with a power rating of 47 MVA, which adjusts the voltage between different levels of the system. The three-phase power source provides energy to the system, with a voltage of 120 kV and a power rating of 2500 MVA. The model also features a grounding transformer to safeguard the system in the event of faults, ensuring the safety of both personnel and equipment.

The transmission lines, with lengths of 8 km, 2 km, and 6 km, model the distributed parameters such as resistance and reactance, which affect the power transmission and system efficiency. The three-phase parallel RLC loads, rated at 30 MW and 2 MW, simulate energy-consuming devices, enabling analysis of the load's impact on system stability. Voltage and current measurements at key points enable monitoring and ensure proper system operation, allowing early fault detection and performance optimization. This model helps analyze the stability and efficiency of the three-phase electrical system when the system operates under normal conditions and when an LLLG occurs.

3. Proposed Control Solution for Maximum Power Point Tracking

3.1. Dynamic Step Size Tuning Solution

This improved P&O MPPT algorithm adjusts the dynamic step-size tuning during MPP tracking. The process begins by measuring the voltage and current of the PV array at a time. The PV power at this time is calculated as follows.

$$P_{pv}(t) = V_{pv}(t) I_{pv}(t) \quad (8)$$

Next, the algorithm calculates the change in power and voltage between time (t) and ($t-1$), as follows.

$$\Delta P_{pv}(t) = V_{pv}(t) I_{pv}(t-1) \quad (9)$$

$$\Delta V_{pv}(t) = V_{pv}(t) V_{pv}(t-1) \quad (10)$$

This calculation of the changes helps the system understand the trend in power and voltage, allowing it to decide the direction of the next adjustment. Once the changes in power and voltage are computed, the algorithm calculates the step-size adjustment as follows.

$$\Delta D = N(\text{abs}(\Delta P_{pv} + \Delta V_{pv} \Delta I_{pv})) \quad (11)$$

where N is a scaling factor that helps adjust the step size appropriately. When there is a significant change in power, the step size will be large to help track the MPP quickly. Conversely, when power changes are small, the step size decreases to avoid oscillations around the MPP.

The algorithm continues by checking three key conditions. If $\Delta P_{pv}(t) = 0$, indicating no change in power, the algorithm will not change the step size and will continue tracking the current state. If $\Delta P_{pv}(t) > 0$, meaning power is increasing, the algorithm will increase the step size to track the MPP faster. If $\Delta P_{pv}(t) < 0$, meaning power is decreasing, the algorithm will reduce the step size and reverse direction to move closer to the MPP.

The step-size adjustment is crucial for improving the efficiency of the MPPT algorithm, enabling the system to dynamically adapt to changing environmental conditions, minimize oscillations around the MPP, and thereby ensure faster convergence.

$$D(t+1) = D(t) \pm \Delta D \tag{12}$$

where $D(t)$ is the duty cycle at time, $D(t + 1)$ is the duty cycle at the next time step $(t + 1)$, and $\pm\Delta D$ means the step size can either be added or subtracted, depending on the change in power ΔP between the two time steps. Finally, after each adjustment, the values of $D(t)$, $V_{pv}(t)$, $I_{pv}(t)$, and $P_{pv}(t)$ are stored and used in the next iterations, allowing the system to continue tracking the MPP stably. This method helps reduce oscillations and improve MPPT accuracy, especially under rapidly changing environmental conditions such as solar irradiance and temperature. Fig. 6 illustrates the flowchart of the proposed P&O MPPT approach with an adaptable step size.

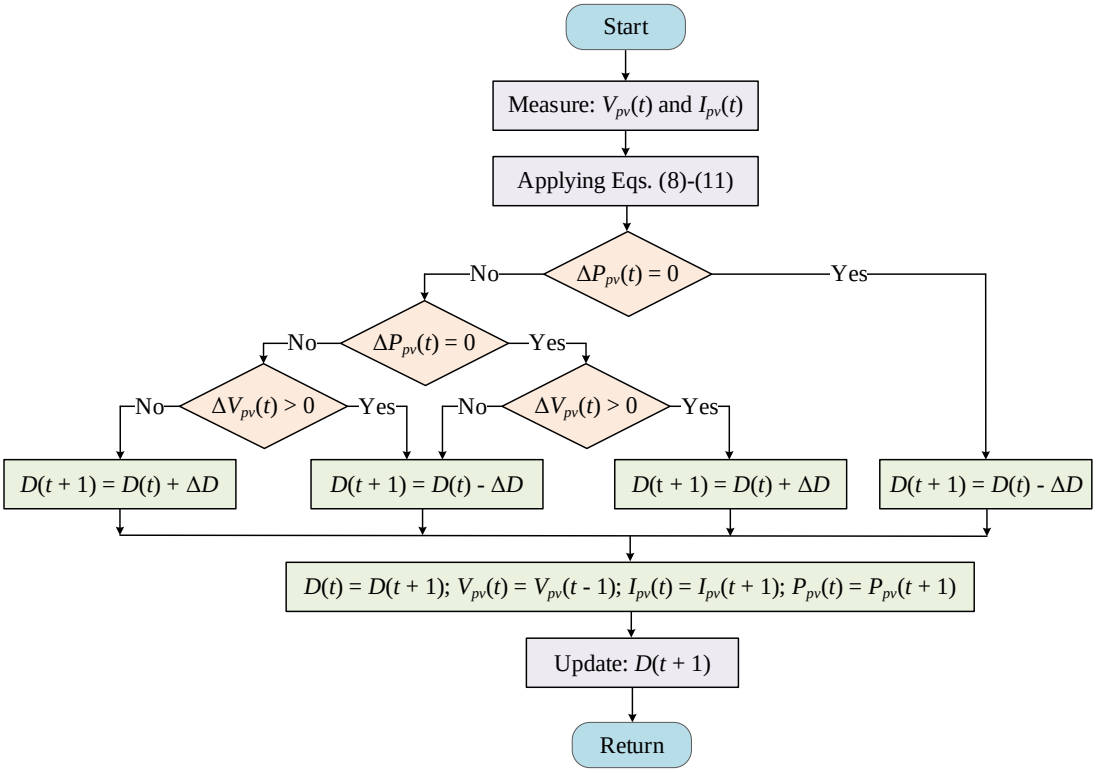

Fig. 6. Flowchart of the P&O MPPT algorithm using the dynamic step size tuning solution.

3.2. Artificial Neural Network Solution

Fig. 7 presents a neural network architecture with two layers, each incorporating bias (b) and weight (W) elements. The inputs are first combined with the bias, then passed through an activation function, represented by the curved line in Layer 10 and the straight line in Layer 2. This design allows the input data, which includes two signals as voltage and current, to undergo nonlinear transformations. As a result, the network is capable of learning complex patterns and relationships between the input data and the output signal, which corresponds to the D [32].

LM is a widely used optimization algorithm for training an ANN. It is especially effective at addressing nonlinear regression issues and determining optimal weights to minimize the discrepancy between predicted and target outputs. The LM method combines the Gauss-Newton and steepest descent approaches, iteratively adjusting the weights to reduce the error, typically quantified by the mean squared error (MSE).

The deployment of ANN optimized via the LM algorithm has emerged as a cornerstone for enhancing the efficacy of PV systems. This computational approach is not merely an engineering preference but a strategic necessity to minimize the carbon footprint of energy-intensive processes by maximizing renewable penetration. The architectural workflow begins with the acquisition of stochastic physical signals: PV voltage V_{pv} and current I_{pv}. To ensure numerical stability and prevent gradient saturation, a common pitfall, deep learning input signals are subjected to a normalization process within the input block. This maps the physical domain into a closed interval using the min-max transform:

$$x_{\text{norm}} = 2\frac{x - x_{\min}}{x_{\max} - x_{\min}} - 1 \tag{13}$$

where $x_{\min}$ and $x_{\max}$ are the minimum and maximum values of

the training dataset, respectively, and x is the actual value V_{pv} or I_{pv}. Upon entering Layer 1, the system uses a tapped-delay line. From my experience, this is critical for PV applications as it provides the network with temporal awareness, allowing it to remember previous irradiance states. The mathematical core of this layer consists of 15 parallel neurons. Each neuron i computes a weighted sum of the inputs based on the input weight matrix IW{1,1}, defined as:

$$z_i = \sum_{j=1}^{R} w_{i,j} p_j \tag{14}$$

This weighted input is then biased by b_i to adjust the decision threshold as follows.

$$n_i = z_i + b_i \tag{15}$$

To capture the highly nonlinear characteristics of semiconductor devices under varying environmental conditions, the Hyperbolic Tangent Sigmoid activation function is employed and can be defined as follows.

$$a_i = \text{tansig}(n_i) = \frac{e^{n_i} - e^{-n_i}}{e^{n_i} + e^{-n_i}} \tag{16}$$

The hallmark of this specific implementation is the LM training protocol. Unlike standard gradient descent, the LM algorithm provides a robust bridge between the Gauss-Newton method and the steepest descent. It updates the weight vector w by approximating the Hessian matrix and can be calculated as follows.

$$w_{k+1} = w_k - [J^T J + \mu I]^{-1} J^T e \tag{17}$$

where J is the Jacobian matrix and μ is the damping factor. This ensures rapid convergence even in complex search spaces, which is vital for real-time MPPT control. The latent features processed in Layer 1 are then aggregated in the output Layer 2 through a linear transfer function, denoted as purelin, and computed as follows.

$$a\{2\} = \text{IW}\{2,1\} \times a\{1\} + b\{2\} \tag{18}$$

Finally, the process output block performs de-normalization to translate the network's abstract output into a tangible PWM signal, denoted as D, and determined as follows.

$$D = \frac{(a\{2\}+1)(D_{\max} - D_{\min})}{2} + D_{\min} \tag{19}$$

By integrating ANN-LM control into PV systems to maximize power output from PV arrays using precise nonlinear control, a faster, more stable transition towards high-power renewable energy integration is facilitated. Ultimately, this framework ensures dynamic stability and enhances system efficiency, maintaining optimal operating points even under rapidly changing atmospheric conditions, thereby guaranteeing a robust and sustainable energy architecture.

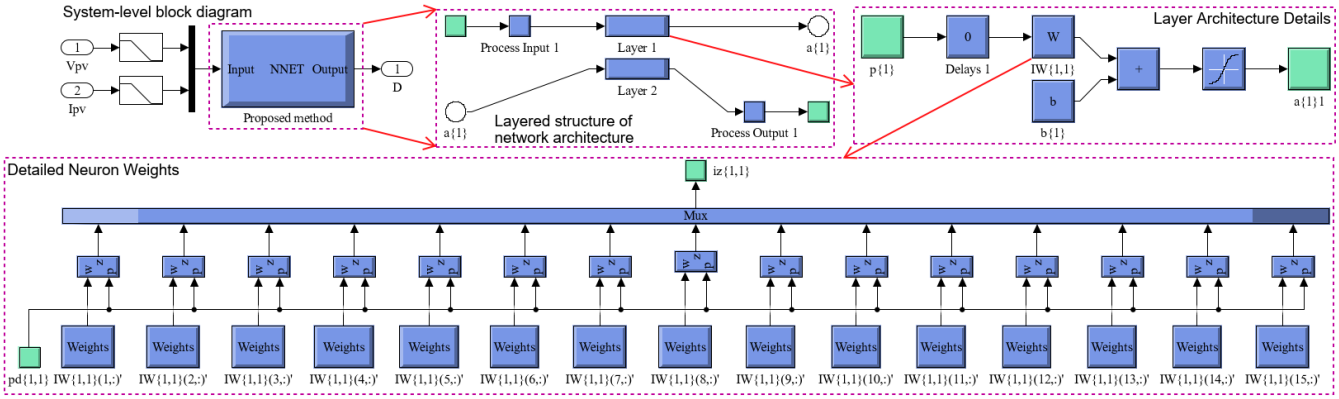

Fig. 7. Feedforward neural network architecture.

The LM algorithm adjusts the step size based on the curvature of the error surface, using a damping parameter to balance local and global search directions. This approach ensures fast convergence and stability while avoiding local minima. LM is effective in approximating the Hessian matrix without requiring direct computation, making it suitable for large networks. The algorithm is also resistant to local minima and automatically adjusts during training. It is widely used in machine learning due to its fast convergence and efficient handling of complex error surfaces [33].

Based on the regression plots in Fig. 8, we observe high accuracy in the artificial neural network training and testing model using the LM algorithm. Specifically, during the Training phase, the training correlation coefficient (R) value is 0.93129; see Fig. 8a. The relationship between the output and target fits well with the dotted line (Y = T). The training R value of 0.93129 indicates that the model has been trained effectively, with relatively small errors between the actual data and the predicted values. In the validation phase, the validation R value of 0.93024, shown in Fig. 8b, indicates

that the model generalizes well when applied to the validation data. The output is still close to the target value, although there is a slight decrease in accuracy compared to the training phase. During the test phase, the test *R* value was 0.93142. As shown in Fig. 8c, the model performs excellently on the test data, achieving a test *R* value of 0.93142. This demonstrates that the model can accurately predict not only on training and validation data but also on completely new data. The overall *R* value of 0.93115; Fig. 8d combines the training, validation, and test phases, showing an overall regression *R* value of 0.93115.

This indicates that the model maintains accurate and stable prediction performance across all datasets. The high regression values across all phases indicate that the LM algorithm has effectively trained the ANN, with minimal error and strong generalization across training, validation, and test data.

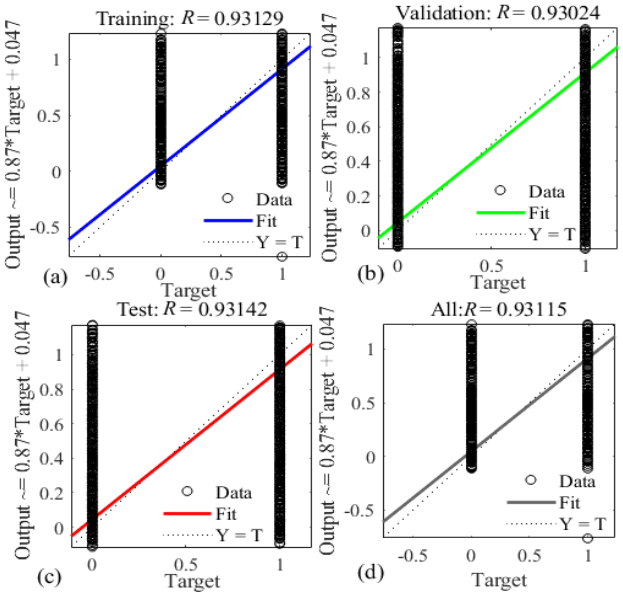

Fig. 8. Regression plot of the LM algorithm with the different correlation coefficient (*R*): (a) the training *R* value of 0.93129, (b) the validation *R* value of 0.93024, (c) the test *R* value of 0.93142, and (d) the overall *R* value of 0.93115.

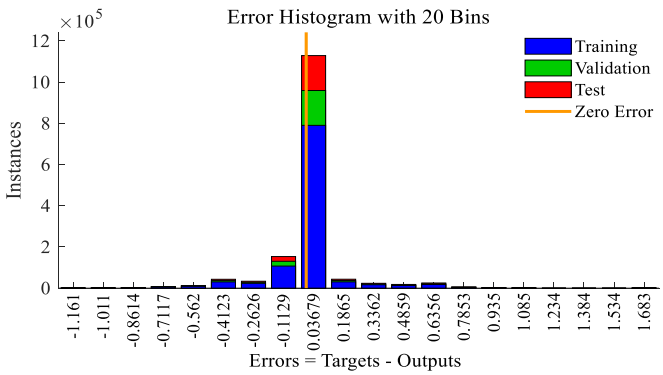

Fig. 9. Error histogram plot of the LM algorithm.

The error histogram in Fig. 9 shows the results obtained with the artificial neural network using the LM algorithm. This histogram consists of a total of 20 bins, with errors ranging from -1.161 to 1.683. The data is distributed across these bins, with errors mainly concentrated in the range from -1.161 to 1.683. Notably, the bar representing 0% error indicates that some samples have zero errors, demonstrating that the model has learned accurately and made almost perfect predictions. These results show that the ANN has effectively optimized the MPPT with minimal error, achieving accurate convergence during the training, test, and validation phases.

Figs. 10a -10c and Fig. 11 illustrate both the training and performance evaluation phases of the artificial neural network used to process the selected dataset. The validation checks for the training dataset, as well as the gradient and momentum (mu) parameters at 1000th epochs, are shown in Fig. 9. The simulation results indicate that at the 1000th epoch, the gradient value is 0.031757, suggesting minimal variance from the training data and a small loss function. These results imply that the cumulative error is primarily due to the decision to generate zero outputs and the average value for each input vector. The effectiveness of the LM algorithm for MPPT is evident from the very low gradient values and the validation tests on the training dataset.

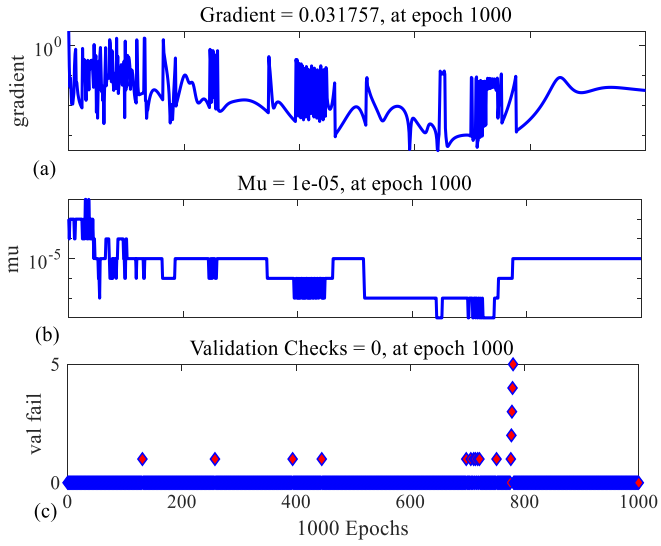

Fig. 10. Training test plot of the LM algorithm; (a) the gradient, (b) the mu, and (c) the valfail.

Fig. 11 shows the MSE for the samples in the training dataset across different epochs, indicating an optimal training outcome at the 1000th epoch. As a result, the dataset achieves the highest validation performance after 1000th epochs. Based on the simulation results, the validation performance of 0.030737 at the 1000th epoch is the best. The MPPT estimation using the LM method achieved nearly zero validation performance, indicating a very low error rate.

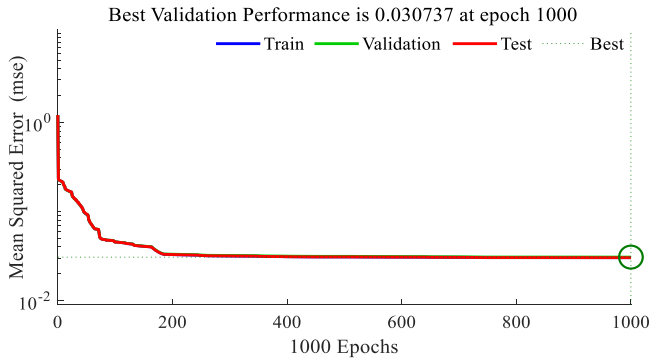

Fig. 11. Performance plot of the LM algorithm.

4. Results and Simulation

A control system for connecting a PV array to the grid has been developed and comprehensively simulated in MATLAB/Simulink. A comparative analysis is performed to evaluate the performance and efficiency of the proposed control strategy. Specifically, the study focuses on assessing the robustness and dynamic response of the controller under two distinct conditions: normal operation and during an LLLG fault. The proposed control system exhibits strong stability and reliable performance in both scenarios, demonstrating its resilience and adaptability to disturbances. The simulation model is constructed and illustrated in Fig. 2, with the PV panel parameters provided in Table 1 and the system parameters presented in Appendix 1.

In the simulation of the system control using the ANN controller trained with the LM algorithm, the following parameters are set: the DC voltage supplied to the rectifier is V_{dc} = 1000 V throughout the simulation, the switching frequency is $T_s = 2.5\times10^{-5}$ seconds, and the simulation time is t = 2.5 seconds in without fault, and t = 1.5 seconds in with fault. The simulation, conducted in MATLAB/Simulink, aims to evaluate the performance of the proposed MPPT control method compared to the conventional method that incorporates a dynamic step-size tuning solution.

4.1. Case Study 1

Considering Normal Operating Conditions: The initial analysis of the grid for all parameters is carried out without any faults in the distribution network, with irradiance set as shown in Fig. 12. Based on Figs. 13a - 13c, both MPPT algorithms, the conventional method and the proposed method, maintain stable voltage and current for the PV arrays, with the proposed method demonstrating better stability throughout the simulation. Specifically, while the voltage of PV arrays remains stable at high levels in both methods, the proposed method maintains smoother power and achieves optimal values more quickly compared to the conventional method.

Fig. 14 illustrates the DC-link voltage under the control of two MPPT algorithms: the proposed method and the conventional method. The DC-link voltage is controlled to maintain stability, as indicated by the red reference voltage line. From the figure, it can be observed that while the conventional method causes significant fluctuations in the DC-link voltage, the proposed method maintains a more stable voltage with fewer variations.

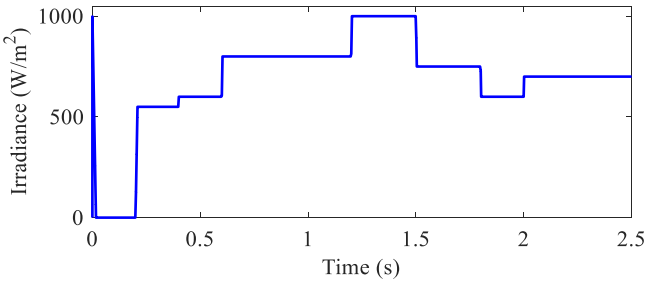

Fig. 12. The solar irradiance pattern applied to PV arrays.

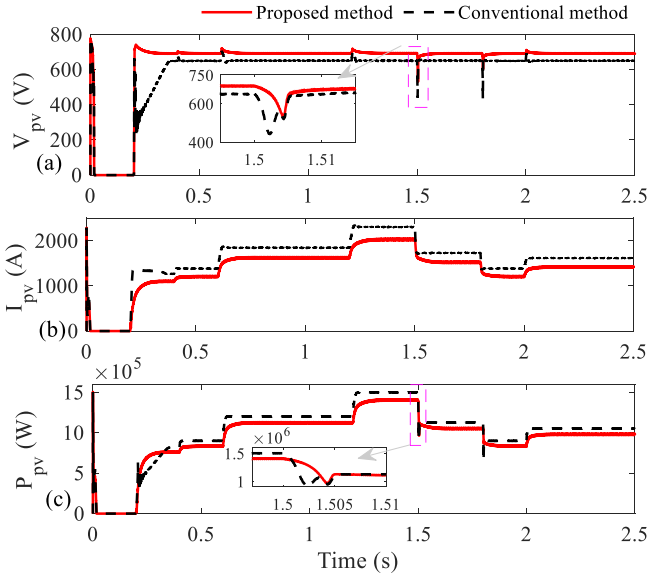

Fig. 13. The PV panel parameters: (a) the voltage, (b) the current, and (c) the active power.

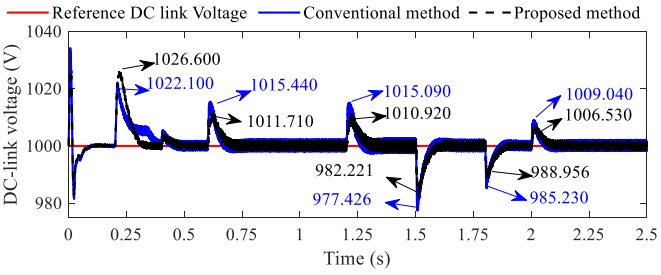

Fig. 14. Dynamic performance of the DC-link voltage under normal operating conditions.

The current of the PV arrays increases similarly in both methods, but the proposed method experiences fewer fluctuations. Table 2 summarizes the voltage, current, and power values for the two panels, showing that from 0.2 to 0.4 seconds, the power of both PV arrays increases, but the conventional method produces lower power than the proposed method. Meanwhile, the proposed method

maintains more stable power and is less affected by changes in irradiance conditions.

Specifically, with the conventional method, the DC-link voltage fluctuates strongly around the reference value, as shown in Table 3, and both methods exhibit voltage overshoot. The percentage overshoot total (%POT) indicates that the proposed method is more effective at maintaining a stable DC-link voltage than the conventional method. Specifically, the conventional method yields a total % POT of 1.496%, while the proposed method yields 1.292%. This indicates that the proposed method causes less fluctuation and overshoot, helping to maintain better voltage stability throughout the operation.

Figs. 15a and 15b show the voltage at the PCC bus with a constant, where the peak voltage per phase is 2×10^4 V. Regardless of variations in the injected power from the combined system, the PCC bus voltage for both the conventional method and proposed methods remains stable. This demonstrates the ability of both methods to maintain voltage stability despite fluctuations in irradiance or changes in input power conditions.

Table 2. Summary of PV array values by the conventional and the proposed methods in case study 1

Time (seconds)	PV array values					
	Conventional method			Proposed method		
	V_{pv} (V)	I_{pv} (A)	$P_{pv}\times10^5$ (W)	V_{pv} (V)	I_{pv} (A)	$P_{pv}\times10^5$ (W)
0 - 0.2	0	0	0	0	0	0
0.2 - 0.4	646.017	1333.550	8.23825	689.519	1086.800	7.53377
0.4 - 0.6	645.563	1377.380	8.99997	689.959	1194.290	8.26264
0.6 - 1.2	647.657	1873.300	12.02330	690.494	1611.230	11.16610
1.2 - 1.5	647.860	2317.430	15.01660	691.413	2013.750	13.95530
1.5 - 1.8	653.187	1721.640	11.26930	690.257	1507.730	10.44850
1.8 - 2.0	645.653	1376.910	9.00257	689.373	1194.610	8.27390
2.0 - 2.5	647.220	1607.700	10.51800	690.145	1404.500	9.87954

Table 3. Overshoot and stability of DC-link voltage for the conventional and the proposed methods

Time (seconds)	Stidied values				
	References	V_{dc} (V)		POT (%)	
	V_{dc} (V)	Conventional method	Proposed method	Conventional method	Proposed method
0.2	1000	1022.100	1026.600	2.162	2.591
0.6		1015.440	1011.710	1.520	1.157
1.2		1015.090	1010.920	1.486	1.080
1.5		977.426	982.221	2.309	1.810
1.8		985.230	988.956	1.499	1.116
2.0		1009.040	1006.530	0.895	0.648
Total				1.496	1.292

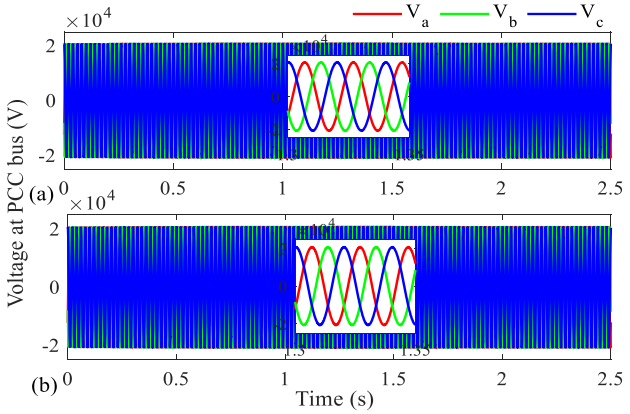

Fig. 15. Dynamic performance of the voltage at the PCC bus under normal operating conditions: (a) proposed method and (b) the conventional method.

The current data for the PCC bus is distributed across three phases, as shown in Figs. 16 and 16b. When irradiance conditions change, slight variations in the current of each phase can be observed, but the voltage remains stable and undistorted, indicating the effectiveness of both the conventional and proposed methods in maintaining voltage quality under external changes. This shows that both methods are effective in maintaining system stability, especially when irradiance and injected power fluctuate.

Based on Figs. 17 and 18, it can be observed that both the active and reactive power of the system under the control of the conventional and proposed method algorithms remain stable, with the proposed method showing superior stability. Specifically, the active power of the system remains stable at 2.5 MW, with the proposed method more effective at maintaining this level without significant fluctuations, whereas the conventional method shows slight variations in active power. Regarding reactive power, the system maintains 0.911 MVAr, indicating a relatively high level, while the power factor remains close to 1, ensuring high operational efficiency and minimizing energy losses. Both algorithms maintain stable reactive power at 0.911 MVAr, but the proposed method better preserves the stability of both active and reactive power, particularly under changing irradiance conditions.

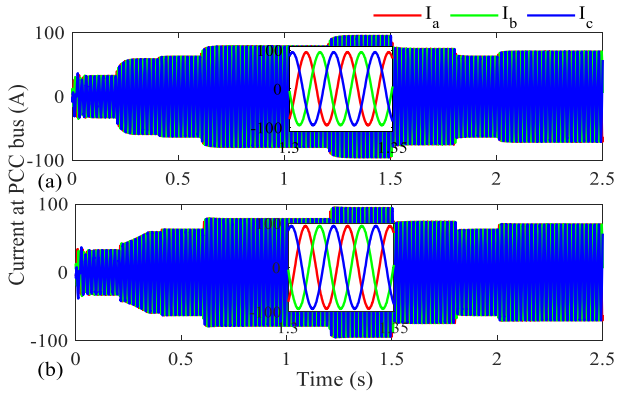

Fig. 16. Dynamic performance of the current at the PCC bus under normal operating conditions: (a) proposed method and (b) the conventional method.

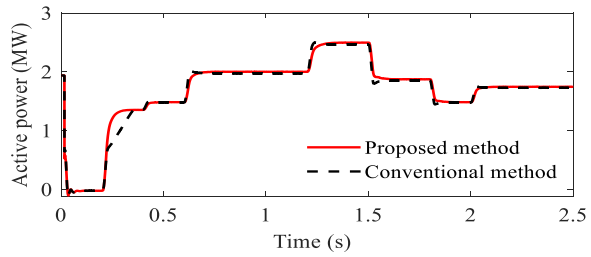

Fig. 17. The active power under normal operating conditions.

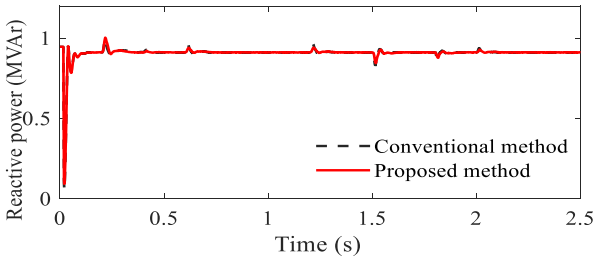

Fig. 18. The reactive power under normal operating conditions.

Based on the analysis of Figs. 19a and 19b show a clear distinction between the two MPPT control methods, the proposed method, and the conventional method, in terms of voltage waveforms, phase current, and harmonic distortion (THD). Although the THD of the input voltage is relatively high in both methods, with the proposed method showing a THD of 38.99% and the conventional method at 39.07%, this is primarily due to the DC-AC conversion process in the inverter and the rapid changes in irradiance conditions. However, both methods maintain very low THD in phase current, 0.04%, indicating nearly ideal current quality with negligible harmonic distortion.

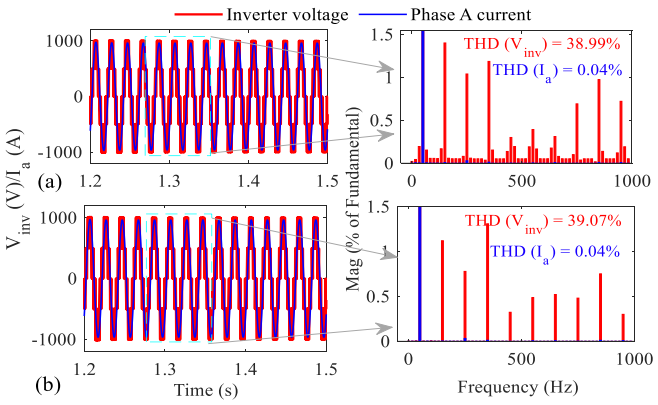

Fig. 19. Comparison of output voltage waveform, phase current, and their THD under normal operating conditions: (a) the proposed method and (b) the conventional method.

The proposed method maintains higher stability in voltage and phase current, with fewer fluctuations than the conventional method, resulting in better system performance. Despite the high harmonic distortion in the input voltage, the proposed method still maintains stable reactive power and better energy quality. In contrast, the conventional method shows greater fluctuations in voltage and current waveforms, leading to higher THD in the input voltage, yet it keeps

reactive power at a low level, indicating reasonable performance under varying light conditions.

4.2. Case Study 2

Considering Grid Fault Condition: LLLG is a common electrical fault that frequently occurs in industrial environments, particularly in renewable energy systems that utilize power electronics, such as inverters and DC-AC converters. When this fault occurs, excessive current can flow, causing significant fluctuations in the system's voltage and current parameters, and posing a risk of damage to semiconductor devices due to their fast response times. Therefore, managing and stabilizing voltage and current during the fault event is crucial to protect the system [34]. In this simulation, an LLLG fault at the PCC bus with a duration of 0.1 seconds occurs at 0.4 seconds, while the irradiance is maintained at 1000 W/m^2 throughout the simulation period, as shown in Fig. 20. This fault has a noticeable impact on the operational parameters of the PV arrays.

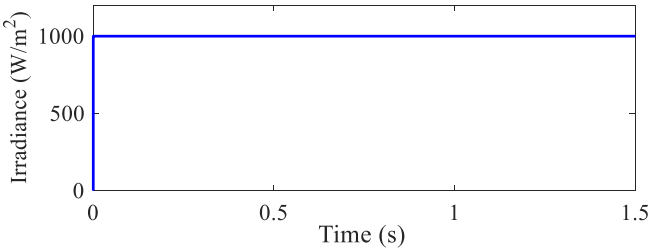

Fig. 20. The solar irradiance pattern applied to PV arrays.

Specifically, as shown in Fig. 21a, the voltage of the PV arrays both increased sharply during the LLLG fault. Within 0.4 to 0.5 seconds, the conventional method caused the voltage to increase from about 650 to 780 V, while the proposed method increased from 690 to 780 V. After the fault was cleared within about 0.5 seconds, the voltage began to recover and stabilize back to its original value of about 650 V for the conventional method and 690 V for the proposed method. Regarding the current, as shown in Fig. 21b, the current of both PVs decreased significantly during the fault. The current almost dropped to 0 A at the time of the fault, indicating an interruption in the power supply from the PV arrays due to the three-phase fault. After the fault is cleared, Fig. 21b shows that the current recovers and increases again to approximately 2000 A for the conventional method and 2300 A for the proposed method, indicating a gradual return to stability.

Regarding power, Fig. 21c shows that the output power from the PV arrays drops sharply during the LLLG fault. Observing from this figure, the power drops from a high value of about 14×10^5 W to nearly 0 MW for the proposed method and from 15×10^5 W to nearly 0 MW for the conventional method, indicating that both PV arrays are unable to supply power during the fault. However, immediately after the fault is cleared, the power recovers rapidly and stabilizes to its initial level, demonstrating the system's ability to quickly return to normal operation. Thus, although there is a significant drop in voltage, current, and power during the LLLG fault, the system recovers rapidly and maintains stability after the fault is cleared.

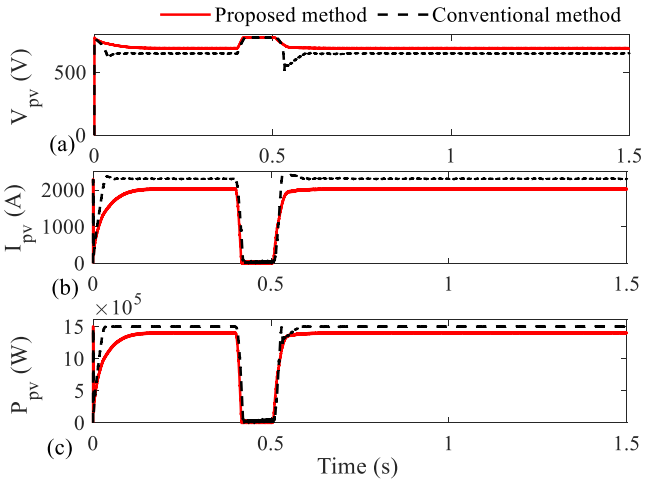

Fig. 21. PV panel parameters: (a) the voltage, (b) the current, and (c) the active power.

The DC voltage suddenly increases at 0.4 seconds, and the conventional method causes it to rise from 1000 to 2071.780 V before dropping back to 1000 V once the fault is cleared, with a settling time of t_{set} = 0.713 seconds. In contrast, the proposed method causes the voltage to rise from 1000 to 1357.660 V before returning to 1000 V when the fault is resolved, with a shorter settling time of t_{set} = 0.539 seconds, demonstrating the proposed method more flexible adjustment and quicker fault recovery, as shown in Fig. 22. The voltage increase for the conventional method is a factor of 2.07 from 1000 to 2071.780 V, while for proposed method, the voltage increase is a factor of 1.36 from 1000 to 1357.66 V.

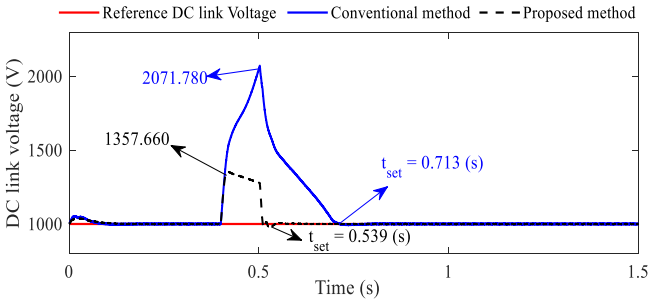

Fig. 22. Dynamic performance of the DC-link voltage under LLLG fault.

The three-phase voltage behavior at the PCC bus during the LLLG fault, using two control methods, the conventional method and the proposed method, is illustrated in Figs. 23a and 23b. The voltage remains constant at 2×10^4 V before the fault. During the fault, the grid voltage drops to zero between 0.4 and 0.5 seconds. The voltage then recovers to its normal level after 0.5 seconds. It is noted that the inverter is off for 0.4 to 0.5 seconds during the fault.

Figs. 24a and 24b present the behavior of the three-phase current at the PCC bus during an LLLG fault under the control of two MPPT methods: the conventional method and the proposed method. In Fig. 24a, the current remains constant at 95 A before the fault occurs, then increases to 560

A during the fault. After the fault is cleared, the current returns to 95 A and stabilizes once the fault is resolved. Similarly, Fig. 24b shows the current at 93 A before the fault, rising to 610 A during the fault, and dropping back to 93 A after the fault is cleared. Once the fault condition ends, the current stabilizes at its normal value of 93 A. Both methods effectively handle the fault, with the proposed method demonstrating slightly better current recovery, suggesting a marginally more efficient response to fault events.

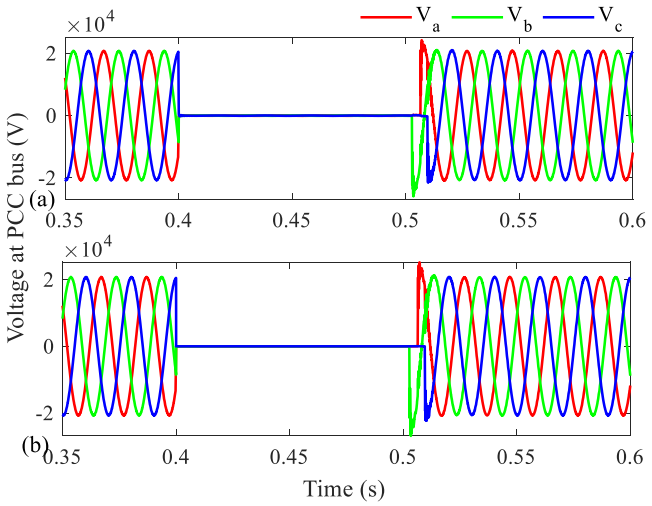

Fig. 23. Dynamic performance of the PCC-Bus voltage under LLLG fault conditions: (a) the proposed method and (b) the conventional method.

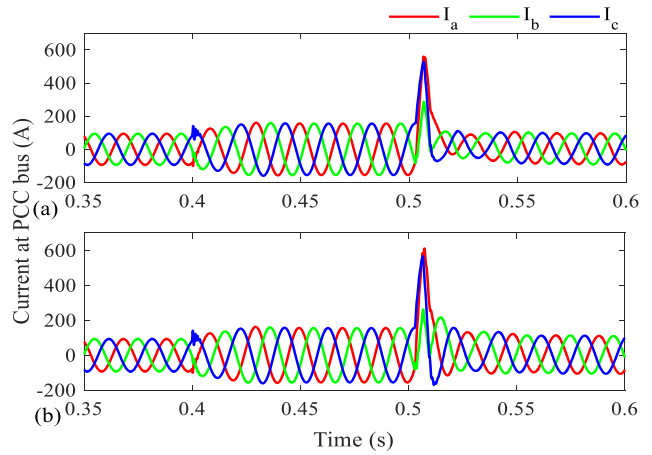

Fig. 24. Dynamic performance of the PCC bus current under LLLG fault: (a) the proposed method and (b) the conventional method.

Based on Figs. 25 and 26, during the LLLG fault, both active power and reactive power for the conventional method and the proposed method experience significant reductions. Specifically, the active power for both methods drops nearly to 0 MW during the fault from 0 to 0.5 seconds. However, the proposed method recovers the active power more quickly, reaching approximately 2.5 MW and stabilizing, whereas the conventional method recovers more slowly, maintaining the power below 2 MW. Regarding reactive power, both methods exhibit substantial fluctuations during the fault, with a peak at the time of the fault. After the fault is cleared, the reactive power of both methods stabilizes at 1.0 MVAr, but the proposed method shows greater reactive power fluctuations, demonstrating its more flexible adjustment and faster recovery compared to the conventional method. In conclusion, the proposed method exhibits faster, more stable power recovery, whereas the conventional method shows slower recovery.

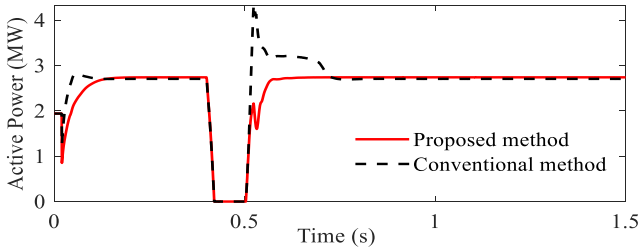

Fig. 25. The active power under LLLG fault.

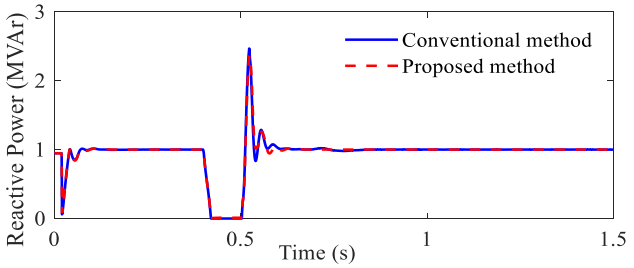

Fig. 26. The reactive power under LLLG fault.

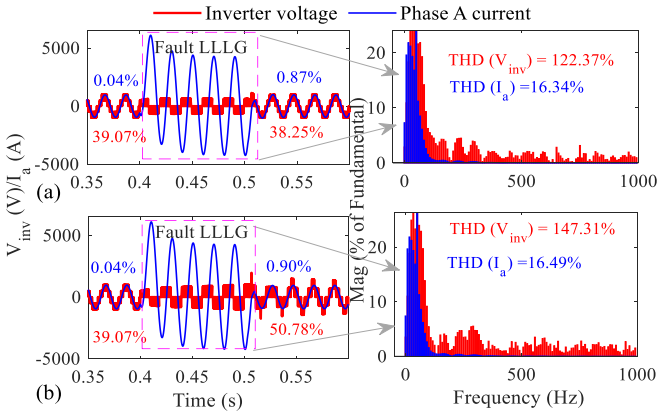

Fig. 27. Comparison of output voltage waveform, phase A current, and their harmonic spectra under LLLG condition: (a) the proposed method and (b) the conventional method.

Table 4. Comparison of inverter voltage and THD (%) of phase A current under conditions of the post-fault, fault-free, and LLLG fault when applying the proposed and the conventional methods

Methods	THD (%)			
	Conditions / Signals	Fault-free	LLLG fault	Post-fault
		(0.35 - 0.4 seconds)	(0.4 - 0.5 seconds)	(0.5 - 0.6 seconds)
Proposed method	V_{inv} (V)	39.07	122.37	38.25
	I_a (A)	0.04	16.34	0.87
Conventional method	V_{inv} (V)	39.07	147.31	50.78
	I_a (A)	0.04	16.49	0.90

Based on Figs. 27a and 27b, and Table 4, during the LLLG fault, both the conventional method and the proposed method exhibit significant fluctuations in voltage and phase current, but the proposed method demonstrates more stable and effective control. Specifically, the conventional method has a voltage THD of 147.31%, which is much higher than the proposed method's 122.37%, indicating that the proposed method maintains a more stable voltage quality during the fault. Although both methods exhibit voltage fluctuations during the fault, the conventional method shows greater distortion, indicating instability in maintaining the output voltage. Regarding phase current, the conventional method has a THD of 50.78%, which is higher than the proposed method at 38.25%, indicating that the conventional method experiences more significant current fluctuations during the fault. The proposed method offers better stability with lower THD, less distortion, and higher current control stability. Overall, the proposed method demonstrates faster recovery and better maintenance of power quality compared to the conventional method during the LLLG fault, thanks to its stability in both voltage and current. The lower THD in both voltage and current for the proposed method demonstrates that it is more effective at minimizing distortion and maintaining system stability under fault conditions.

5. Conclusion

This paper has presented the development and simulation of a grid-connected solar energy conversion system utilizing a three-level NPC inverter and an advanced MPPT controller based on an artificial neural network (ANN) trained with the Levenberg-Marquardt (LM) algorithm. The study evaluated the system's performance in terms of stability, power quality, and fault resilience through a comparative analysis with a conventional dynamic-step-size P&O method. Based on the obtained simulation results, the following conclusions are drawn:

The proposed ANN-LM control strategy significantly improves the DC-link voltage stability under varying irradiance conditions. The quantitative analysis shows that the proposed method reduces the total percentage overshoot to 1.292%, compared to 1.496% for the conventional method. This result indicates that the neural network's nonlinear mapping capability enables more precise tracking of the maximum power point with minimal oscillation, thereby reducing energy losses and mechanical stress on system components compared to traditional gradient-based algorithms.

The simulation of the system under a three-phase-to-ground (LLLG) fault scenario demonstrates the superior dynamic response of the proposed controller. The system utilizing the ANN-LM algorithm achieves a voltage recovery settling time of 0.539 seconds, which is markedly faster than the 0.713 seconds required by the conventional method. Additionally, the voltage surge during the fault is limited to 1.36 times the nominal value with the proposed method, versus 2.07 times with the traditional approach. This rapid recovery is attributed to the predictive nature of the trained neural network, which can instantly estimate the optimal duty cycle, even during severe voltage dips, unlike the reactive adjustments of the P&O method.

The proposed method maintains better power quality during fault conditions, as evidenced by the total harmonic distortion (THD) analysis. During the LLLG fault, the THD of the inverter voltage for the proposed method is 122.37%, significantly lower than the 147.31% recorded for the conventional method; similarly, the phase current THD is reduced to 38.25% compared to 50.78%. This peculiarity suggests that the ANN's robust control of the DC-link voltage effectively mitigates the propagation of harmonic distortions through the inverter during transient states, ensuring safer grid integration.

The application of the Levenberg-Marquardt algorithm for training the neural network resulted in a high correlation coefficient equal to 0.931 across training, validation, and testing phases. This quantitative indicator confirms the MPPT model's precision. The essence of this result lies in the LM algorithm's ability to combine the speed of the Gauss-Newton method with the stability of the steepest descent method, preventing the network from getting trapped in local minima and ensuring reliable performance across diverse operating conditions.

Acknowledgements

The authors would like to thank the managers and the members of the "*International Journal of Smart Grid*" for their valuable remarks and suggestions.

Author Contributions

Le Van Dai was involved in conceptualization, investigation, methodology, software, supervision, writing-original draft, writing -review and editing, formal analysis, and resources. Huynh Hoang Bao Nghia was the methodology, investigation, formal analysis, software, and writing-original draft. All authors have read and agreed to the published version of the manuscript.

Conflict of Interest

The authors declared no potential conflicts of interest with respect to the research, authorship, and/or publication of this article.

Nomenclature

ANN	Artificial Neural Networks
LM	Levenberg-Marquardt
PV	Photovoltaic
LLLG	Three-Phase Ground Faults
MPP	Maximum Power Point
MPPT	Maximum Power Point Tracking
P&O	Perturb and Observe
PLL	Phase-Locked Loop
DC	Direct current
AC	Alternating current
THD	Total Harmonic Distortion
POT	Percentage Overshoot Total
NPC	Neutral Point Clamped

Appendix

Appendix 1. Element parameters.

Manufacture	Symbols	Values
➢ *Three-phase Transformer* (*Yg/Dlta1*)		
Nominal power and frequency	P_n	2.25 MVA
	f_n	50 Hz
Winding 1 parameters	V_1	25e3 V
	R_1	0.001 pu
	L_1	0.03 pu
Winding 2 parameters	V_2	500 V
	R_2	0.001 pu
	L_2	0.03 pu
Magnetization resistance	R_m	200
Magnetization inductance	L_m	200
➢ *Three-phase Transformer* (*Yg/Dlta1*)		
Nominal power and frequency	P_n	47 MVA
	f_n	50 Hz
Winding 1 parameters	V_1	120 kV
	R_1	0.08/30 pu
	L_1	0.08 pu
Winding 2 parameters	V_2	25 kV
	R_2	0.08/30 pu
	L_2	0.08 pu
Magnetization resistance	R_m	500 pu
Magnetization inductance	L_m	500 pu
➢ *Boost Converter*		
Device on-state resistance	R_{db}	$1\times10^{-3}\,\Omega$
Snubber resistance	R_{sb}	$1\times10^{-6}\,\Omega$
➢ *Three-Level NPC Converter*		
Device on-state resistance	R_{on}	$0.5\times10^{-4}\,\Omega$
Snubber resistance	R_{sn}	$1\times10^{-6}\,\Omega$
➢ *Series RL Branch*		
Resistance	R_{sb}	$1\times10^{-3}\,\Omega$
Inductance	L_{sb}	1×10^{-3} H
➢ *Three-Phase Series RL Branch*		
Resistance	R_p	1e-3 Ω
Inductance	L_p	44.2×10^{-6} H
➢ *Invert Control* (*Control system for a* 2 *MW,* 1*MVAr,* 25 *kV, Grid-Connected Inverter*)		
Power	P_n	2.25 MVA
Frequency	f	50 Hz
Primary voltage	V_p	25 kV
Secondary voltage	V_s	500 V
DC voltage	V_{dc}	1.0 kV
Feedforward Values	R_{ff}	0.004 pu
	L_{ff}	0.21 pu
➢ *MPPT Controller*		
Duty cycle initial value	D	0.35
D limits [Upper, Lower]	Upper	0.8
	Lower	0.3
Increment value for the P and O algorithm		60×10^{-6}

Measurement filter cutoff frequency		1000 Hz
➢ *Distributed Parameters* (8 *km*, 2 *km*, 6 *km*, 50 *Hz*)		
Resistance pu length (Ω/km) [NxN matrix]	NxN	0.1153
	matrix	0.413
Inductance pu length (H/km) [NxN matrix]	NxN	1.05×10^{-3}
	matrix	3.32×10^{-3}
Capacitance pu length (F/km) [NxN matrix]	NxN	11.33×10^{-9}
	matrix	5.01×10^{-9}
➢ *Grounding Transformer*		
Nominal power and frequency	P_n	3e6 VA
	f_n	50 Hz
Nominal voltage (Vrms)	V	25 kV
Zero-sequence resistance and reactance	R_0	0.25 Ω
	X_0	7.5 Ω
Magnetization branch	R_0	1.0417×10^5 Ω
	X_0	1.0417×10^5 Ω

References

[1] Z. Reguieg, I. Bouyakoub, F. Mehedi, and F. Bouhadji, "Optimizing Power Quality: Simulation of UPQC Integrated PV with Comprehensive Reliability and Performance Analysis," International Journal of Smart Grid-ijSmartGrid, vol. 8, no. 1, pp. 46-52, 2024, doi: 10.20508/ijsmartgrid.v8i1.333.g338.

[2] V. T. K. Nhi, B. T. Quy, H. H. B. Nghia, and L. V. Dai, "A Robust Hybrid Control Strategy for Enhancing Torque Stability and Performance in PMSM Drives," Electrical Engineering & Electromechanics, no. 6, pp. 64-74, 2025, doi: 10.20998/2074-272X.2025.6.09.

[3] M. Taghavi, H.-J. Yoon, J.-U. Choi, and C.-J. Lee, "Innovative structure of a liquefied natural gas (LNG) process by mixed fluid cascade using solar renewable energy, photovoltaic panels (PV), and absorption refrigeration system," in computer aided chemical engineering, vol. 53: Elsevier, 2024, pp. 2071-2076.

[4] M. Taghavi, H. Salarian, and B. Ghorbani, "Thermodynamic and exergy evaluation of a novel integrated hydrogen liquefaction structure using liquid air cold energy recovery, solid oxide fuel cell and photovoltaic panels," Journal of Cleaner Production, vol. 320, p. 128821, 2021, doi: 10.1016/j.jclepro.2021.128821.

[5] N. V. T. Kieu, N. H. H. Bao, and T. Q. Bach, "A Model Advanced Predictive Current Control Strategy for PMSM Drives with Torque Ripple and Current Harmonic Reduction," Journal of Robotics and Control (JRC), vol. 6, no. 5, pp. 2444-2456, 2025, doi: 10.18196/jrc.v6i5.26908.

[6] B. Ghorbani, G. Salehi, A. Ebrahimi, and M. Taghavi, "Energy, exergy and pinch analyses of a novel energy storage structure using post-combustion CO2 separation unit, dual pressure Linde-Hampson liquefaction system, two-stage organic Rankine cycle and geothermal energy," Energy, vol. 233, p. 121051, 2021, doi: 10.1016/j.energy.2021.121051.

[7] C. N. Dien and H. H. B. Nghia, "Optimizing Permanent Magnet Synchronous Motor Performance Considering Both Maximum Torque Per Ampere and Field Weakening," International Journal of Intelligent Engineering & Systems, vol. 18, no. 1, 2025, doi: 10.22266/ijies2025.0229.81.

[8] Y. Duan, Y. Zhao, and J. Hu, "An initialization-free distributed algorithm for dynamic economic dispatch problems in microgrid: Modeling, optimization and analysis," Sustainable Energy, Grids and Networks, vol. 34, p. 101004, 2023, doi: 10.1016/j.segan.2023.101004.

[9] V. D. Le, "Development of converter configuration and corresponding control strategy for wind turbines using permanent magnet synchronous generator: A Case study," Journal of Energy Systems, vol. 6, no. 4, pp. 484-502, 2022, doi: 10.30521/jes.1025810.

[10] T. T. Nguyen, T. D. Pham, L. C. Kien, and L. Van Dai, "Improved coyote optimization algorithm for optimally installing solar photovoltaic distribution generation units in radial distribution power systems," Complexity, vol. 2020, no. 1, p. 1603802, 2020, doi: 10.1155/2020/1603802.

[11] H. M. H. Farh, A. Fathy, A. A. Al-Shamma'a, S. Mekhilef, and A. M. Al-Shaalan, "Global research trends on photovoltaic maximum power extraction: Systematic and scientometric analysis," Sustainable Energy Technologies and Assessments, vol. 61, p. 103585, 2024, doi: 10.1016/j.seta.2023.103585.

[12] K. Ullah, M. Ishaq, F. Tchier, H. Ahmad, and Z. Ahmad, "Fuzzy-based maximum power point tracking (MPPT) control system for photovoltaic power generation system," Results in Engineering, vol. 20, p. 101466, 2023, doi: 10.1016/j.rineng.2023.101466.

[13] T. Bahi and A. Lakhdara, "Analysis of Genetic and Cuckoo Search Algorithms for MPPT in Partial Shaded," International Journal of Smart Grid-ijSmartGrid, vol. 8, no. 1, pp. 35-40, 2024, doi: 10.20508/ijsmartgrid.v8i1.329.g330.

[14] L. Van Dai, "A novel protection method to enhance the grid-connected capability of DFIG based on wind turbines," IETE Journal of Research, vol. 70, no. 2, pp. 2047-2063, 2024, doi: 10.1080/03772063.2022.2163925.

[15] B. M. Bellah, B. Tahar, and B. Adel, "Adaptive hybrid MPPT using artificial intelligence for an autonomous PV system," International Journal of Smart Grid-ijSmartGrid, vol. 8, no. 1, pp. 27-34, 2024, doi: 10.20508/ijsmartgrid.v8i1.328.g331.

[16] M. H. Zafar, N. M. Khan, A. F. Mirza, and M. Mansoor, "Bio-inspired optimization algorithms based maximum power point tracking technique for photovoltaic systems under partial shading and complex

partial shading conditions," Journal of Cleaner Production, vol. 309, p. 127279, 2021, doi: https://doi.org/10.1016/j.jclepro.2021.127279.

[17] M. Uoya and H. Koizumi, "A calculation method of photovoltaic array's operating point for MPPT evaluation based on one-dimensional Newton–Raphson method," IEEE Transactions on Industry Applications, vol. 51, no. 1, pp. 567-575, 2014, doi: 10.1109/tia.2014.2326083.

[18] M. A. Kamarposhti, I. Colak, H. Shokouhandeh, C. Iwendi, S. Padmanaban, and S. S. Band, "Optimum operation management of microgrids with cost and environment pollution reduction approach considering uncertainty using multi-objective NSGAII algorithm," IET Renewable Power Generation, vol. 19, no. 1, p. e12579, 2025, doi: 10.1049/rpg2.12579.

[19] F. M. Makahleh, A. Amer, A.A. Manasrah, H. Attar, A.A. Solyman, M.A. Kamarposhti, and P. Thounthong, "Optimal management of energy storage systems for peak shaving in a smart grid," Computers, Materials and Continua, vol. 75, no. 2, pp. 3317-3337, 2023, doi: 10.32604/cmc.2023.035690.

[20] N. D. Hung, "Voltage Stability Improvement of Synchronous Generator by Using AVR Self Turning Based on the Adaptive Fuzzy-PID Controller," International Journal of Intelligent Engineering & Systems, vol. 15, no. 6, 2022, doi: 10.22266/ijies2022.1231.42

[21] M. Ahmadi Kamarposhti, H. Shokouhandeh, Y. Gholami Omali, I. Colak, P. Thounthong, and W. Holderbaum, "Optimal coordination of TCSC and PSS2B controllers in electric power systems using MOPSO multiobjective algorithm," International Transactions on Electrical Energy Systems, vol. 2022, no. 1, p. 5233620, 2022, doi: 10.1155/2022/5233620.

[22] I. A. Joneidi, M. A. Kamarposhti, A. A. Shayegani Akmal, and H. Mohseni, "Leakage current analysis, FFT calculation and electric field distribution under water droplet on polluted silicon rubber insulator," Electrical Engineering, vol. 95, no. 4, pp. 315-323, 2013, doi: 10.1007/s00202-012-0260-8.

[23] M. Killi and S. Samanta, "Modified perturb and observe MPPT algorithm for drift avoidance in photovoltaic systems," IEEE transactions on Industrial Electronics, vol. 62, no. 9, pp. 5549-5559, 2015, doi: 10.1109/tie.2015.2407854.

[24] L. Shang, H. Guo, and W. Zhu, "An improved MPPT control strategy based on incremental conductance algorithm," Protection and Control of Modern Power Systems, vol. 5, no. 2, pp. 1-8, 2020, doi: 10.1186/s41601-020-00161-z.

[25] Y. Xiao, Y. Zhao, Z. Shen, and H. Jiao, "SMGSA algorithm-based MPPT control strategy," Journal of Power Electronics, vol. 24, no. 5, pp. 789-798, 2024, doi: 10.1007/s43236-023-00757-2.

[26] D. Van Hoa, H. H. Bao Nghia, and L. Van Dai, "Optimizing permanent magnet synchronous motor control: a comparative study of MPCC-based techniques," Eastern-European Journal of Enterprise Technologies, vol. 135, no. 2, 2025, doi: 10.15587/1729-4061.2025.331895.

[27] L. Wang, H. Liu, L. V. Dai, and Y. Liu, "Novel method for identifying fault location of mixed lines," Energies, vol. 11, no. 6, p. 1529, 2018, doi: 10.3390/en11061529.

[28] X. Liu and Y. Wang, "Reconfiguration method to extract more power from partially shaded photovoltaic arrays with series-parallel topology," Energies, vol. 12, no. 8, p. 1439, 2019, doi: 10.3390/en12081439.

[29] M. Alkahtani, Z. Wu, C. S. Kuka, M. S. Alahammad, and K. Ni, "A Novel PV array reconfiguration algorithm approach to optimising power generation across non-uniformly aged PV arrays by merely repositioning," J, vol. 3, no. 1, p. 5, 2020, doi: 10.3390/j3010005.

[30] A. Belkaid, S. HADJI, and L. Larbi, "Modified Topology of SEPIC Converter with High Gain Transfer Ratio for PV Applications," International Journal of Smart Grid-ijSmartGrid, vol. 8, no. 4, pp. 199-204, 2024, doi: 10.20508/ijsmartgrid.v8i4.363.g368.

[31] B. Dhouib, M. A. Zdiri, Z. Alaas, and H. Hadj Abdallah, "Fault analysis of a small PV/wind farm hybrid system connected to the grid," Applied Sciences, vol. 13, no. 3, p. 1743, 2023, doi: 10.3390/app13031743.

[32] D. Nishad, A. Tiwari, S. Khalid, S. Gupta, and A. Shukla, "AI-based hybrid power quality control system for electrical railway using single phase PV-UPQC with Lyapunov optimization," Scientific Reports, vol. 15, no. 1, p. 2641, 2025, doi: 10.1038/s41598-025-85393-5.

[33] C. D. Loi, H. H. B. Nghia, V. T. K. Nhi, B. T. Quy, and L. Van Dai, "Advanced Speed and Torque Control for PMSM via Adaptive PID and Higher-Order Sliding Mode," International Journal of Intelligent Engineering & Systems, vol. 18, no. 3, 2025, doi: 10.22266/ijies2025.0430.44.

[34] K. Moloi, N. W. Ndlela, and I. E. Davidson, "Fault classification and localization scheme for power distribution network," Applied Sciences, vol. 12, no. 23, p. 11903, 2022, doi: 10.3390/app122311903.

International Journal of Smart Grid (IJSmartGrid)
https://www.ijsmartgrid.org/ Online ISSN: 2602-439X
A. Berrim et al., Vol. 10, No. 1, March, 2026 Research Article

Enhancing Power Quality in Grid- Connected PV Systems Using New Integral Backstepping Control Validated via PIL Co-Simulation

Ali Berrim*, Moussaoui Abdelkrim*, Zellouma Laid **, Houssam Eddine Ghadbane*‡, Habib Benbouhenni ***

*Laboratoire de Génie Électrique de Guelma (LGEG), Université 8 Mai 1945, Guelma 24000, Algeria.

**LEVRES Laboratory, Department of Electrical Engineering, University of El Oued, 39000, Algeria.

*** Department of Electrical Engineering, Faculty of Technology, Hassiba Benbouali University of Chlef, B.P 78C Ouled Fares, Chlef 02180, Algeria

(berrim.ali@univ-guelma.dz, moussaoui.abdelkrim@univ-guelma.dz, Zellouma13@yahoo.fr, ghadbane.houssameddine@univ-guelma.dz, habib0264@gmail.com)

‡Corresponding Author;24000, Tel:+213 657155158,

ghadbane.houssameddine@univ-guelma.dz

Received: 25.07.2025 Accepted: 10.12.2025

Abstract- In the context of the growing global demand for clean and sustainable energy, advanced control strategies for renewable energy systems play a crucial role in improving efficiency, reliability, and grid integration. This paper addresses these challenges by proposing a novel nonlinear integral backstepping control (NIBC) approach for a grid-connected photovoltaic (PV) system with dual functionality. The proposed control scheme is designed to regulate the maximum power point (MPP), current, and DC-link voltage loops, ensuring a stable DC bus voltage while enabling continuous and optimal energy extraction from the PV array. By incorporating power exchange rules with the utility grid into the energy management strategy, effective DC bus voltage regulation is achieved under varying operating conditions. The proposed approach enhances grid power quality by maintaining low harmonic distortion, fast dynamic response, high power factor, and strong robustness, even in the presence of nonlinear loads. Furthermore, the system's performance is evaluated under fluctuating solar irradiation to demonstrate the effectiveness and resilience of the control strategy. To validate its practical feasibility, a Processor-in-the-Loop (PIL) co-simulation using a C2000 LaunchXL-F28379D digital signal processing (DSP) platform is conducted, highlighting the potential of the proposed method to support the reliable and efficient integration of renewable energy sources into modern power grids.

Keywords Grid connected photovoltaic system, double function, nonlinear integral backstepping controller.

1. Introduction

In recent years, the increasing need for electrical energy has put significant amounts of pressure on traditional methods to generate energy, which predominantly rely on fossil fuels such as coal, diesel, and natural gas. These conventional sources, while widely used, are increasingly being recognized for their high costs, inefficiency, and, more critically, their adverse environmental impact. The environmental consequences of continued reliance on such

Cite this article as: A. Berrim, M. Abdelkrim, Z. Laid, H.E. Ghadbane, and H. Benbouhenni, "Enhancing Power Quality in Grid-Connected PV Systems Using New Integral Backstepping Control Validated via PIL Co-Simulation" *International Journal of Smart Grid (ijSmartGrid)*, Vol. 10, No. 1, pp. 48-59, March, 2026.

energy sources, notably the emission of greenhouse gases, exacerbate global warming and climate change. As the world grapples with these challenges, the focus has shifted toward sustainable and renewable energy sources that not only address the rising energy demands but also minimize environmental harm [1-5]. Among the renewable energy technologies, photovoltaic (PV) systems stand out due to their cost-effectiveness, ease of implementation, and environmental benefits [6-8]. PV systems harness solar energy and convert it directly into electricity, offering a pollution-free and sustainable solution for energy generation. The integration of PV systems into the electrical grid, however, introduces several power quality issues, particularly due to the nonlinear characteristics of loads connected to the grid. These issues, including harmonic distortions, reactive power, and fluctuations in active power, can severely affect grid stability and efficiency [9-13].

Various maximum power point tracking (MPPT) techniques have been created because of the nonlinear power-voltage properties of PV panels, from basic extremum-seeking algorithms like Perturb and Observe (P&O) to more sophisticated controllers like as sliding mode controllers (SMC), proportional integral (PI) controller, adaptive controls, neural networks (NN), and fuzzy logic [14-17]. Often, without needing a thorough mathematical model of the PV system, these sophisticated techniques provide greater efficiency and durability. To get the best outcomes, however, they rely heavily on expertise and trial adjustment.

Heuristic global optimisation methods like particle swarm optimisation (PSO) and genetic algorithms (GA) are more efficient for complicated situations like partial shading, guaranteeing convergence to the global maximum power point [18]. Often implemented and validated via MATLAB simulations, other sophisticated nonlinear control techniques—including third-order SMC technique, nonlinear backstepping control (NBC), and their combinations—have been suggested to enhance robustness, dynamic response, and power quality [19].

Despite the advances, challenges remain, such as control complexity, dependency on accurate system modeling, tuning difficulties due to numerous gains, and the presence of steady-state errors (SSEs). To overcome these, integral actions and hybrid control strategies are integrated into controllers, though at the expense of increased implementation complexity.

Shunt active power filter (SAPF) has become crucial for harmonic correction as nonlinear loads impairing power quality are increasingly used; they operate in parallel with the grid to preserve sinusoidal source currents [20-22]. Usually, control techniques for PV-based SAPFs include voltage-oriented control (VOC) and direct power control (DPC), each having its own benefits and trade-offs regarding complexity, dynamic responsiveness, and sensitivity to parameter changes [23]. Improvements, such as space vector pulse width modulations (SV-PWM), have been created to stabilise switching frequencies and enhance general system performance [24].

This paper uses backstepping control to govern the DC-DC boost converter and hence maximise the power drawn from the PV generator. The reference value for the duty cycle of the DC-DC converter is given by two nonlinear integral backstepping controls (NIBCs) controlling the voltage and current of the PV generator. Moreover, backstepping control is used to manage the harmonic currents of the parallel active power filter (PAPF) and also the DC link capacitor voltage. Using the extracted solar power, the control approach for the PV-PAPF system is designed to meet the load requirements. Thus, taking into account the nonlinear load's reactive power consumption and power factor. We used PIL co-simulation to assess the system's operation. The results demonstrate the overall effectiveness of the system.

2. System Description and Modeling

Fig. 1 illustrates the overall configuration and control scheme of the PV-SAPF system, divided into two main sections: the power section and the control section. The power section consists of a voltage source inverter (VSI), a capacitive energy storage circuit on the DC side, and an output filter on the AC side. The control section includes a method for identifying perturbed currents, a DC-link voltage regulator that manages the energy storage component, and a controller for the injected currents.

2.1. SAPF Modeling

In the a-b-c-phase reference frame, the following equations characterise the SAPF's behaviour:

$$\frac{d}{dt}\begin{bmatrix} i_{fa} \\ i_{fb} \\ i_{fc} \end{bmatrix} = -\frac{1}{L_f}\begin{bmatrix} R_f & 0 & 0 \\ 0 & R_f & 0 \\ 0 & 0 & R_f \end{bmatrix}\begin{bmatrix} i_{fa} \\ i_{fb} \\ i_{fc} \end{bmatrix} - \begin{bmatrix} v_{fa} \\ v_{fb} \\ v_{fc} \end{bmatrix} + \begin{bmatrix} v_a \\ v_b \\ v_c \end{bmatrix}$$

$$\frac{dV_{dc}}{dt} = \frac{1}{C_{dc}}(S_a i_{fa} + S_b i_{fb} + S_c i_{fc}) \quad (1)$$

The AC side voltages and currents of the shunt active power filter are represented by $v_{fa,b,c}$ and $i_{fa,b,c}$, respectively. The common coupling voltage point is denoted by $v_{a,b,c}$. where L_f stands for the filter's output inductance and R_f for its resistance. The control signals for the voltage source inverter are denoted by $S_i, i = a, b, c$, and V_{dc} refers to the capacitor C_{dc} voltage.

In the synchronous reference frame, the mathematical model of the shunt active power filter is provided by:

$$\begin{cases} \frac{di_{fd}}{dt} = -\frac{1}{L_f}\left(R_f i_{fd} - v_{fd} + v_d\right) - L_f w.\, i_{fd} \\ \frac{di_{fq}}{dt} = -\frac{1}{L_f}\left(R_f i_{fq} - v_{fq} + v_q\right) - L_f w.\, i_{fq} \\ \frac{dV_{dc}}{dt} = \frac{1}{C_{dc}} i_{dc} \end{cases} \quad (2)$$

In the synchronous reference frame, $v_{fd,q}$ and $i_{fd,q}$ denote the SAPF voltages and currents, respectively, while v_d and v_q represent the voltages at the point of common coupling. Additionally, the current flowing through the capacitor C_{dc} is indicated.

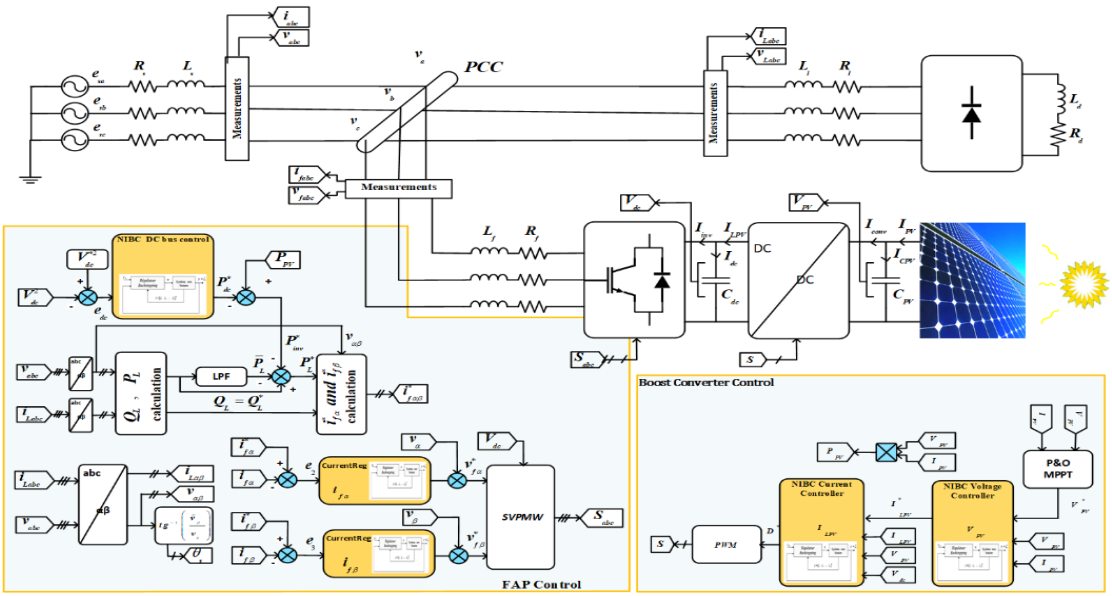

Fig. 1. The proposed control method block diagram.

3. NIBC for the PV- SAPF System

This section implements a backstepping control approach to regulate the DC-DC boost converter, with the objective of maximizing energy extraction from the PV source. Two NIBC controllers are employed to adjust the reference duty cycle of the converter by controlling both the voltage and current of the PV array. Additionally, backstepping techniques are utilized to manage the harmonic currents in the SAPF and to maintain the DC bus voltage.

Using the extracted solar power, adjusting for power factor, and the nonlinear load's reactive power consumption, the control strategy for the PV- SAPF system is meant to satisfy the load demand.

Figure 1 shows the control diagram in the stationary reference frame employing backstepping regulators for the PV-SAPF system.

3.1. *Control Strategy on the FAP Side*

The squared DC bus voltage $V_{dc}^2$and its reference V_{dc}^{2*} are compared in Figure 1. The result is used to feed the error to a backstepping controller. The reference active power $P_{dc}^*$is supplied by the voltage controller's output. Based on instantaneous p-q theory, the compensation powers are computed. To obtain the average powers, a 4th-order low-pass filter is applied. The oscillating powers are determined by subtracting these average values from the corresponding instantaneous active and reactive powers.

3.1.1. Design of the NIBC on the PAPF side

Here, the FAP controllers are synthesised using the backstepping control approach. A breakdown of the full FAP model forms the basis for the construction of the backstepping controllers. For this purpose, system (5) is partitioned into the following three phases:

- **Phase 1**

The derivative of the DC bus voltage can be extracted from Equation (3).

$$\frac{dV_{dc}}{dt} = \frac{P_{dc}}{V_{dc}C_{dc}} \tag{3}$$

In this phase, described by Equation (3), the voltage $V_{dc}$is the output variable, the control variable is the instantaneous active power P_{dc}^*.

- **Phase 2**

The voltage $v_{f\alpha}^*$ in the second stage defined by Equation (4) is selected as the control variable; the current $i_{f\alpha}$ is seen as the output variable.

$$\frac{di_{f\alpha}}{dt} = -\frac{R_f}{L_f}i_{f\alpha} + \frac{v_{f\alpha}^*}{L_f} - \frac{\hat{v}_\alpha}{L_f} \tag{4}$$

- **Phase 3**

In this phase, the control and output variables are respectively represented as $v_{f\beta}^*$ and $i_{f\beta}$:

$$\frac{di_{f\beta}}{dt} = -\frac{R_f}{L_f}i_{f\beta} + \frac{v_{f\beta}^*}{L_f} - \frac{\hat{v}_\beta}{L_f} \tag{5}$$

3.1.2. Design of the NIBC DC bus voltage

The DC bus voltage is controlled to a reference value using a backstepping controller so that it remains at a desired constant value, while compensating for inverter losses.

The tracking error variable z_1 is defined as follows, as this control aims to establish the power reference at the terminals of the DC bus capacitor.

$$z_1 = V_{dc}^* - V_{dc} \tag{6}$$

The first phase provides the error z_1 dynamics as follows:

$$\dot{z}_1 = \dot{V}_{dc}^* - \dot{V}_{dc} = \dot{V}_{dc}^* - \frac{P_{dc}^*}{V_{dc}C_{dc}} \tag{7}$$

We select the Lyapunov candidate function as:

$$V_1 = \frac{1}{2}z_1^2 \tag{8}$$

Function (8) derivative is given by:

$$\dot{V}_1 = z_1\left(\dot{V}_{dc}^* - \frac{P_{dc}^*}{V_{dc}C_{dc}}\right) \tag{9}$$

A negative derivative of the Lyapunov function is required to guarantee system stability. Picking the derivative z_1 of as follows will do this:

$$\dot{z}_1 = -k_1 z_1 \tag{10}$$

Where k_1 represents a gain positive.

Accordingly, the control law is expressed in Equation (11), and its corresponding control structure is illustrated in Fig. 2.

$$P_{dc}^* = V_{dc}C_{dc}\left(\dot{V}_{dc}^* + k_1 z_1\right) \tag{11}$$

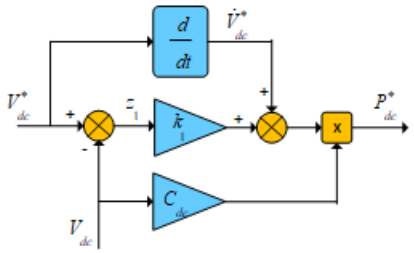

Fig. 2. Control schematic for DC bus voltage regulation.

3.1.3. Synthesis of the NIBC current $i_{f\alpha}$ regulator

The following analysis focuses on the design of the current $i_{f\alpha}$ NIBC controller, formulated from the second part of Equation (1).

The tracking error variable z_2 is expressed as:

$$z_2 = i_{f\alpha}^* - i_{f\alpha} \tag{12}$$

The error z_2's dynamic is defined as:

$$\dot{z}_2 = i_{f\alpha}^* - \left(-\frac{R_f}{L_f}i_{f\alpha} + \frac{v_{f\alpha}^*}{L_f} - \frac{\hat{v}_\alpha}{L_f}\right) \tag{13}$$

It is decided that the Lyapunov candidate function will be:

$$V_2 = \frac{1}{2}z_2^2 \tag{14}$$

The function's derivative Equation (14) is stated as:

$$\dot{V}_2 = z_2\left(i_{f\alpha}^* - \left(-\frac{R_f}{L_f}i_{f\alpha} + \frac{v_{f\alpha}^*}{L_f} - \frac{\hat{v}_\alpha}{L_f}\right)\right) \tag{15}$$

Choosing the derivative z_2 of as guarantees system stability:

$$\dot{z}_2 = -k_2 z_2 \tag{16}$$

Where $k_2$is a gain positive.

Thus, the resulting regulation rule is defined by Equation (17), and its associated schematic is depicted in Fig. 3.

$$v_{f\alpha}^* = L_f i_{f\alpha}^* + L_f k_2 z_2 + R_f i_{f\alpha} + \hat{v}_\alpha \tag{17}$$

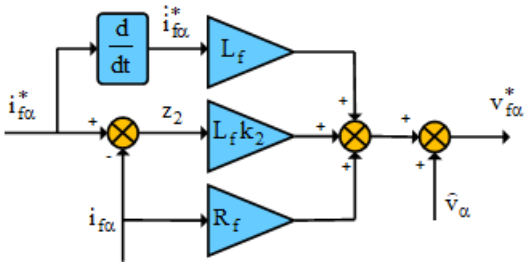

Fig. 3. Schematic of the NIBC control of current $i_{f\alpha}$

3.1.4. Design of the NIBC for current $i_{f\beta}$

The NIBC's design for current $i_{f\beta}$, defined by the third phase specified by Equation (5), is examined as follows:

The tracking error variablez_3 is structured as follows:

$$z_3 = i_{f\beta}^* - i_{f\beta} \tag{18}$$

The error dynamics $z_3$are supplied by:

$$\dot{z}_3 = i_{f\beta}^* - \left(-\frac{R_f}{L_f}i_{f\beta} + \frac{v_{f\beta}^*}{L_f} - \frac{\hat{v}_\beta}{L_f}\right) \tag{19}$$

It is decided that the candidate function of Lyapunov will be:

$$V_3 = \frac{1}{2}z_3^2 \tag{20}$$

There is a function (20) whose derivative is:

$$\dot{V}_3 = z_3\left(i_{f\beta}^* - \left(-\frac{R_f}{L_f}i_{f\beta} + \frac{v_{f\beta}^*}{L_f} - \frac{\hat{v}_\beta}{L_f}\right)\right) \tag{21}$$

System stability is ensured when the Lyapunov function's derivative is negative; Guaranteeing system stability is as simple as selecting the derivative z_3 of as:

$$\dot{z}_3 = -k_3 z_3 \tag{22}$$

Wherek_3 presents a gain positive.

Equation (23) gives the resulting control law, and Fig. 4. shows its block diagram.

$$v_{f\beta}^* = L_f i_{f\beta}^* + L_f k_3 z_3 + R_f i_{f\beta} + \hat{v}_\beta \tag{23}$$

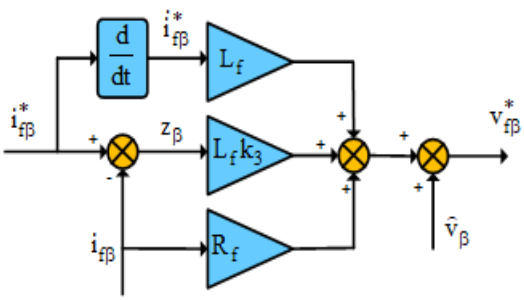

Fig. 4. Schematic of the NIBC of current $i_{f\beta}$

3.2. NIBC on the Boost Converter Side

The DC-DC converter is governed using a backstepping control strategy to ensure optimal energy harvesting from the PV source. The PV generator's output voltage and current are controlled by two NIBCs in the control system shown in Fig. 5. To accomplish voltage control, the MPPT algorithm supplies a reference value V_{pv}^* and uses it to regulate the PV generator voltage V_{pv}. The reference current for internal current regulation, the reference value I_{Lpv}^* is computed by integrating the voltage controller's output with a correction factor linked to the PV current.

In addition, as seen in Fig. 5, the DC/DC converter's duty cycle reference D^* is determined using the output of the current controller with compensation.

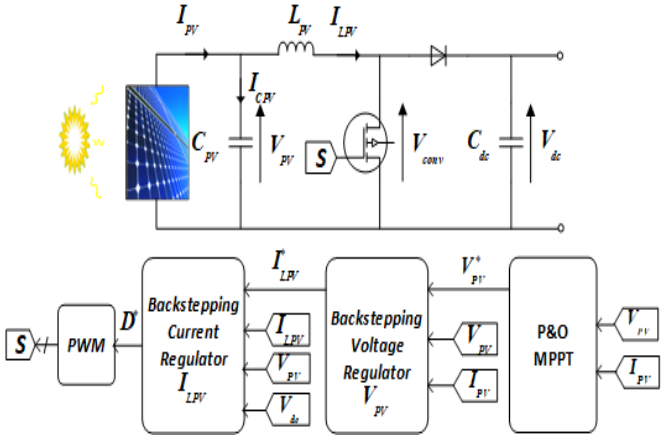

Fig. 5. Schematic of DC-DC converter NIBC.

Following the division of the global model provided by Equation (20) into two parts, the following NIBC controllers are utilised for the control of the system on the DC-DC converter side:

- **Part 1**

$$\frac{dV_{PV}}{dt} = \frac{1}{C_{PV}} I_{PV} - \frac{1}{C_{PV}} I_{LPV} \tag{24}$$

In this initial part of the control scheme, the current I_{LPV} is regarded as the fluctuating control input, and the corresponding output is the voltage produced $V_{PV}$by the PV generator.

- **Part 2**

The PV current $I_{LPV}$is the output variable in the second subsystem described by Equation (25), while the duty cycle D is the control variable.

$$\frac{dI_{LPV}}{dt} = \frac{1}{L_{PV}} V_{PV} - \frac{1}{L_{PV}} (1 - D) V_{dc} \tag{25}$$

3.2.1. Design of the NIBC voltage regulator

The synthesis of the voltage V_{PV} regulator utilising the backstepping technique, as shown by the first subsystem specified by Equation (24), is examined in this manner:

The tracking error variable $z_{Vpv}$is given by

$$z_{Vpv} = V_{PV}^* - V_{PV} \tag{26}$$

The dynamics of errors $z_{Vpv}$are supplied by:

$$\dot{z}_{Vpv} = \dot{V}_{PV}^* - \left(\frac{1}{C_{PV}} I_{PV} - \frac{1}{C_{PV}} I_{LPV}^*\right) \tag{27}$$

We select the candidate Lyapunov function as:

$$V_{Vpv} = \frac{1}{2} z_{Vpv}^2 \tag{28}$$

The function's (28) derivative is:

$$\dot{V}_{Vpv} = z_{Vpv}\left(\dot{V}_{PV}^* - \left(\frac{1}{C_{PV}} I_{PV} - \frac{1}{C_{PV}} I_{LPV}^*\right)\right) \tag{29}$$

Choosing the derivative z_{Vpv} of as follows will help to guarantee system stability: the Lyapunov function's derivative is negative.

$$\dot{z}_{Vpv} = -k_{Vpv} z_{Vpv} \tag{30}$$

Where k_{Vpv} is a gain positive.

Consequently, Equation (31) can be used to calculate the reference current. Fig. 6 shows its control schematic.

$$I_{LPV}^* = C_{PV} \dot{V}_{PV}^* - I_{PV} - k_{Vpv} C_{PV} (V_{PV}^* - V_{PV}) \tag{31}$$

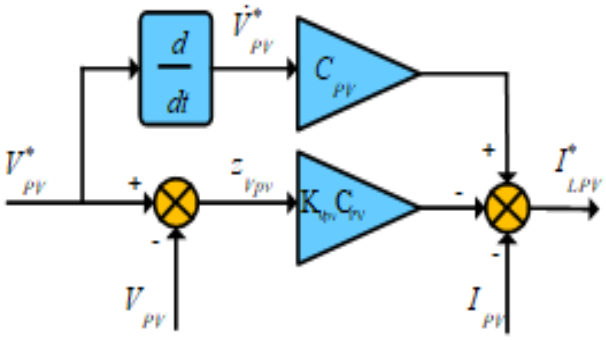

Fig. 6. Schematic of the NIBC of the voltage V_{PV}

3.2.2. Synthesis of the NIBC current regulator I_{LPV}

This is investigated by synthesising the required current regulation I_{LPV}PV using the second part defined by Equation (25).

The tracking error variable $z_{ILpv}$is defined as:

$$z_{ILpv} = I^*_{LPV} - I_{LPV} \tag{32}$$

The dynamics of the error z_{ILpv} is examined in this manner:

$$\dot{z}_{ILpv} = \dot{I}^*_{PV} - \left(\frac{1}{L_{PV}} V_{PV} - \frac{1}{L_{PV}}(1 - D^*)V_{dc}\right) \tag{33}$$

We select the candidate Lyapunov function as:

$$V_{ILpv} = \frac{1}{2} z^2_{ILpv} \tag{34}$$

The function's derivative Equation (34) is:

$$\dot{V}_2 = z_{ILpv}\left(\dot{I}^*_{PV} - \left(\frac{1}{L_{PV}} V_{PV} - \frac{1}{L_{PV}}(1 - D^*)V_{dc}\right)\right) \tag{35}$$

Choosing the derivative z_{ILpv} of as follows guarantees system stability:

$$\dot{z}_{ILpv} = -k_{ILpv} z_{ILpv} \tag{36}$$

Where k_{ILpv}denotes a gain positive.

Consequently, the duty cycle D^* may be computed via Equation (37). Fig. 7 illustrates the relevant control block diagram.

$$D^* = \frac{1}{V_{dc}}\left(L_{PV}\dot{I}^*_{LPV} - V_{PV} + V_{dc} + L_{PV} k_{ILpv} z_{ILpv}\right) \tag{37}$$

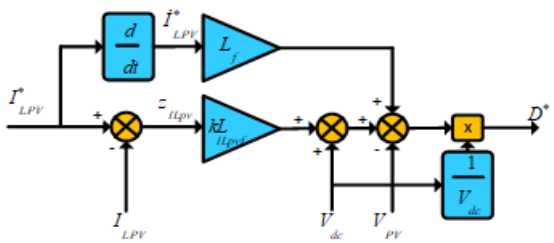

Fig. 7. Schematic of the NIBC control of the current I_{LPV}

4. The PIL Technique for Implementing Control Strategy

By immediately running the produced code on an embedded CPU in a real-time setting, the PIL test allows the validation and testing of regulation techniques, and it is a co-simulation approach. Here, we put the control algorithms through their paces in a real-world setting by simulating PIL operations on a C2000 LaunchXL-F28379D DSP board. Fig. 8 depicts the simulation setup, where the physical system model is executed on a host computer and constantly communicates with the embedded control algorithm running on the DSP board. In this configuration, important metrics like memory utilisation, code speed, and execution time may be optimised for a thorough evaluation of the system's behaviour [25–30].

To evaluate the real-time performance of the proposed diagnostic system, a PIL test was conducted. The system operated with a simulation time step of 1 ms, maintaining an average CPU load of 35 % (with peaks up to 55 %), and required approximately 120 kB of RAM and 450 kB of Flash memory. The measured host–target latency was around 250 µs, confirming the computational efficiency and suitability of the approach for real-time implementation.

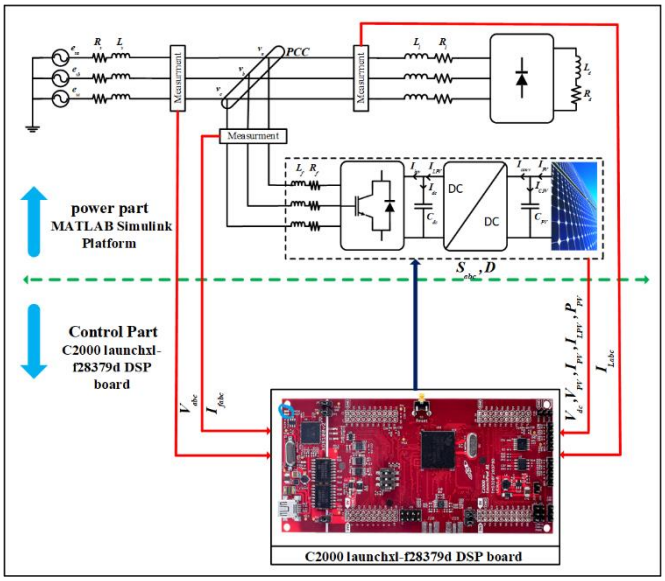

Fig. 8. Scheme of PIL.

5. Co-simulation Results and Discussion

The co-simulation of the PV-SAPF system controlled using the NIBC technique was carried out with the same parameters and under the same conditions mentioned earlier. The parameters of the BC controllers used are given in Table 1.

Table 1. Parameters of the BC-VOC-SVM controllers of the PV-SAPF system

SAPF Side	
DC bus voltage reference V_{dc}^{*}	700 V
DC-link capacitor C_{dc}	5 mF
Filter impedance R_f,L_f	1 mΩ, 350 µH
grid impedance R_l, L_l	2.7 mΩ, 26 µH
NIBC controller parameter for the DC bus voltage k_1	180
Parameters of the current $i_{f\alpha\beta}$controllerk_2, k_3	$5e^9$
Fundamental frequency f	50 Hz
switching frequencyf_{sw}	35 kHz
PV side	
Inductance L_{PV}	5 mH
Capacitance C_{PV}	55 mH
NIBC voltage V_{PV} controller parameter k_{Vpv}	$11010e^3$
NIBC current I_{LPV}controller parameterk_{ILpv}	$2e^3$

5.1. Variation in Solar Irradiance

Figs. 9 and 10 below show the results of the system's response to a change in solar irradiation under NIBC technique.

Fig. 9a shows the DC bus voltage waveform, which remains well-regulated at its reference value even during variations in solar irradiance. Fig. 9b displays the voltage and current waveforms of one grid phase, showing that they are in phase. The variation in the amplitude of source currents indicates the power level supplied or absorbed by the grid, as shown in Fig. 9c.

Moreover, the source current THD for phase a, obtained through Fast Fourier Transform (FFT) analysis, is 2.06%, which is well below the IEEE 519 recommended limit of 5%, as illustrated in Fig. 9d. This confirms that the proposed system effectively mitigates harmonic distortion and ensures compliance with international power quality standards.

Fig. 10 shows the PV generator's output power profile. In Fig. 10a, the PV output power follows the applied irradiance profile accurately. As the irradiance level increases, the PV output power rises accordingly, and the MPP shifts to track the new operating conditions. The active power produced by the PV system closely matches the maximum power of the PV generator under standard test conditions. The proposed control method exhibits a fast dynamic response, with a convergence time of approximately 0.002 s, and a steady-state error of about 40 W between the generated and reference PV power. These results demonstrate the high tracking efficiency and superior performance of the proposed control.

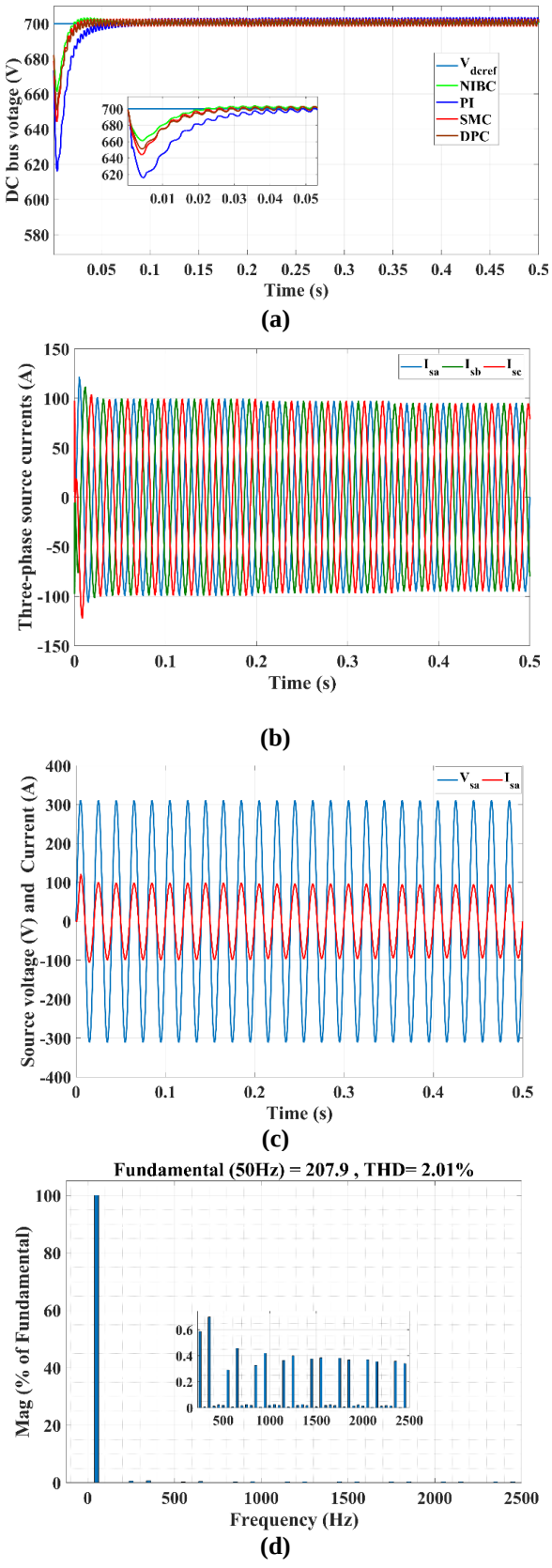

Fig. 9. Dynamic responses of the proposed system under changing solar irradiation (BC-VOC-SVM control): (a) the DC bus voltage V_{dc}, (b) a-b-c-phases currents of source I_{sabc} (c) Phase "a" of voltage $V_{sa}$and source current I_{sa}, and (d) Source current Harmonic spectrum.

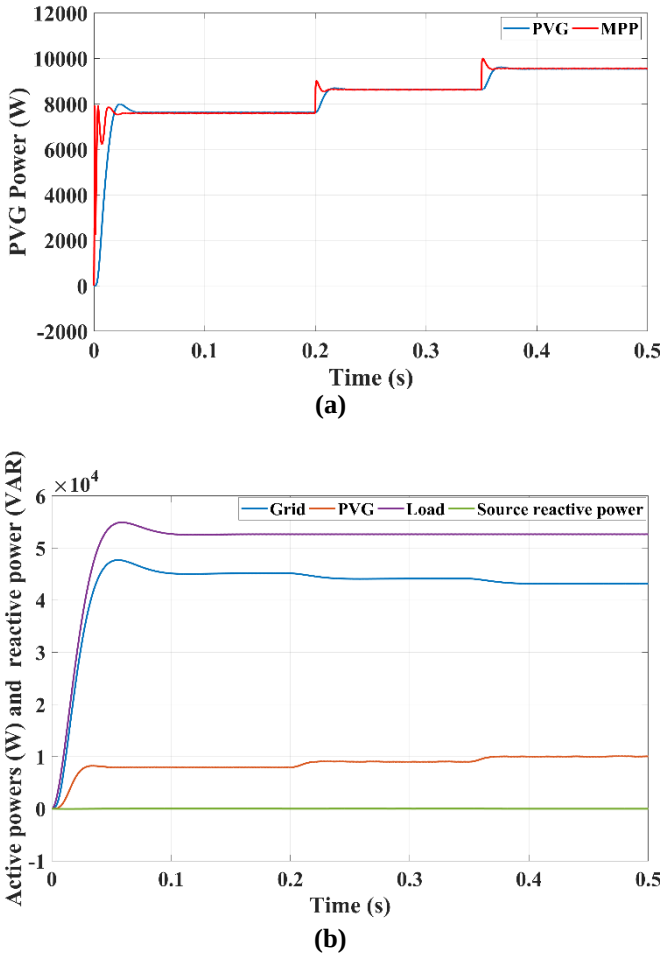

Fig. 10. Dynamic responses of the proposed system under changing solar irradiation (BC-VOC-SVM control): (a) GPV Power and its MPP, (b) Active powers of the grid P_s, the load P_L, and the VSI PF, Reactive powers of the grid Q_s, the load Q_L, and the VSI Q_F

5.2. Variation in Nonlinear Load

Figures 11 and 12 show the results of a nonlinear load variation under BC control of the PV-SAPF system.

The DC bus voltage remains stable at its reference value during abrupt changes in nonlinear load, as shown in Fig. 11a. Fig. 11b illustrates the grid phase current during load variation, showing that the sinusoidal shape of the current remains undistorted. This is reflected in the THD value, which is significantly reduced as shown in Fig. 11d. Fig. 11c also shows that the grid phase current remains in phase with its voltage during load changes, leading to a unity power factor on the grid side.

Fig. 12b shows the active power behavior: the inverter power always matches the PV generator power. As the load increases, grid power increases to compensate for the power shortfall from the PV generator. Meanwhile, the grid's reactive power remains zero. When the load's reactive power increases, the active filter provides the necessary reactive power in the opposite direction. Additionally, Fig. 12a shows that the PV generator's power continues to follow the irradiation profile, even when the load changes.

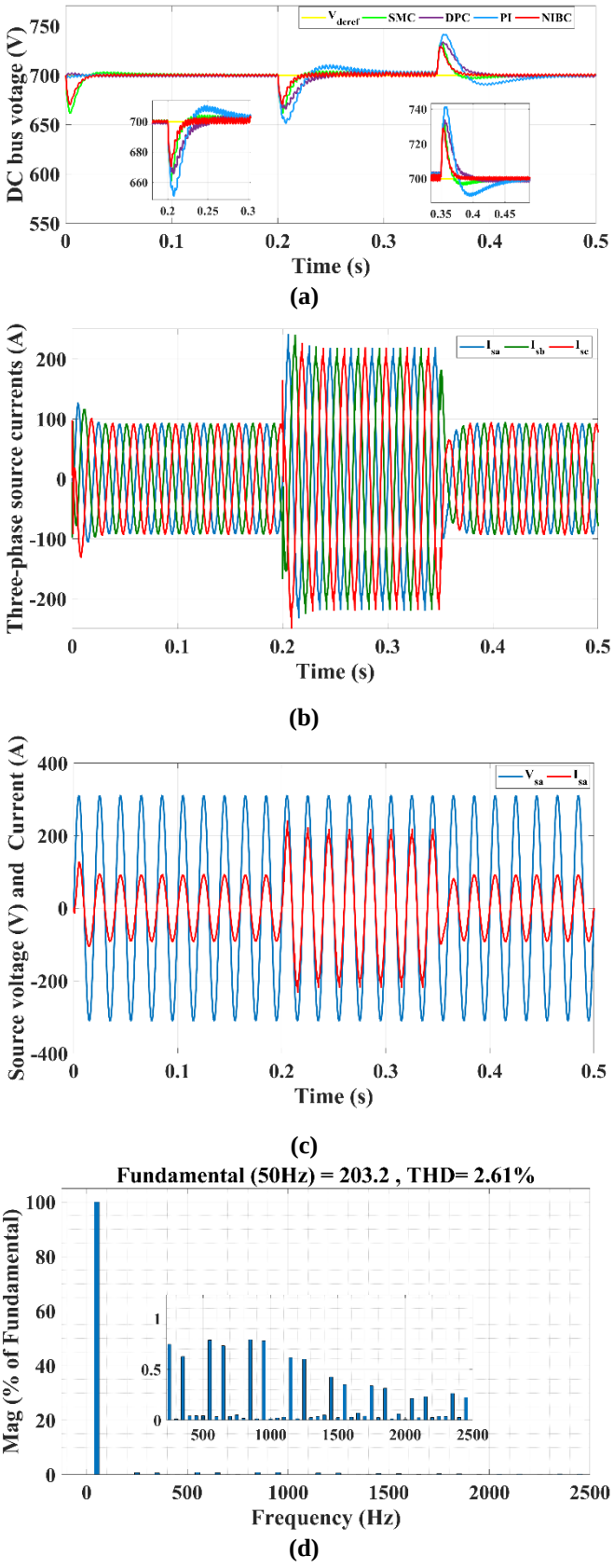

Fig. 11. Dynamic responses of the proposed system under changing solar irradiation (BC-VOC-SVM control): (a) the DC bus voltage V_{dc}, (b) a-b-c-phases currents of source I_{sabc} (c) Phase "a" of voltage V_{sa} and source current I_{sa}, and (d) Source current harmonic spectrum.

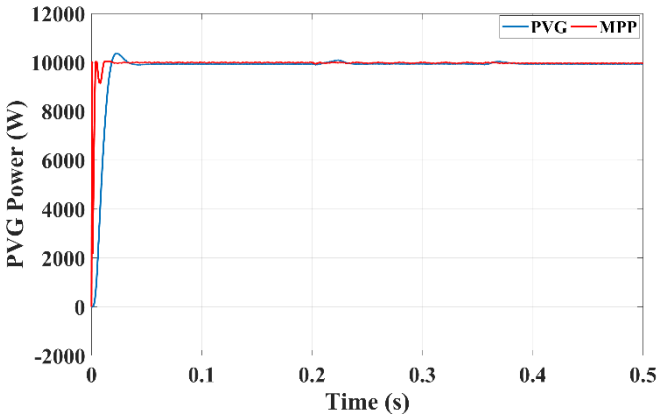

(a)

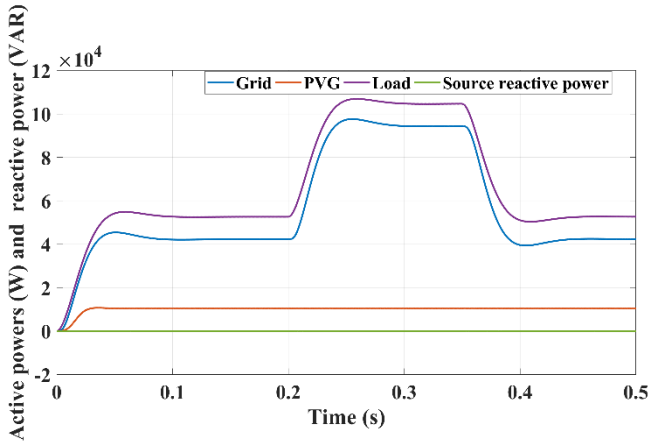

(b)

Fig. 12. System dynamic performance under nonlinear load disturbances with the proposed NIBC-VOC-SVM controller: (a) PVG power and its MPP and (b) Active powers of the grid P_s, the load P_L, and the VSI P_F, Reactive powers of the grid Q_s, the load Q_L, and the VSI Q_F

As seen in Table 2, the proposed NIBC controller achieves the lowest THD and fastest settling time, indicating superior dynamic and steady-state performance compared to other methods.

Table 2. Comparison between NIBC and conventional controllers under identical test conditions.

Controller	THD (%)	PF (%)	Overshoot (%)	Settling Time (ms)	Efficiency (%)
PI	3.5	92	7.14	14	89.35
SMC	3.75	89.5	5.46	6	94.784
DPC	3.18	95.3	4.43	7	96.383
NIBC (proposed)	**2.61**	**98.5**	**2.6**	**2.1**	**98.1**

5.3. Robustness Under Parameter Mismatch

Figs. 13 and 14 present the PIL validation results of the robustness test conducted to evaluate the system's performance under parameter uncertainties. The assessment considers deviations in the DC-link capacitor ($C = C_o$, $0.8\times C_o$, and $1.2\times C_o$) as depicted in Fig. 12, as well as variations in the filter inductance ($L = L_o$, $0.8\times L_o$, and $1.2\times L_o$) and resistance ($R = R_o$, $0.8\times$Ro, and $1.2\times R_o$), where C_o, L_o, and R_o denote the nominal parameters. The figure illustrates the DC-link voltage responses corresponding to a 700 V reference and the THD current under identical operating conditions to those described in Section 5.2.

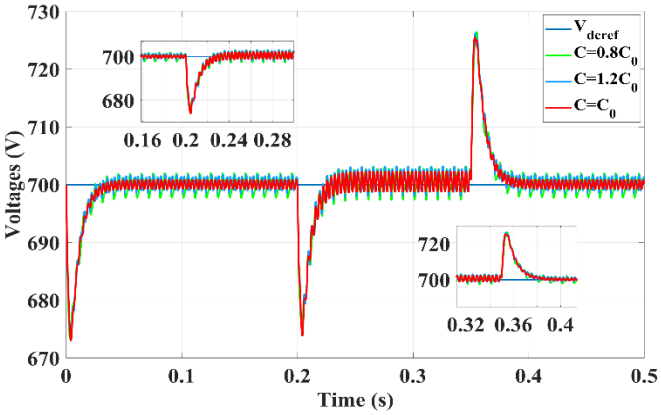

Fig. 13. DC-link voltage response under DC-link capacitor mismatch.

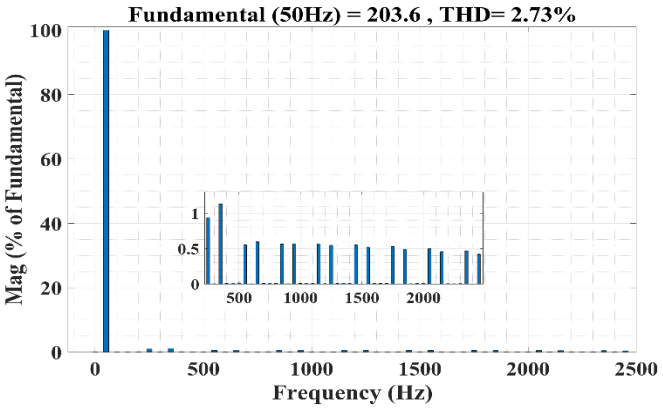

(a)

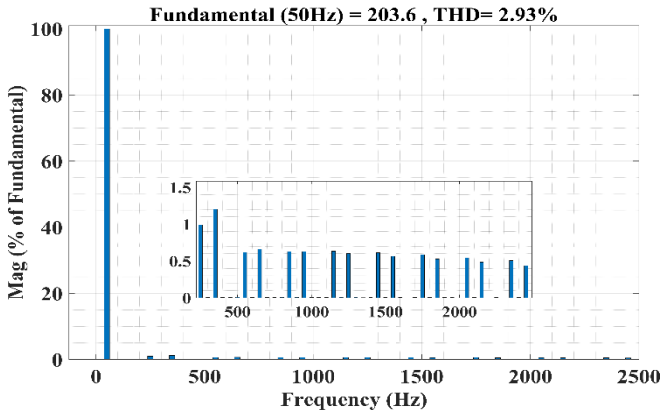

(b)

Fig. 14. Source current Harmonic spectrum response under filter inductance and resistance mismatch.

The obtained results confirm the remarkable robustness of the proposed control strategy, evidencing its strong

capability to accommodate parameter mismatches while maintaining stable operation and effective disturbance rejection throughout all operating scenarios.

5.4. Noise Assessment

To evaluate the robustness of the proposed NIBC technique against measurement noise, a simulation study was performed by introducing uniform random noise within the range of [-0.2 V, 0.2 V] to the measured DC microgrid voltage using the Uniform Random Number function. Fig.14 depicts the resulting DC microgrid voltage responses. Among the compared control methods—PI, SMC, and the proposed NIBC technique —the latter exhibits the best performance, showing a significant reduction in voltage drops and settling time while effectively suppressing measurement noise. Conversely, the conventional NIBC technique displays larger steady-state voltage ripples due to amplified noise effects. These results confirm that the proposed NIBC technique provides the most robust performance in mitigating measurement noise and rejecting external disturbances.

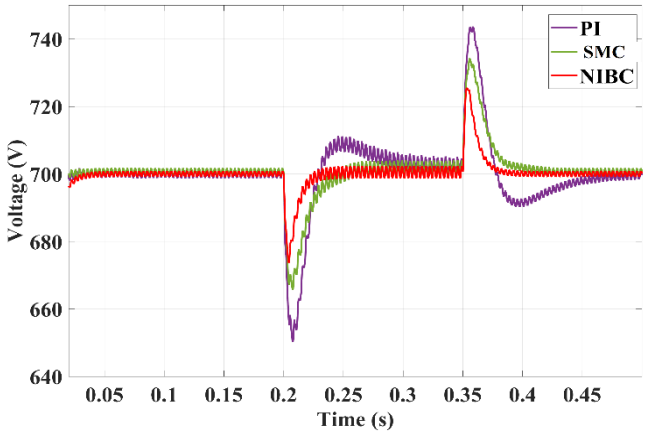

Fig. 15. DC-link voltage response with noise assessment.

6. Conclusions

This study presents an advanced control strategy for improving the performance and power quality of grid-connected PV systems, particularly in decentralized energy setups. The proposed approach integrates nonlinear ıntegral backstepping control with space vector pulse width modulation to optimize energy use, reduce SSEs, and enhance the control of key system parameters such as DC bus voltage, active and reactive power, and the maximum power point tracking process.

By utilizing a SAPF, the system ensures improved power quality, effectively minimizing THD values, maintaining a unity power factor, and achieving quick response times. This method also demonstrates strong resilience under varying solar conditions and load imbalances, with near-total elimination of steady-state faults. The system's stability and robustness have been validated through Lyapunov function analysis and Processor-in-the-Loop co-simulation results, confirming its ability to avoid overshooting and undershooting.

Overall, the integration of NIBC and SVPWM techniques enhances the efficiency, stability, and power quality of PV-micro grid-connected systems, making it a promising solution for modern smart grid applications.

In the future, the experimentally designed system will be implemented using real-world instruments, and the experimental results will be compared with other nonlinear strategies. Additionally, an attempt will be made to apply a fractional-order control strategy based on a neural algorithm to the NIBC approach in order to achieve high efficiency and superior operational performance for network-connected PV-micro systems.

Nomenclature

THD	Total harmonic distortion
PV	Photovoltaic system
PI	Proportional-integral controller
SMC	Sliding mode control
DPC	Direct power control
NIBC	Nonlinear ıntegral backstepping control
BC	Backstepping control
PVG	Photovoltaic generator
PIL	Processor-in-the-Loop
DSP	Digital Signal Processing
VSI	Voltage source inverter
VOC	Voltage-oriented control
MPP	Maximum power point
SSE	Steady-state error
SAPF	Shunt active power filter
P&O	Perturb and Observe
PAPF	Parallel active power filter
MPPT	Maximum power point tracking
SVPWM	Space vector pulse width modulation
NN	Neural network
PSO	Particle swarm optimisation
GA	Genetic algorithm

Acknowledgment

The authors would like to express their sincere appreciation to all contributors involved in this research. This work was conducted as part of a doctoral research project within the Electrical Engineering Laboratory of Guelma at the University of 8 May 1945, Guelma 24000. The authors gratefully acknowledge the academic environment, guidance, and support provided by the laboratory and the university, which greatly facilitated the completion of this study.

Author Contributions

Conceptualization, A. B., M. A., Z. L., and H. E. D.; methodology, A. B., M. A., Z. L., H.B. and H. E. D.; software, A. B., M. A., and Z.L.; validation, A. B., M. A., Z. L., and H. E. D.; formal analysis, A. B., M. A., Z. L., H. E. D., and H.B.; investigation, A. B., M. A., Z. L., and H.B., and H. E. D.; resources, A. B., M. A., H. B., Z. L., and H. E. D.; data curation, A. B., M. A., H. B., Z. L., and H. E. D.; writing-original draft preparation, A. B., M. A., Z. L., and H. E. D.; writing-review and editing, A. B., H. B., M. A., Z. L., and H. E. D.; visualization, A. B., H.B., M. A., Z. L., and H. E. D.; supervision, M. A., and H. E. D.; project administration, A.B., M.A., and H.B.;. All authors have read and agreed to the published version of the manuscript.

Conflict of interest

The author(s) declared no potential conflicts of interest with respect to the research, authorship, and/or publication of this article.

References

1. M. Osman and I. Qureshi, “Review of photovoltaic and concentrated solar technologies including their performance, reliability, efficiency and storage,” Results Eng., vol. 25, p. 104424, Mar. 2025, doi: 10.1016/J.RINENG.2025.104424.
2. S. M. Belhadj, B. Meliani, H. Benbouhenni, I. Colak, Z. M. S. Elbarbary and S. F. Al-Gahtani, "Control of three-level quadratic DC-DC boost converters for energy systems using various technique-based MPPT methods," Sci Rep vol. 15, pp. 14631, 2025. https://doi.org/10.1038/s41598-025-99551-2.
3. B. Maroua, Z. Laid, H. Benbouhenni, Z. M. S. Elbarbary, I. Colak, and M. M. Alammar "Genetic algorithm type 2 fuzzy logic controller of microgrid system with a fractional-order technique," Sci Rep vol. 15, pp. 6318, 2025. https://doi.org/10.1038/s41598-025-90239-1.
4. İ. F. Tepe, O. Taşdemir, and E. Irmak, “Design and Optimization of a Hybrid Energy Storage System Using the Dandelion Optimization Algorithm in Islanded Rural DC Microgrids,” 2025 13th International Conference on Smart Grid (icSmartGrid), pp. 249–257, May 2025, doi: 10.1109/icsmartgrid66138.2025.11071730.
5. M. N. Rahman, Md. S. Rahman, A. R. Rinatovich, M. M. Islam, V. Vavilov, and J. G. Singh, “Real-time energy management in microgrids using ARIMA Price forecasting and SLSQP optimization,” 13th International Conference on Smart Grid (icSmartGrid), pp. 310–316, May 2025, doi: 10.1109/icsmartgrid66138.2025.11071810.
6. H. Fatma-Zohra, D. Boukhetala, N. Debdouche, B. Habib, B. Jean-Pierre and L. Zarour, "Performance evaluation of nonlinear control approaches for grid-connected PV systems includes a novel fractional-order terminal-super twisting approach," Energy Reports, vol. 12, pp. 5024-5043, December 2024. https://doi.org/10.1016/j.egyr.2024.10.059.
7. Ch. Ali, D. Mabrouk, S. Ihammouchen, N. Bizon, B. Habib, K. Abdelhalim, R. Toufik, B. Mohamed-Fouad," An enhanced active disturbance rejection control scheme for DC voltage regulation in photovoltaic grid-connected four-leg inverter using a sliding mode observer," IEEE Access, vol. 13, pp. 18623-18643, 2025. doi: 10.1109/ACCESS.2025.3533015.
8. A. A. M. Faizal, N. Dwivedi, M. Sivasubramanian, S. Marisargunam, K. Rajesh, and N. Janaki, ‘Enhanced microgrid performance using coupled inductor switched Z-Source boost converter and GOA-tuned RBFNN MPPT,’ Int. J. Smart Grid - IjSmartGrid, vol. 9, no. 2, pp. 59–70, June 2025.
9. A. Boussafa, R. Rabeh, M. Ferfra, and K. Chennoufi, “Experimental test of optimizing maximum power point tracking performance in solar photovoltaic arrays based on backstepping control and optimized by genetic algorithm,” Results Eng., vol. 23, p. 102746, Sep. 2024, doi: 10.1016/J.RINENG.2024.102746.
10. L. El Oussoul, A. Elhamdaouy, and A. Ait Madi, “A new MPPT control strategy based on a weighting mechanism: Enhancing efficiency in solar energy harvesting,” Results Eng., vol. 26, p. 104725, Jun. 2025, doi: 10.1016/J.RINENG.2025.104725.
11. S. Akagi, S. Kaburagi, K. Ishibashi, K. Okumura, and R. Maeda, “Evaluation of the impact of uncertainty on reactive power reduction through fixed power factor adjustment of PV systems in medium-voltage distribution networks,” 2024 13th International Conference on Renewable Energy Research and Applications (ICRERA), pp. 612–616, Nov. 2024, doi: 10.1109/icrera62673.2024.10815182.
12. J. K. Sapawat and M. Miyatake, “Integration of solar PV with existing grid system to test a Ni-Cd battery set for railway applications,” 2024 13th International Conference on Renewable Energy Research and Applications (ICRERA), pp. 673–678, Nov. 2024, doi: 10.1109/icrera62673.2024.10815529.
13. S. Palavali and R. Kiranmayi, ‘PV model parameters extraction using opposition-based learning flow direction algorithm’, Int. J. Renew. Energy Res. IJRER, vol. 15, no. 3, pp. 488–502, Sept. 2025.
14. S. Akagi, S. Kaburagi, K. Ishibashi, K. Okumura, and R. Maeda, “Evaluation of the impact of uncertainty on reactive power reduction through fixed power factor adjustment of PV systems in medium-voltage distribution networks,” 2024 13th International Conference on Renewable Energy Research and Applications (ICRERA), pp. 612–616, Nov. 2024, doi: 10.1109/icrera62673.2024.10815182.
15. A. J. Alqattan, F. Albasri, and S. A. Al-Mosawi, ‘Modeling and assessment of D-STATCOM in grid connected PV system using ANN and ANFIS

controller', Int. J. Renew. Energy Res. IJRER, vol. 15, no. 3, pp. 525–536, Sept. 2025.

16. Y. Izgheche, T. Bahi, and A. Lakhdara, 'Analysis of genetic and cuckoo search algorithms for MPPT in partial shaded', Int. J. Smart Grid - IjSmartGrid, vol. 8, no. 1, pp. 35–40, Mar. 2024.
17. A. B. Djilali, E. Bounadja, A. Yahdou, H. Benbouhenni, Z. M. S. Elbarbary, I. Colak and S. F. Al-Gahtani, "Enhanced variable step sizes perturb and observe MPPT control to reduce energy loss in photovoltaic systems," Sci Rep. 15, pp. 11700, 2025. https://doi.org/10.1038/s41598-025-95309-y.
18. H. Renaudineau, F. Donatantonio, J.-P. Martin, S. Pierfederici, and F. Meibody-Tabar, "A PSO-based global MPPT technique for distributed PV power generation," IEEE Trans. Ind. Electron., vol. 62, no. 2, pp. 1047–1058, Feb. 2015, doi: 10.1109/TIE.2014.2336600.
19. A. B. Djilali, A. Yahdou, E. Bounadja, H. Benbouhenni, D. Zellouma, and I. Colak, "Energy management of the hybrid power system based on improved intelligent perturb and observe control using battery storage systems," Energy Reports, vol. 11, pp. 1611–1626, Jun. 2024, doi: 10.1016/J.EGYR.2024.01.010.
20. N. Debdouche, A. Chebabhi, B. Habib, F.-Z. Hadjaidji, Z. M. S. Elbarbary and S. F. Al-Gahtani, "Synergetic simplified super-twisting algorithm control for stability enhancement of PV/BESS-based DC microgrid," Scientific Reports, vol. 15, 7392, 2025. https://doi.org/10.1038/s41598-025-92042-4
21. K. Boutaghane, H. Benbouhenni, N. Bennecib, Z. M. S. Elbarbary, I. Colak, and M. M. Alammar, "Using new control strategies to improve the effectiveness and efficiency of the hybrid power system based on the battery storage system," Sci Rep vol. 15, pp. 4730, 2025. https://doi.org/10.1038/s41598-025-88804-9
22. Kh. N. Khallouf, Z. Laid, B. Habib, N. Debdouche, Z.M.S. Elbarbary, "Adaptive fuzzy logic control for microgrid-connected hybrid photovoltaic/wind generation systems," Energy Reports, vol. 12, pp. 4741-4756, Dec 2024. https://doi.org/10.1016/j.egyr.2024.10.042.
23. J. Y. Lee, R. Verayiah, K. H. Ong, A. Ramasamy, and M. B. Marsadek, "Voltage oriented control and direct power control strategies in solving under and overvoltage conditions for heavy load application on Malaysian distribution representative network," Electr. Eng., vol. 103, no. 3, pp. 1597–1612, Jun. 2021, doi: 10.1007/S00202-020-01143-Y/METRICS.
24. Y. Zhang, J. Liu, H. Yang, and J. Gao, "Direct power control of pulsewidth modulated rectifiers without DC voltage oscillations under unbalanced grid conditions," IEEE Trans. Ind. Electron., vol. 65, no. 10, pp. 7900–7910, Oct. 2018, doi: 10.1109/TIE.2018.2807421.
25. H. E. Ghadbane, S. Barkat, A. Houari, A. Djerioui, H. Rezk, and M. Louzazni, "Optimal adaptive fractional order integral sliding mode controller-energy management strategy for electric vehicles based on bald eagle search algorithm," Int. J. Energy Res., vol. 2024, 2024, doi: 10.1155/2024/7844084.
26. T. Kamel, D. Abdelkader, B. Said, S. Padmanaban, and A. Iqbal, "Extended Kalman Filter based sliding mode control of parallel-connected two five-phase PMSM drive system," Electron. 2018, Vol. 7, Page 14, vol. 7, no. 2, p. 14, Jan. 2018, doi: 10.3390/ELECTRONICS7020014.
27. H. E. Ghadbane, S. Barkat, A. Djerioui, A. Houari, M. Oproescu, and N. Bizon, "Energy management of electric vehicle using a new strategy based on slap swarm optimization and differential flatness control," Sci. Reports 2024 141, vol. 14, no. 1, pp. 1–19, Feb. 2024, doi: 10.1038/s41598-024-53396-3.
28. H. E. Ghadbane, S. Barkat, A. Houari, A. Djerioui, H. Abdelhak, and T. Mesbahi, "A load following energy management strategy for a battery-supercapacitor hybrid power system implemented with a PIL co-simulation approach," Smart Grids Sustain. Energy, vol. 9, no. 2, pp. 1–15, Dec. 2024, doi: 10.1007/S40866-024-00214-4/TABLES/4.
29. H. E. Ghadbane, S. Barkat, A. Houari, A. Djerioui, and T. Mesbahi, "Energy management strategy for hybrid power system implemented with processor in the loop," Oct. 2022, Hal Open Science [Online]. Available: https://hal.science/hal-03934029
30. H. E. Ghadbane, and A. F. Mohamed, "Optimizing fuel economy in hybrid electric vehicles using the equivalent consumption minimization strategy based on the arithmetic optimization algorithm," Math., vol. 13, no. 9, p. 1504, May 2025, doi: 10.3390/MATH13091504.

International Journal of Smart Grid (IJSmartGrid)
https://www.ijsmartgrid.org/ Online ISSN: 2602-439X
A. Soeprijanto et al., Vol. 10, No. 1, March, 2026 Research Article

Redefinition of Transient Stability Boundaries for Overcurrent Relay Settings in Multi-Machine Power Systems with VSG Penetration

Adi Soeprijanto*, Ardyono Priyadi*, Dimas Fajar Uman Putra*, Dani Irfani*
Ony Asrarul Qudsi**, Naoto Yorino***

* Department of Electrical Engineering, Institut Teknologi Sepuluh Nopember, Surabaya 60111, Indonesia

** Department of Electrical Engineering, Politeknik Elektronika Negeri Surabaya, Surabaya 60111, Indonesia

*** Graduate School of Advanced Science and Engineering, National Institute of Technology(KOSEN) Kure College, Kure, Japan

(adisup@its.ac.id, priyadi@ee.its.ac.id, dimasfup@its.ac.id, irfanidani8@gmail.com, ony@pens.ac.id, yorino@hiroshima-u.ac.jp)

‡Corresponding Author; Adi Soeprijanto, Buildings A, B, C, and AJ, ITS Campus, Sukolilo, Surabaya 60111, Indonesia, Tel: (+6231) 5994251-54, Ext. 1206,

adisup@its.ac.id

Received: 11.12.2025 Accepted:08.02.2026

Abstract- VSG penetration can affect transient stability in power systems. CCT is the time limit set in OCR to isolate faults and serves as the boundary for power system stability during disturbances. VSG penetration may alter the CCT value, necessitating careful consideration of whether the OCR settings align with system stability boundary. This paper proposes a CCT calculation using the CT method due to VSG penetration. CT is determined through a numerical iteration process based on critical synchronization conditions due to VSG penetration in the power system. This method is sufficiently accurate for CCT calculation in complex systems. VSG penetration is modeled into a multi-machine system to provide a comprehensive view of transient stability. Subsequently, CCT is used as a boundary redefinition for OCR settings. Finally, an investigation is conducted on a modified IEEE 30-bus system, showing changes in transient stability boundary due to VSG penetration, indicating that OCR settings must be adjusted according to stability requirements to ensure the system remains stable after fault clearance. Quantitative validation shows that the proposed modified CT-based approach achieves an accuracy of 99.98% when compared with time-domain simulation–based reference results, demonstrating its high reliability in estimating the transient stability boundary.

Keywords-VSG, Transient Stability, CCT, Critical Trajectory, OCR setting.

1. Introduction

Authors should any word processing software that is Transient stability is a fundamental aspect that must be ensured in the operation of modern power systems, particularly when the system is subjected to large and sudden disturbances such as short circuits, transmission line outages, or protection device failures [1]. Transient stability refers to the ability of a power system to maintain rotor angle synchronism following the clearance of a large

Cite this article as: A. Soeprijanto, A. Priyadi, D. F. U. Putra, D. Irfani, O. A. Qudsi, and N. Yorino, "Redefinition of Transient Stability Boundaries for Overcurrent Relay Settings in Multi-Machine Power Systems with VSG Penetration" *International Journal of Smart Grid (ijSmartGrid)*, Vol. 10, No. 1, pp. 60-72, March, 2026.

disturbance within a specified time interval. In conventional power systems dominated by synchronous generators (SGs), transient stability studies primarily focus on the electromechanical interactions among synchronous machines through the transmission network.

However, the ongoing transition toward power systems with high penetration of renewable energy sources (RESs) has significantly altered system dynamic characteristics [2]. Large-scale integration of inverter-based RESs introduces increased uncertainty, reduced natural inertia, and control dynamics that differ fundamentally from those of conventional synchronous machines [3], [4]. Recent studies have shown that increasing RES penetration requires power systems to exhibit enhanced flexibility and resilience against large disturbances, particularly with respect to transient stability and protection coordination in modern power systems [5]-[7].

In response to these challenges, grid-forming inverters (GFMIs) have been developed to enable inverter-based resources to actively contribute to system stability. Among various GFMI approaches, the virtual synchronous generator (VSG) concept has attracted significant attention due to its capability to emulate the dynamic behavior of synchronous generators through the implementation of virtual inertia, a virtual governor, and a virtual automatic voltage regulator (AVR) [8]-[10]. This approach has been reported to improve frequency stability, voltage stability, and overall dynamic performance of power systems under various disturbance scenarios [11]-[13].

Despite these advancements, the majority of existing VSG-related studies primarily focus on small-signal stability, load fluctuations, or frequency stability, whereas comprehensive investigations of transient stability under large disturbances remain relatively limited [14]-[17]. Several recent works have begun to examine the impact of VSG penetration on transient stability using metrics such as the critical clearing angle (CCA) and the critical clearing time (CCT) [18]-[21]. Among these metrics, CCT is of particular practical relevance, as it directly relates to the allowable operating time of protection devices especially overcurrent relays (OCRs) and therefore plays a crucial role in real-world power system implementation and protection design [22].

Nevertheless, two major limitations can be identified in the existing literature. First, most CCT analyses associated with VSG penetration are conducted using single-machine infinite bus (SMIB) models, which are insufficient to capture the complex interactions among multiple machines and realistic network configurations. In practice, the impact of VSG penetration on transient stability strongly depends on the penetration location, network topology, and inter-machine interactions. Second, variations in CCT resulting from VSG penetration are rarely linked quantitatively to adjustments of OCR settings, leaving the practical implications for protection coordination largely unexplored.

In practical studies, CCT is commonly determined through time-domain simulations based on trial-and-error procedures or numerical fitting, which only provide approximate stability margins without yielding a precise stability boundary [23]. To address this limitation, several direct methods for CCT computation have been proposed, including the boundary controlling unstable equilibrium point (BCU) method and the critical trajectory (CT) method [24]-[27]. The BCU method, which is based on transient energy functions, enables direct computation of CCT but is applicable only to limited classes of power system models. In contrast, the CT method offers greater flexibility and can be applied to more detailed power system models, including multi-machine systems [28]-[30]. However, conventional CT formulations are not designed to accommodate the nonlinear control dynamics and operational characteristics of VSGs, necessitating further modifications to ensure applicability to modern power systems with significant GFMI penetration.

Motivated by these research gaps, this paper aims to develop and apply a modified CT-based approach to quantitatively analyze the impact of VSG penetration on the transient stability of multi-machine power systems. The CCT is computed through numerical integration of the nonlinear differential equations governing system dynamics before, during, and after fault clearance. The transient stability boundary is identified using a loss-of-synchronization (LOS) criterion defined with respect to the center of inertia (COI), enabling critical trajectory analysis for both SGs and VSGs within a unified multi-machine framework. The resulting CCT values are subsequently employed as quantitative stability limits for the determination and optimization of OCR settings with inverse definite minimum time (IDMT) characteristics, which are well suited for complex power systems with high levels of RES penetration [31].

As summarized in Table 1, existing studies either investigate VSG dynamic behavior without providing quantitative critical clearing time boundaries or address CCT estimation without explicitly considering grid-forming inverter dynamics and protection coordination. This paper uniquely integrates these aspects by establishing a CCT-based transient stability boundary for overcurrent relay settings in multi-machine power systems with virtual synchronous generator penetration.

The main contributions of this paper can be summarized as follows:

1. Providing guidelines for OCR settings based on the transient stability boundary of power systems under VSG penetration.

2. CCT calculation and system analysis due to VSG penetration are performed using the CT method to determine the system's stability boundary during faults.
3. The transient stability analysis mechanism of power systems due to VSG penetration is modeled using a multi-machine model, taking into account the network configuration with reference to the COI.

This paper is organized as follows. Section 2 describes the VSG penetration model in a multi-machine system. Section 3 explains the problem formulation for the quantitative calculation of CCT and transient stability boundary redefinition for OCR settings. Section 4 presents the simulation results with several test cases on the modified IEEE 30-bus system. Finally, Section 5 provides the conclusion of the paper.

2. System Modelling

2.1. VSG System Modelling

The topology of the VSG system is shown in Fig. 1. The active current in the VSG generates active power P, while the reactive current in the VSG generates reactive power Q. In this study, the transient stability analysis is confined to the inertial response time frame immediately following a large disturbance, during which the system dynamics are dominated by pure virtual inertia emulation of the VSG, while the effects of current limiting, converter saturation, control mode transitions, and primary or higher-level control actions are not considered due to their inherently slower response times [32]. Table 2 presents the VSG parameters used.

Table 1. Comparison of existing studies and the proposed approach

Ref	Power System Model	VSG Penetration Analysis	Transient Stability Evaluation	CCT Determination Method	Protection System Integration
[1]	Weak grid, inverter-dominated system	Yes (IBR-based RES)	Small-signal and dynamic stability	Not considered	No
[2]	Hybrid system (SG + grid-forming devices)	Yes	Time-domain transient stability	Not explicitly addressed	No
[3]	Inverter-intensive hybrid power plant	Yes	Small-signal stability	Not considered	No
[4]	Power system with AGC	Yes (VSG-based RES)	Frequency stability	Not considered	No
[8]	Parallel SG-VSG system with induction motor loads	Yes	Transient voltage stability	Not considered	No
[9]	Review of VSG models	Yes	Not specifically evaluated	Not considered	No
[10]	Single VSG-based system	Yes	Transient stability (controller-oriented)	Not considered	No
[14]	Single-machine VSG system	Yes	Frequency stability	Not considered	No
[15]	SG-VSG system	Yes	Low-frequency oscillation analysis	Not considered	No
[16]	Multi-VSG system	Yes	Transient stability	Not explicitly addressed	No
[19]	Parallel current-controlled VSCs and VSGs	Yes	Transient stability and current injection behavior	Not explicitly addressed	No
[20]	Single VSG-based system	Yes	Transient stability	Not considered	No
[21]	Grid-forming converter-based system	Yes (GFMI)	Transient stability	Yes (CCT)	No
[22]	Active distribution network with DERs	Not VSG-specific	Stability-constrained analysis	Not considered	Yes (OCR setting)
In this paper	Multi-machine power system	Yes (penetration level and location considered)	Transient stability under large disturbances	Yes (Critical Trajectory method)	Yes (OCR IDMT setting based on CCT)

The active power and reactive power generated by the VSG can be formulated according to equations (1) and (2).

$$P = \frac{V_g V_{VSG}}{X_L} \sin\delta \quad (1)$$

$$Q = \frac{V_{VSG}(V_{VSG} - V_g \cos\delta)}{X_L} \quad (2)$$

The VSG control system consists of the swing equation and the electromagnetic equation, which can be expressed by equations (3).

$$J\omega \frac{d^2\delta}{dt^2} = P_{rated} - P \quad (3)$$

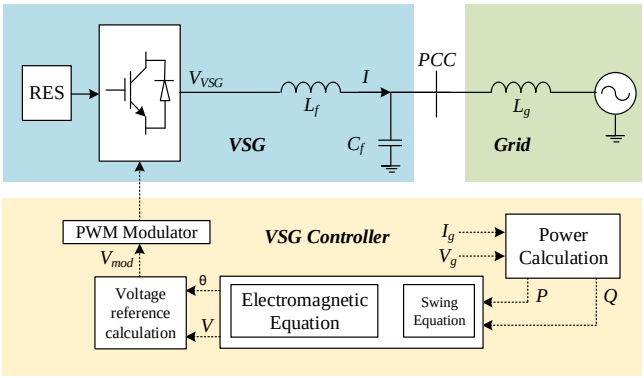

Fig. 1. VSG system topology.

By substituting equation (1) into equation (3), equation (4) is obtained.

$$J\omega \frac{d^2\delta}{dt^2} = P_{rated} - \frac{V_g V_{VSG}}{X_L} \sin\delta \quad (4)$$

Table 2. Main Parameters of VSG Used in Simulation

Parameter	Unit	VSG 1	VSG 2	VSG 3	VSG 4
P_{rated}	*MW*	30	20	25	20
Q_{rated}	*MVAR*	25	20	15	20
V_{VSG}	*p.u.*	1.082	1.082	1.082	1.082
X_L	*p.u.*	0.184	0.184	0.184	0.184
J	*p.u.*	2.5	2.5	2.5	2.5

2.2. Fault Condition of VSG

The transient stability of the system is assessed based on the conditions before the fault occurs, during the fault, and after the fault is cleared. Fig. 2 shows the equivalent circuit of the system for these three conditions. V_L is the voltage drop across the network, with $V_L = V_{VSG} - V_g$. X_g consisting of X_{g1} and X_{g2}. The superscripts ' and " represent the during-fault and post-fault conditions, respectively. Based on Fig. 3(a), there is a difference in the value of X_g in the pre-fault, during-fault, and post-fault conditions ($X_g' < X_g < X_g''$), which affects the voltage and current in the system, as shown in the phasor diagram in Fig. 3(b). From Fig. 3, V_{VSG} and I can be formulated according to equations (5) and (6).

$$V_{VSG} = I(X_L + X_g) + V_g \quad (5)$$

$$I = \frac{V_{VSG} - V_g}{X_L + X_g} \quad (6)$$

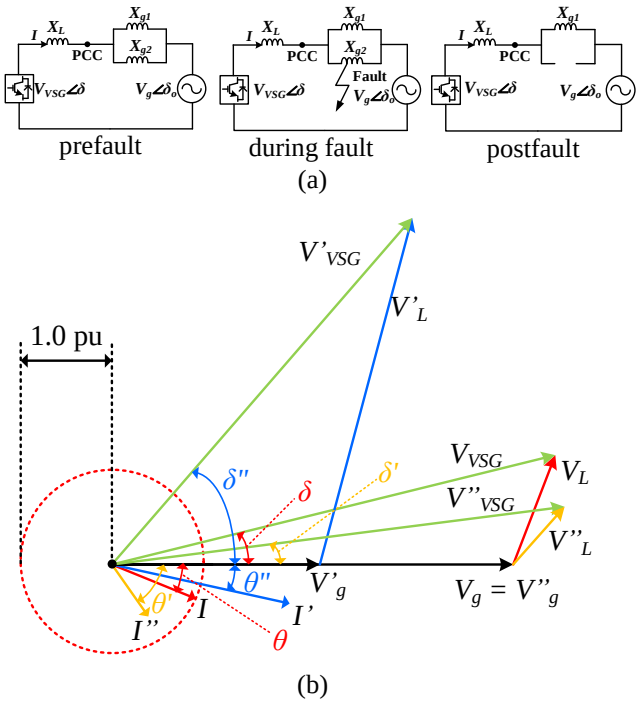

Fig 2. System condition (a) equivalent circuit for prefault, during fault, and postfault; (b) phasor diagram for prefault, during fault, and postfault.

2.3. Multi-machine Models

The equivalent circuit model of the generation system, network, and load is shown in Fig. 3. The rotor angle of each machine, including the VSG, depends on the terminal voltage and internal reactance. The machine terminal voltage and the PCC VSG voltage are obtained through the power flow iteration process.

To reduce complexity, a reduction is performed to simplify the analysis and mathematical calculations. In this research, Kron reduction is used to eliminate the load bus from the admittance matrix. The subscript n denotes the bus number, while the subscripts i and p represent the generator bus and the location of VSG penetration, respectively.

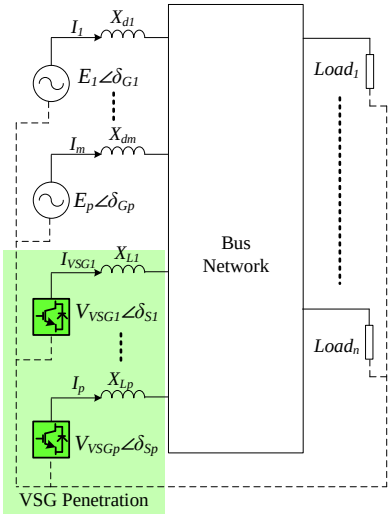

Fig. 3. Representation of multimachines system.

Thus, a complex multi-machine system is simplified according to the following equations:

$$\begin{bmatrix} Y_{11} & \cdots & Y_{1(n-1)} & Y_{1k} & Y_{1p} \\ \vdots & \ddots & \vdots & \vdots & \vdots \\ Y_{(n-1)1} & \cdots & Y_{(n-1)(n-1)} & Y_{nk} & Y_{np} \\ Y_{k1} & \cdots & Y_{kn} & Y_{kk} & Y_{kp} \\ Y_{p1} & \cdots & Y_{pn} & Y_{pk} & Y_{pp} \end{bmatrix} \textit{yields} \begin{bmatrix} Y_{11} & \cdots & Y_{1(n-1)} \\ \vdots & \ddots & \vdots \\ Y_{(n-1)1} & \cdots & Y_{(n-1)(n-1)} \end{bmatrix} \quad (7)$$

3. Problem Formulation of Proposed Method

CCT is the system stability boundary to be determined in this research. Quantitatively, CCT is calculated through a numerical iteration process based on CT with an end point at LOS. CCT lies between the ST and UT after the fault is cleared. The steps involved in the CCT calculation process are shown in Fig. 4. The procedure starts with system data initialization, including generator, network, and load parameters, followed by steady-state power flow calculation. Kron matrix reduction is then applied to obtain the reduced network model for transient analysis. The initial state variables before fault occurrence are determined, and a three-phase fault is introduced to evaluate system dynamics. The critical clearing time (CCT) is computed using a modified Critical Trajectory (CT) method by numerically integrating the nonlinear differential equations and identifying the loss-of-synchronization (LOS) condition based on the center-of-inertia reference. Finally, the obtained CCT is employed as a quantitative stability boundary for redefining overcurrent relay (OCR) settings, ensuring that relay operation time does not exceed the transient stability limit.

The proposed CT-based approach requires numerical integration of system differential equations combined with a limited number of trajectory iterations to identify the critical clearing time. Compared to conventional trial-and-error time-domain scanning, the method significantly reduces computational effort by directly converging toward the stability boundary.

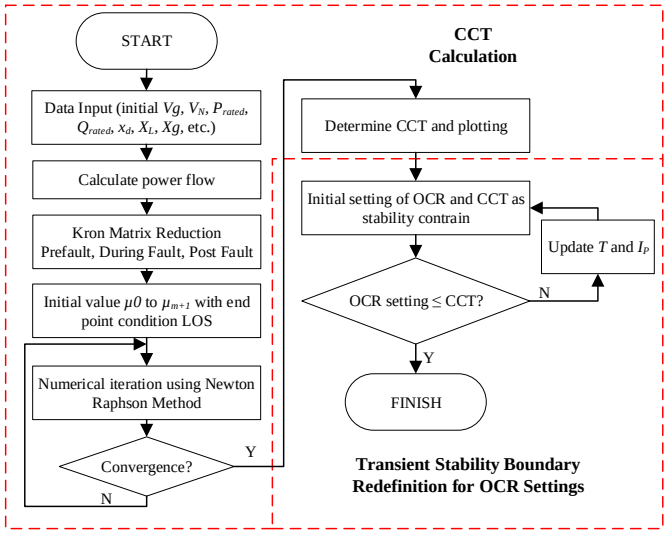

Fig. 4. Procedure of transient stability boundary redefinition for OCR settings.

The convergence behavior is robust, as the iteration process terminates once the LOS criterion is reached, and no sensitivity to initial guesses was observed in the conducted studies. Furthermore, the proposed approach is well suited for protection setting, as individual fault scenarios can be evaluated independently and executed in parallel, making the method scalable for larger power systems and multiple contingency assessments as demonstrated in [29] and [30].

3.1. COI Reference with VSG Penetration

The concept of COI is employed in this study to represent the collective behavior of all generators in the system as a single inertia mass, providing a more realistic approach to analyzing the dynamic interactions between generators during transient conditions. P_e in the bus network must be calculated first. This electrical power flow is based on the power generated by the SG and VSG. To prevent the SG and VSG from losing synchronization in the multi-machine system, the angles δ of the SG and VSG must follow the P_{COI} reference. P_{COI} is expressed according to the following equation:

$$P_{COI} = \left(\sum_{i=1}^{n} P_{mi} - P_{ei}(\delta_i)\right) + \left(\sum_{p=1}^{n} P_{mp} - P_{ep}(\delta_p)\right) \quad (8)$$

Using the COI concept, the swing equation with respect to the COI reference is as follows:

$$M_{(i+p)} \frac{d^2\delta_{(i+p)}}{dt^2} = \left(P_{mi} + P_{mp}\right) - \left(P_{ei} + P_{ep}\right) - \frac{M_{(i+p)}}{M_T} P_{COI} \quad (9)$$

M is the constant inertia of both the SG and VSG, which is the product of the moment of inertia J and the angular velocity ω. M_T is the total moment of inertia, calculated

using the following equation:

$$M_T = \left(\sum_{i=1}^{n} M_i\right) + \left(\sum_{p=1}^{n} M_p\right) \tag{10}$$

3.2. Critical Condition of the System

The CT method end point condition is LOS. According to reference [29], the LOS in a multi-machine system can be expressed by the following equation:

$$\begin{cases} \left[\dfrac{\partial P}{\partial \delta}\right].v \\ v \neq 0 \end{cases} \tag{11}$$

v is the eigenvector associated with the zero eigenvalue of the matrix $[\partial P/\partial \delta]$. As shown in Fig. 5, μ_u represents the end point based on LOS. By maintaining the value of μ_u as the end point condition, numerical iteration is then performed with the initialization of δ_0 and ω_0, starting from the pre-fault condition to the post-fault condition, as the network configuration changes during the fault. δ_0 and ω_0 can be calculated using equations (12) and (13).

$$\delta_0 = \frac{1}{M_T}\left(\sum_{i=1}^{n} M_i \delta_i + \sum_{p=1}^{n} M_p \delta_p\right) \tag{12}$$

$$\omega_0 = \frac{1}{M_T}\left(\sum_{i=1}^{n} M_i \omega_i + \sum_{p=1}^{n} M_p \omega_p\right) \tag{13}$$

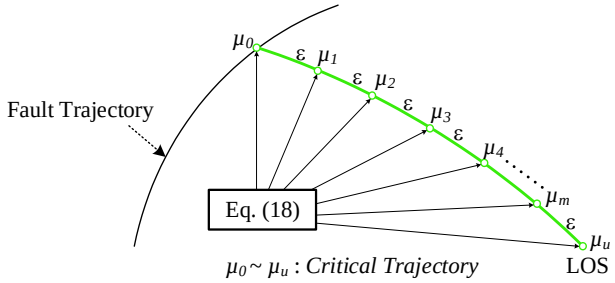

Fig. 5. Fault trajectory after fault clearing.

The pair δ_0 and ω_0 in equations (12) and (13) are nonlinear functions of a second-order differential equation. This function can be expressed by the following equation:

$$\mu = f(\mu, \mu_0, t) \tag{14}$$

Represented as a matrix with dimensions ($2n$+1),

$$\mu = [\delta_1, \omega_1, \delta_2, \omega_2, ..., \delta_n, \omega_n] \tag{15}$$

Numerical iteration is performed until the end point condition is reached, as shown in the following equation:

$$\mu_k = \mu_{k+1} - \mu_k - \frac{\dot{\mu}_{k+1} + \dot{\mu}_k}{\left|\dot{\mu}_{k+1} + \dot{\mu}_k\right|}\varepsilon \tag{16}$$

Where $\mathcal{E}$ is the distance between the two points of μ.

3.3. Iterative CCT Calculation Based on CT

The fault trajectory is obtained during the disturbance period [0,τ]. The fault trajectory can be expressed by the following equation:

$$\dot{\mu} = f(\mu); 0 \le t \le \tau; \mu(0) = \mu \tag{17}$$

$$\mu(t) = \chi(t; \mu); 0 \le t \le \tau \tag{18}$$

When the fault is cleared at time τ, the dynamic change in the trajectory becomes:

$$\dot{\mu} = f(\mu), \tau \le t \le \infty; f : R_N \to R_N \tag{19}$$

After the fault is cleared, the post-fault trajectory can be expressed by the following equation:

$$\mu(t) = \chi(t; \mu_0), \tau \le t \le \infty; \chi(\cdot; \mu_0 : R_N \to R_N) \tag{20}$$

CCT is determined based on the post-fault trajectory when the fault is cleared at time τ under the following conditions:

$$\mu_0 = \chi_F(\tau; \mu_{pre}), \tau = CCT \tag{21}$$

3.4. Transient Stability Boundary Redefinition for OCR Settings Based on CCT

The settings are configured by combining the standard inverse curve and the definite time curve. The key parameters in OCR settings are I_P and TSM [33]. In the IDMT characteristic, I_P and TSM are interrelated for OCR configuration, thus the transient stability boundary redefinition problem is represented by the following equation:

$$Minimize \to \sum_{f=1}^{f_{max}}\left(\sum_{i=1}^{n} T_i\right) \tag{22}$$

I_P can be determined according to the following constraints:

$$1.1 I_{FLi} \le I_{Pi} \le \alpha I_{FMi} \tag{23}$$

with,

$$\begin{cases} \alpha = 0.6 \to 0.6 I_{FMi} \ge 1.1 I_{FLi} \\ \alpha = 0.8 \to otherwise \end{cases} \tag{24}$$

Meanwhile, TSM is determined based on the following equation:

$$T_i = \frac{0.14}{\left(I_{Fi}/I_{Pi}\right)^{0.02} - 1} TSM_i \quad (25)$$

To solve the transient stability boundary redefinition problem in equation (24), CCT is used as the constraint for the settings. Thus, the OCR operating time can be expressed by the following equation:

$$T_i \leq CCT \quad (26)$$

4. Case Study, Result, and Analysis

The test case system is conducted on the modified IEEE 30-bus system with VSG penetration [34]. The penetration locations are shown in Fig. 6. There are ten three-phase ground fault points (A, B, C, D, E, F, G, H, I, and J) for investigation and analysis. The faults occur on transmission lines located near buses. For example, fault point "E" occurs on the line between bus 2 and bus 6, with the fault location near bus 2. Subsequently, transient stability boundary redefinition for OCR settings are applied to the OCR closest to the fault point on the transmission line, as illustrated in Fig. 7.

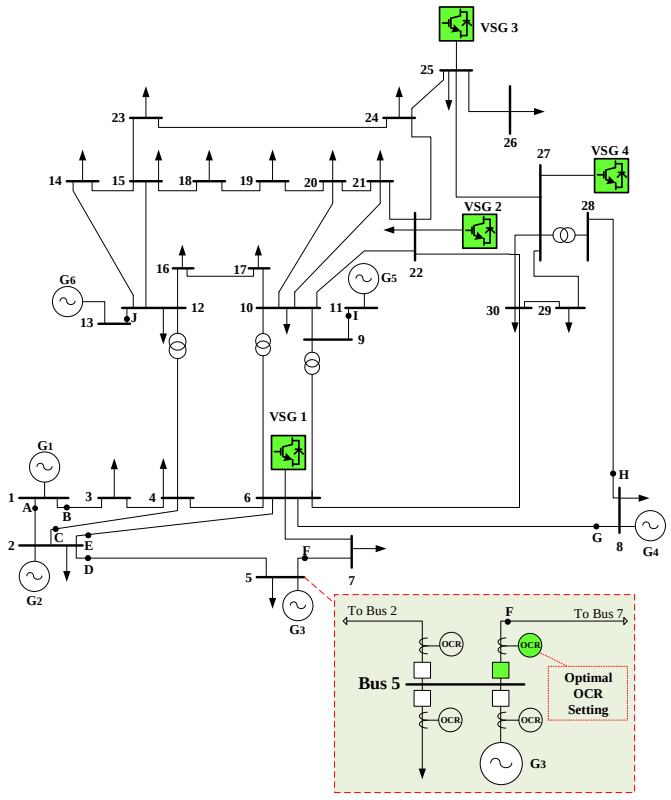

Fig. 6. Modified IEEE 30 bus systems with VSG penetration.

Based on Fig. 7, five test cases are used for VSG penetration as follows:

- *Test case 1*: VSG 1, VSG 2, VSG 3, and VSG 4 are penetrated.
- *Test case 2*: VSG 2, VSG 3, and VSG 4 are penetrated.
- *Test case 3*: VSG 1, VSG 3, and VSG 4 are penetrated.
- *Test case 4*: VSG 1, VSG 2, and VSG 4 are penetrated.
- *Test case 5*: VSG 1, VSG 2, and VSG 3 are penetrated.

CCT and transient stability boundary redefinition for OCR settings are provided in Tables II-VI. The proposed modified CT method for CCT calculation is compared with the TDS method, based on numerical fitting of τ. For example, the CCT value "0.84-0.85" at fault point "I" in Table II indicates that the system will remain stable if ST with τ_s = 0.84s and will become unstable if UT with τ_u = 0.85s. This serves as a reference for determining whether the CCT obtained through the CT method is accurate in determining CCT. Subsequently, the CCT is used as a boundary for setting the OCR to achieve the transient stability boundary redefinition for OCR setting.

4.1. Existing Condition Without VSG Penetration

In the existing condition without VSG penetration, CCT values and OCR settings with transient stability limits for each fault point are obtained, as shown in Table 3. Based on the data in Table 1, the average accuracy of the CCT calculated using the proposed method is 99.93%. The CCT obtained for each fault point is used for OCR settings. These OCR settings serve as the initial OCR configuration before redefinition is performed due to VSG penetration.

Table 3. CCT and OCR setting of modified IEEE 30 bus system without VSG penetration

Fault	CCT Calculation			Existing OCR Setting		
	ST - UT (s)	CT (s)	Accuracy (%)	TSM	I_P	T (s)
A	0.50-0.51	0.5011	100%	4.4	8.80	0.425
B	0.51-0.52	0.5129	100%	2.5	3.15	0.475
C	0.62-0.63	0.6281	100%	3.2	2.35	0.550
D	0.62-0.63	0.6238	100%	3.4	2.66	0.550
E	0.62-0.63	0.6289	100%	3.8	2.78	0.550
F	1.33-1.34	1.3423	99.83%	1.1	4.77	1.250
G	1.43-1.44	1.4473	99.49%	1.6	8.07	1.300
H	1.67-1.68	1.6780	100%	0.4	1.37	1.525
I	0.97-0.98	0.9764	100%	1.7	5.07	0.850
J	1.03-1.04	1.0388	100%	1.9	5.41	0.950

4.2. Transient Stability Analysis and Redefinition OCR Setting due to VSG Penetratition

VSG penetration impacts the system's stability boundary, which will change depending on the location of VSG penetration. The study conducted on test cases 1-5 shows changes in CCT as a stability boundary. The CCT at

fault points "A", "B", and "H" in test cases 1, 3, 4, and 5 is greater than the CCT in the existing condition at the same fault points. Meanwhile, in test case 2, the CCT at fault points "A", "B", "G", and "H" is greater than the CCT in the existing condition at the same fault points. Thus, the transient stability boundary redefinition for OCR setting can remain the same as in the existing condition when the CCT due to VSG penetration is larger, as the system stability becomes greater than in the existing condition. However, at other fault points, redefinition is required because the CCT changes with stability limits lower than those in the existing condition.

- *Test Case 1*

In test case 1, there is a penetration of VSG 1 with a capacity of 30 MW, VSG 2 with a capacity of 20 MW, VSG 3 with a capacity of 25 MW, and VSG 4 with a capacity of 20 MW, resulting in a total VSG penetration capacity of 27% in the system. The CCT and redefinition for OCR settings are shown in Table 4. The average accuracy of the proposed method for CCT calculation in test case 1 is 100%.

Table 4. CCT and redefinition OCR setting of modified IEEE 30 bus system in Test Case 1

Fault	CCT Calculation			Redefinition OCR Setting		
	ST - UT (s)	CT (s)	Accuracy (%)	TSM	I_P	T (s)
A	0.84-0.85	0.8437	100%	4.4	8.80	0.425
B	0.85-0.86	0.8567	100%	2.5	3.15	0.475
C	0.62-0.63	0.6251	100%	8.9	5.22	0.55
D	0.62-0.63	0.6229	100%	5.2	5.02	0.5
E	0.62-0.63	0.6256	100%	5.2	6.38	0.5
F	0.97-0.98	0.9711	100%	3.7	10.15	0.9
G	0.80-0.81	0.8063	100%	3.7	18.08	0.775
H	1.74-1.75	1.7400	100%	0.4	1.37	1.525
I	0.84-0.85	0.8419	100%	2.3	10.94	0.75
J	0.85-0.86	0.8589	100%	2.7	11.53	0.775

- *Test Case 2*

In test case 2, there is a penetration of VSG 2 with a capacity of 20 MW, VSG 3 with a capacity of 25 MW, and VSG 4 with a capacity of 20 MW, resulting in a total VSG penetration capacity of 19% in the system. The CCT and redefinition OCR settings are shown in Table 5. The average accuracy of the proposed method for CCT calculation in test case 2 is 99.98%. Fig. 7 illustrates the difference in redefinition OCR settings with VSG penetration in test case 2 at fault location point "C" compared to the existing condition.

- *Test Case 3*

In test case 3, there is a penetration of VSG 1 with a capacity of 30 MW, VSG 3 with a capacity of 25 MW, and VSG 4 with a capacity of 20 MW, resulting in a total VSG penetration capacity of 21% in the system. The CCT and redefinition OCR settings are shown in Table 6. The average accuracy of the proposed method for CCT calculation in test case 3 is 100%.

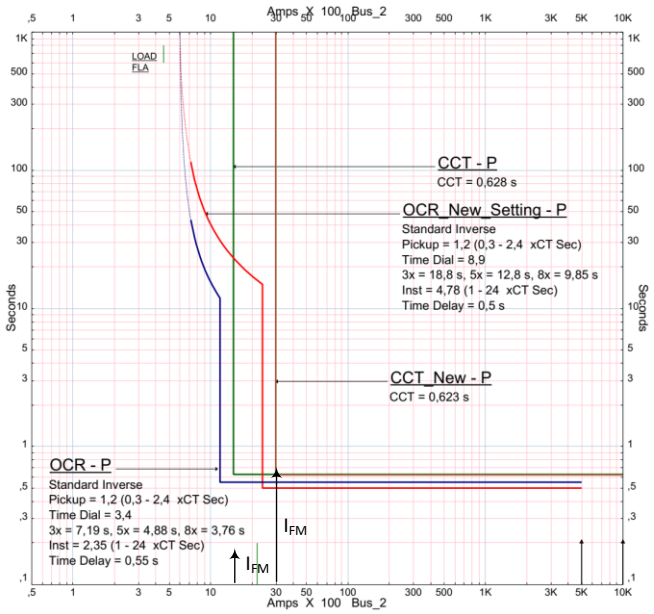

Fig. 7. Transient stability boundary redefinition for OCR Setting with VSG penetration in test case 2 at fault location point "C".

Table 5. CCT and redefinition OCR setting of modified IEEE 30 bus system in Test Case 2

Fault	CCT Calculation			Redefinition OCR Setting		
	TDS (s)	CT (s)	Accuracy (%)	TSM	I_P	T (s)
A	0.70-0.71	0.7087	100%	4.4	8.80	0.425
B	0.70-0.71	0.7095	100%	2.5	3.15	0.475
C	0.62-0.63	0.6227	100%	8.9	4.78	0.50
D	0.62-0.63	0.6203	100%	5.2	4.96	0.50
E	0.62-0.63	0.6227	100%	5.2	5.67	0.50
F	1.02-1.03	1.0290	100%	3.7	9.40	0.95
G	2.07-2.08	2.0850	99.76%	3.7	16.12	1.95
H	1.84-1.85	1.8440	100%	0.4	1.37	1.525
I	0.84-0.85	0.8453	100%	2.3	10.52	0.75
J	0.85-0.86	0.8530	100%	2.7	11.10	0.775

Table 6. CCT and redefinition OCR setting of modified IEEE 30 bus system in Test Case 3

Fault	CCT Calculation			Redefinition OCR Setting		
	TDS (s)	CT (s)	Accuracy (%)	TSM	I_P	T (s)
A	0.75-0.76	0.7561	100%	4.4	8.80	0.425
B	0.75-0.76	0.7513	100%	2.5	3.15	0.475
C	0.59-0.60	0.5975	100%	8.9	4.98	0.5
D	0.62-0.63	0.6203	100%	5.2	4.88	0.5
E	0.61-0.62	0.6155	100%	5.2	6.10	0.55
F	1.01-1.02	1.0126	100%	3.7	9.75	0.95
G	0.81-0.82	0.8110	100%	3.7	17.28	0.75
H	1.81-1.82	1.8162	100%	0.4	1.37	1.525
I	0.89-0.90	0.8980	100%	2.3	10.05	0.8
J	0.91-0.92	0.9165	100%	2.7	10.75	0.875

- *Test Case 4*

In test case 4, there is a penetration of VSG 1 with a capacity of 30 MW, VSG 2 with a capacity of 20 MW, and VSG 4 with a capacity of 20 MW, resulting in a total VSG penetration capacity of 20% in the system. The CCT and redefinition OCR settings are shown in Table 7. The average accuracy of the proposed method for CCT calculation in test case 4 is 99.999%.

- *Test Case 5*

In test case 5, there is a penetration of VSG 1 with a capacity of 30 MW, VSG 2 with a capacity of 20 MW, and VSG 3 with a capacity of 25 MW, resulting in a total VSG penetration capacity of 21% in the system. The CCT and redefinition OCR settings are shown in Table 8. The average accuracy of the proposed method for CCT calculation in test case 5 is 100%. Fig. 8 illustrates the difference in transient stability boundary redefinition for OCR settings with VSG penetration in test case 5 at fault location point "G" compared to the existing condition.

Table 7. CCT and redefinition OCR setting of modified IEEE 30 bus system in Test Case 4

Fault	CCT Calculation			Redefinition OCR Setting		
	TDS (s)	CT (s)	Accuracy (%)	TSM	I_P	T (s)
A	0.67-0.68	0.6784	100%	4.4	8.80	0.425
B	0.68-0.69	0.6850	100%	2.5	3.15	0.475
C	0.59-0.60	0.5900	100%	8.9	5.03	0.5
D	0.59-0.60	0.5915	100%	5.2	4.86	0.5
E	0.59-0.60	0.5902	100%	5.2	6.15	0.5
F	0.98-0.99	0.9880	100%	3.7	9.79	0.92
G	0.81-0.82	0.8200	100%	3.7	17.45	0.75
H	1.79-1.80	1.7899	99.99%	0.4	1.37	1.525
I	0.86-0.87	0.8602	100%	2.1	10.55	0.75
J	0.87-0.88	0.8784	100%	2.2	11.09	0.8

Table 8. CCT and redefinition OCR setting of modified IEEE 30 bus system in Test Case 5

Fault	CCT Calculation			Redefinition OCR Setting		
	TDS (s)	CT (s)	Accuracy (%)	TSM	I_P	T (s)
A	0.69-0.70	0.6994	100%	4.4	8.80	0.425
B	0.70-0.71	0.7042	100%	2.5	3.15	0.475
C	0.59-0.60	0.5912	100%	7.4	4.40	0.5
D	0.58-0.59	0.5892	100%	5.2	4.99	0.5
E	0.58-0.59	0.5896	100%	5.2	5.21	0.55
F	0.96-0.97	0.9640	100%	3.7	8.95	0.9
G	0.78-0.79	0.7896	100%	3.9	15.13	1.7
H	1.75-1.76	1.7557	100%	0.4	1.37	1.525
I	0.85-0.86	0.8565	100%	2.0	9.51	0.75
J	0.85-0.86	0.8589	100%	1.9	10.14	0.775

The radar diagram in Fig. 9 shows the changes in CCT due to VSG penetration in the modified IEEE 30-bus system. At certain fault locations, the CCT values increase, providing better stability boundary. However, at different fault locations, the CCT values decrease, leading to worse stability boundary. A closer examination reveals that the reduction in CCT values occurs at fault locations near the VSG penetration point. For instance, at fault location G in Test Case 2, where no VSG1 penetration is present, the CCT value increases compared to Test Cases 1, 3, 4, and 5 with VSG1 penetration. This phenomenon is attributed to the increased short-circuit current contribution at locations close to the VSG penetration, which consequently reduces the CCT as the transient stability boundary. This indicates that redefinition of the OCR settings is necessary to ensure the system remains stable after the fault is cleared.

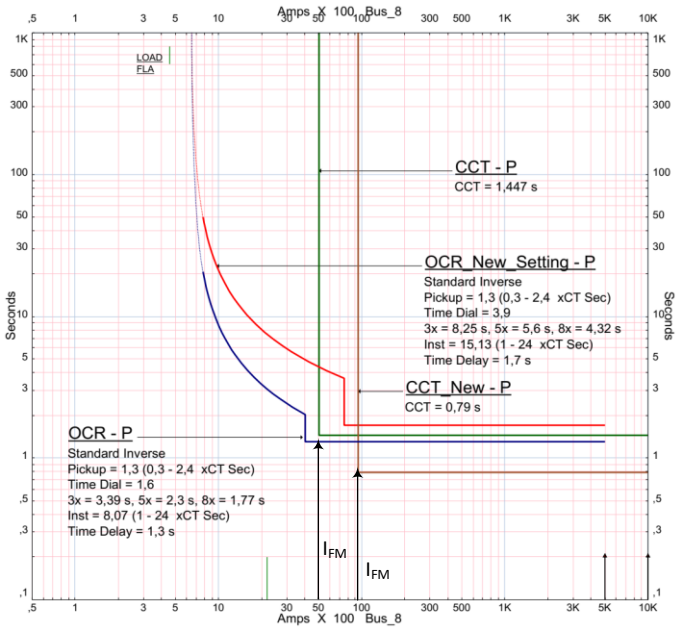

Fig. 8. Transient stability boundary redefinition for OCR Setting with VSG penetration in test case 5 at fault location point "G".

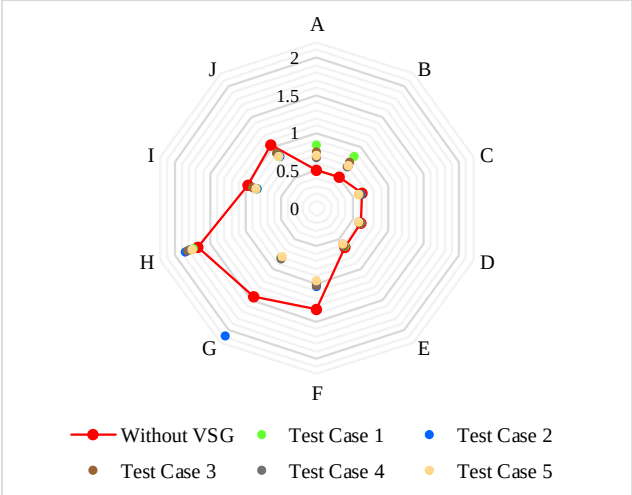

Fig. 9. CCT comparison of modified IEEE 30 bus systems with VSG penetration using Test Case 1-5 in "A" – "J" fault point.

Fig. 10 shows the angular velocity (ω) vs. angle (δ) curve for SG and VSG, which forms the trajectory. When the fault is cleared by opening the CB through OCR settings at $T = \tau_s$, the fault trajectory of each SG and VSG follows the stable trajectory "2." Conversely, when the fault is cleared by opening the CB through OCR settings at $T = \tau_u$, the fault trajectory of each SG and VSG follows the unstable trajectory "3." Trajectory "4" represents the stability boundary for SG and VSG, calculated based on the proposed modified CT method for redefinition OCR settings due to VSG penetration in the system. The proposed CT method lies between the stable trajectory and the unstable trajectory. Based on the data in Tables 3-8, the average accuracy of the proposed method is 99.98%. This indicates that the proposed method is accurate in assessing the impact of VSG penetration on system stability.

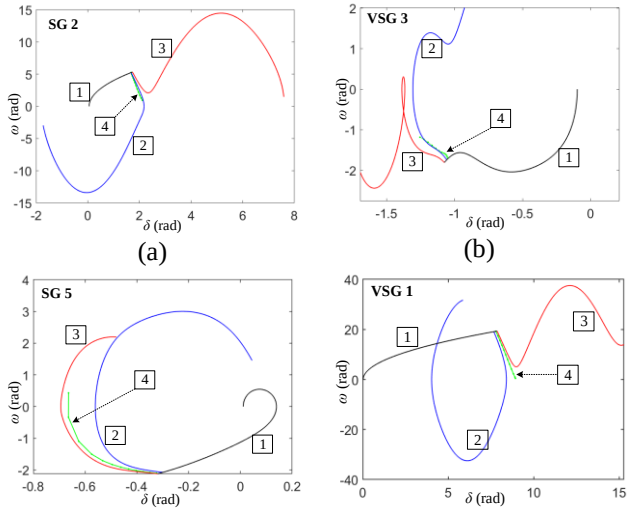

Fig. 10. Angular velocity (ω) vs angle (δ) curve of the SG and the VSG which representation trajectory of Modified IEEE 30 bus systems with Test Case 1 (a) SG 2 when fault occur in point "D", (b) VSG 3 when fault occur in point "D", (c) SG 5 when fault occur in point "G", (d) VSG 1 when fault occur in point "G".

The dynamic behavior of SG and VSG when the fault is cleared by the CB with redefinition OCR settings based on CCT calculation using the CT method can be seen in Fig. 11. The dynamic behavior of angle δ for SG 1-6 and VSG 1-4 during the fault at point "I" until the fault is cleared in test case 1 is shown in Fig. 11(a). When the fault is cleared with $T \leq$ CCT, the δ of each SG and VSG fluctuates but still demonstrates stable behavior, as the δ values for both SG and VSG fluctuate within certain limits. Similarly, the dynamic behavior of ω for SG and VSG in Fig. 11(b) shows that the ω fluctuations remain stable, as the dynamic behavior of ω for all generators and VSGs is within certain bounds. Fig. 11(c) shows the behavior of δ in SG 3 and VSG 1 when the fault is cleared at T = CCT and $T = \mu_u$. When the fault is cleared at T = CCT, the δ of SG 3 and VSG 1 demonstrates stable behavior. However, when the fault is cleared at $T = \mu_u$, the δ of SG 3 and VSG 1 increasingly moves in the negative direction. This indicates unstable behavior when the fault is cleared at $T = \mu_u$.

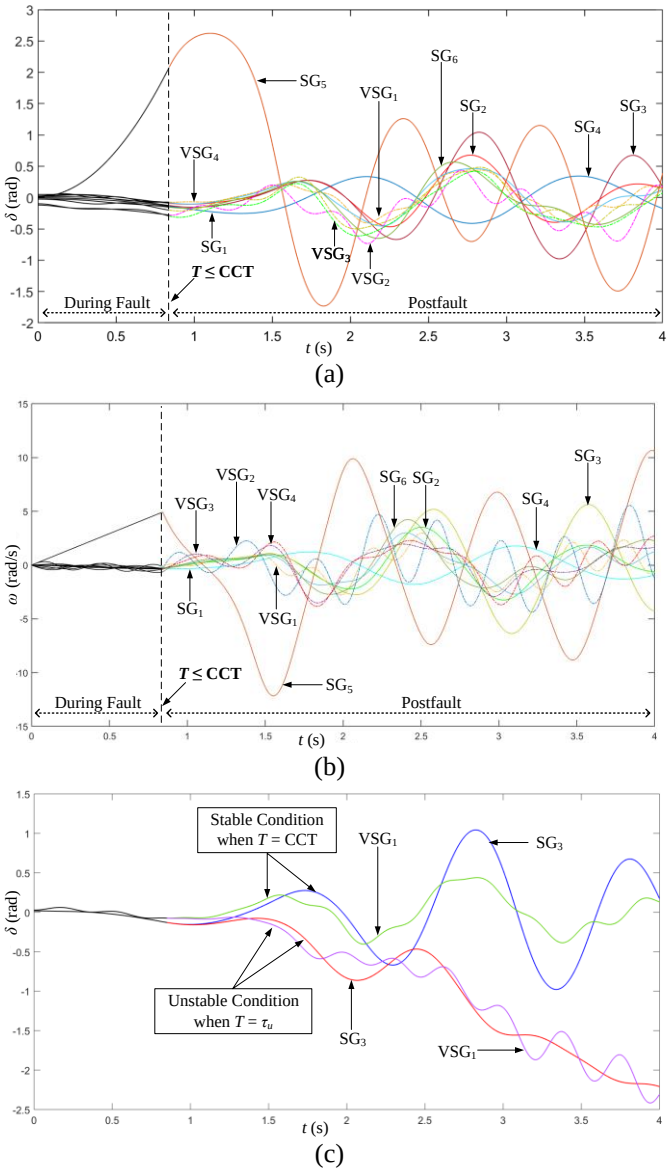

Fig. 11. Dynamic behavior of the SG 1-6 and the VSG 1-4 for fault in point "I" of Modified IEEE 30 bus systems with Test Case 1 when fault cleared in $T \leq$ CCT, (a) Angle (δ) behavior, (b) Angular velocity (ω) behavior, (c) Stable and unstable condition of the SG 3 and the VSG 1.

5. Conclusion

This study demonstrates that the CT method provides an accurate approach for determining the CCT in power systems with VSG penetration. Based on the data in Tables 3-8, the average accuracy of the proposed method is 99.98%. This indicates that the proposed method is accurate in assessing the impact of VSG penetration on system stability.

Changes in the system's stability boundary are evaluated based on variations in the CCT value due to VSG penetration, which are subsequently used as the basis for redefinition OCR settings. Simulation results have confirmed that the proposed method successfully achieves the primary objectives of analyzing transient stability and redefinition OCR settings in the presence of VSG penetration in power systems. If a fault is cleared within the CCT, the fault trajectory will oscillate around the stable equilibrium point, allowing the system to regain stability. However, if the fault is cleared beyond the CCT, the fault trajectory will exceed the stability limit, causing the system to become unstable. Therefore, this work provides a novel framework for assessing the impact of VSG integration, offering system stability analysis for modern power systems and paving the way for more resilient and sustainable grid operations.

Despite these contributions, several limitations should be acknowledged. The analysis is conducted under predefined VSG parameters and assumes idealized protection operation without considering delays, relay coordination, or adaptive protection schemes. Moreover, nonlinear effects such as converter saturation, detailed current-limiting behavior, and control mode transitions under severe faults are not explicitly modeled, which may influence the transient stability boundary in practical implementations. Future research will focus on extending the proposed framework to incorporate detailed VSG control nonlinearities, adaptive and communication-assisted protection strategies, and validation using larger-scale power systems and real-time simulation or hardware-in-the-loop platforms.

Acknowledgements

The authors would like to express their sincere gratitude to the Ministry of Education, Science, and Technology of the Republic of Indonesia for the support provided under contract number 017/C3/DT.05.00/PL/2025, which has greatly contributed to the completion of this research.

The authors used ChatGPT (OpenAI) to assist grammar improvements during manuscript preparation. All content has been reviewed and verified by the authors for accuracy and integrity.

Author Contributions

Adi Soeprijanto conceived and supervised the study; Ardyono Priadi and Dimas Fajar Uman Putra contributed to the methodology, system modeling, and analysis; Dani Irfani and Ony Asrarul Qudsi supported the investigation, validation, and data interpretation; Naoto Yorino provided technical review and critical revision of the manuscript. All authors have read and agreed to the published version of the manuscript.

Conflict of Interest

The author(s) declared no potential conflicts of interest with respect to the research, authorship, and/or publication of this article.

References

[1] M. I. Saleem, S. Saha, U. Izhar and L. Ang, “Stability assessment of inverter-based renewable energy sources integrated to weak grids”, IET Energy Syst. Integr., 1-20 (2024), https://doi.org/10.1049/esi2.12151.

[2] X. He, S. Pan and H. Geng, "Transient stability of hybrid power systems dominated by different types of grid-forming devices", IEEE Transactions on Energy Conversion, vol. 37, no. 2, pp. 868-879, June 2022, doi: 10.1109/TEC.2021.3113399.

[3] L. Ding, J. Zhang, X. Lu, S. Dong, A. Hoke and J. Tan, "Inverter intensive hybrid power plant modeling with small-signal stability augmentation through flexible operation mode transition", IEEE Journal of Emerging and Selected Topics in Power Electronics, doi: 10.1109/JESTPE.2024.3432850.

[4] W. Zhang, W. Sheng, Q. Duan, H. Huang and X. Yan, "Automatic generation control with virtual synchronous renewables," in Journal of Modern Power Systems and Clean Energy, vol. 11, no. 1, pp. 267-279, January 2023, doi: 10.35833/MPCE.2020.000921.

[5] M. Taghavi and C.J. Lee, “Development of a novel hydrogen liquefaction structure based on liquefied natural gas regasification operations and solid oxide fuel cell: Exergy and economic analyses”, Fuel, vol. 384, Art. no. 133826, 2025, doi: 10.1016/j.fuel.2024.133826.

[6] M. Taghavi, H.J. Yoon, J.-U. Choi, and C.J. Lee, “Innovative structure of a liquefied natural gas (LNG) process by mixed fluid cascade using solar renewable energy, photovoltaic panels, and absorption refrigeration system”, Computer Aided Chemical Engineering, vol. 53, F. Manenti and G. V. Reklaitis, Eds. Elsevier, 2024, pp. 2071–2076, doi: 10.1016/B978-0-443-28824-1.50346-X.

[7] M. Taghavi and C.J. Lee, “Development of novel hydrogen liquefaction structures based on waste heat recovery in diffusion–absorption refrigeration and power generation units”, Energy Conversion and Management, vol. 302, Art. no. 118056, 2024, doi: 10.1016/j.enconman.2023.118056.

[8] H. Cheng, W. Huang, C. Shen, Y. Peng, Z. Shuai and Z. J. Shen, "Transient voltage stability of paralleled synchronous and virtual synchronous generators with ınduction motor loads", IEEE Transactions on Smart

Grid, vol. 12, no. 6, pp. 4983-4999, Nov. 2021, doi: 10.1109/TSG.2021.3104655.

[9] A. Suvorov, A. Askarov, A. Kievets, and V. Rudnik, "A comprehensive assessment of the state-of-the-art virtual synchronous generator models," Electric Power Systems Research, vol. 209, pp. 108054, 2022, https://doi.org/10.1016/j.epsr.2022.108054.

[10] O.A. Qudsi, A.Soeprijanto, A. Priyadi, "Virtual inertia calculation and virtual power system stabiliser design for stability enhancement of virtual synchronous generator system under transient condition", IET Energy Syst. Integr. 6(S1), 903–917 (2024).https://doi.org/10.1049/esi2.12177.

[11] M. Taghavi, H. Salarian, and B. Ghorbani, "Thermodynamic and exergy evaluation of a novel integrated hydrogen liquefaction structure using liquid air cold energy recovery, solid oxide fuel cell and photovoltaic panels", Journal of Cleaner Production, vol. 320, Art. no. 128821, 2021, doi: 10.1016/j.jclepro.2021.128821.

[12] M. Taghavi, H. Salarian, and B. Ghorbani, "Economic evaluation of a hybrid hydrogen liquefaction system utilizing liquid air cold recovery and renewable energies", Renewable Energy Research and Applications, vol. 4, no. 1, pp. 125-143, 2023, doi: 10.22044/rera.2022.11899.1122.

[13] S. Ho and M. Taghavi, "Solar energy development: Study cases in Iran and Malaysia", International Journal of Engineering Trends and Technology, vol. 70, no. 8, pp. 408–422, 2022, doi: 10.14445/22315381/IJETT-V70I8P242.

[14] D. Li, Q. Zhu, S. Lin and X. Y. Bian, "A self-adaptive ınertia and damping combination control of vsg to support frequency stability", IEEE Transactions on Energy Conversion, vol. 32, no. 1, pp. 397-398, March 2017, doi: 10.1109/TEC.2016.2623982.

[15] H. Wang, Y. Hao, H. He, H. Dong, S. Lu, G. Zhang, J. Yang, and Z. Chen., "Influence mechanism and virtual power system stabiliser method of virtual synchronous generator for low−frequency oscillation of power system", IET Energy Syst. Integr. 6(2), 104–116 (2024). https://doi.org/10.1049/esi2.12119.

[16] L. Chen, J. Tang, X. Qiao, H. Chen, J. Zhu, Y. Jiang, Z. Zhao, R. Hu, and X. Deng, "Investigation on transient stability enhancement of multi-VSG system incorporating resistive SFCLs based on deep reinforcement learning", IEEE Transactions on Industry Applications, vol. 60, no. 1, pp. 1780-1793, Jan.-Feb. 2024, doi: 10.1109/TIA.2023.3321264.

[17] M. Taghavi, H. Salarian, and B. Ghorbani, "Thermodynamic and exergy evaluation of a novel integrated hydrogen liquefaction structure using liquid air cold energy recovery, solid oxide fuel cell and photovoltaic panels", Journal of Cleaner Production, vol. 320, Art. no. 128821, 2021, doi: 10.1016/j.jclepro.2021.128821.

[18] M. Taghavi, H. Salarian, and B. Ghorbani, "Economic evaluation of a hybrid hydrogen liquefaction system utilizing liquid air cold recovery and renewable energies", Renewable Energy Research and Applications, vol. 4, no. 1, pp. 125–143, 2023, doi: 10.22044/rera.2022.11899.1122.

[19] C. Shen, Z. Shuai, Y. Shen, Y. Peng, X. Liu, Z. Li, and Z. J. Shen, "Transient stability and current injection design of paralleled current-controlled VSCs and virtual synchronous generators", IEEE Transactions on Smart Grid, vol. 12, no. 2, pp. 1118-1134, March 2021, doi: 10.1109/TSG.2020.3032610.

[20] P. Ge, C. Tu, F. Xiao, Q. Guo and J. Gao, "Design-oriented analysis and transient stability enhancement control for a virtual synchronous generator", IEEE Transactions on Industrial Electronics, vol. 70, no. 3, pp. 2675-2684, March 2023, doi: 10.1109/TIE.2022.3172761.

[21] T. Qoria, F. Gruson, F. Colas, G. Denis, T. Prevost and X. Guillaud, "Critical clearing time determination and enhancement of grid-forming converters embedding virtual ımpedance as current limitation algorithm", IEEE Journal of Emerging and Selected Topics in Power Electronics, vol. 8, no. 2, pp. 1050-1061, June 2020, doi: 10.1109/JESTPE.2019.2959085.

[22] A. N. Sheta, B. E. Sedhom, A. Pal, M. S. E. Moursi and A. A. Eladl, "Stability-constrained settings of directional overcurrent relays with shifted user-defined characteristics for distribution networks with DERs", IEEE Transactions on Power Delivery, vol. 39, no. 4, pp. 2401-2413, Aug. 2024, doi: 10.1109/TPWRD.2024.3403921.

[23] M. N. Acosta, E. Gómez, F. Gonzalez-Longatt, M. A. Andrade, E. Vázquez and E. Barocio, "Single value decomposition to estimate critical clearing time of a power system using measurements", IEEE Access, vol. 9, pp. 125999-126010, 2021, doi: 10.1109/ACCESS.2021.3111006.

[24] T. L. Vu, S. M. Al Araifi, M. S. El Moursi and K. Turitsyn, "Toward simulation-free estimation of critical clearing time", IEEE Transactions on Power Systems, vol. 31, no. 6, pp. 4722-4731, Nov. 2016, doi: 10.1109/TPWRS.2016.2523265.

[25] Y. Liu, Z. Chen, H. Yao, L. Yi and Q. H. Wu, "Estimating critical clearing time of grid faults using DA of state-reduction model of power systems", CSEE Journal of Power and Energy Systems, vol. 10, no. 2, pp. 807-820, March 2024, doi: 10.17775/CSEEJPES.2022.07170.

[26] C. Mishra, "Critical clearing time sensitivity for differential-algebraic power system model," IEEE Transactions on Power Systems, vol. 36, no. 4, pp. 3153-3162, July 2021, doi: 10.1109/TPWRS.2020.3040625.

[27] S. Jiriwibhakorn, "Critical clearing time prediction for power transmission using an adaptive neuro-fuzzy ınference system", IEEE Access, vol. 11, pp. 142100-142110, 2023, doi: 10.1109/ACCESS.2023.3341968.

[28] S. Sharma, S. Pushpak, V. Chinde and I. Dobson, "Sensitivity of transient stability critical clearing time", IEEE Transactions on Power Systems, vol. 33, no. 6, pp. 6476-6486, Nov. 2018, doi: 10.1109/TPWRS.2018.2854650.

[29] N. Yorino, A. Priyadi, H. Kakui and M. Takeshita, "A new method for obtaining critical clearing time for transient stability", IEEE Transactions on Power Systems, vol. 25, no. 3, pp. 1620-1626, Aug. 2010, doi: 10.1109/TPWRS.2009.2040003.

[30] I. B. Sulistiawati, A. Priyadi, O. A. Qudsi, A. Soeprijanto and N. Yorino, “Critical clearing time prediction within various loads for transient stability assessment by means of the extreme learning machine method”, International Journal of Electrical Power & Energy Systems, Vol. 77, 2016, Pages 345-352, ISSN0142-0615, doi: 10.1016/j.ijepes.2015.11.034.

[31] P. Alaee and T. Amraee, "Optimal coordination of directional overcurrent relays in meshed active distribution network using ımperialistic competition algorithm", Journal of Modern Power Systems and Clean Energy, vol. 9, no. 2, pp. 416-422, March 2021, doi: 10.35833/MPCE.2019.000184.

[32] B. Tan, J. Zhao, M. Netto, V. Krishnan, V. Terzija, and Y. Zhang, “Power system inertia estimation: Review of methods and the impacts of converter-interfaced generations”, International Journal of Electrical Power & Energy Systems, vol. 134, Art. no. 107362, Jan. 2022, doi: 10.1016/j.ijepes.2021.107362.

[33] "IEEE guide for protective relay applications to power system buses", IEEE Std C37.234-2009 , vol., no., pp.1 125, 6 Nov. 2009, doi:10.1109/IEEESTD.2009.5325912.

[34] M. Shahidehpour and Y. Wang, "Appendix C: IEEE30 Bus System Data", Communication and control in electric power systems: applications of parallel and distributed processing, IEEE, 2003, pp.493-495, doi: 10.1002/0471462926.app3.